Characterization of Al(Ga,In)N Nanowire Heterostructures and Applications in Light Emitting Diodes

Ashfiqua Tahseen Connie

Department of Electrical and Computer Engineering
Faculty of Engineering
McGill University
Montreal

April 2015

A thesis submitted to McGill University in partial fulfillment of the requirements of the degree of Doctor of Philosophy

To my family

Table of Contents

Table of Contents ..... **i**
List of Figures ..... **iii**
List of Tables ..... **vii**
List of Acronyms ..... **viii**
Abstract ..... **xi**
Abrégé ..... **xiii**
Contribution of Authors ..... **xvii**
Chapter 1. Introduction **1**
1.1 Nanowire LEDs 3
1.1.1 Strain Relaxation 3
1.1.2 Enhanced Light Extraction Efficiency 5
1.1.3 Surface States of Nanowires 6
1.2 III-Nitride Nanowire White LEDs 9
1.3 Ultraviolet LEDs 14
1.3.1 Ultraviolet LEDs: The Challenges 14
1.3.2 Optical Properties of Ultraviolet LEDs 18
1.4 Organization of the Thesis 23
Chapter 2. Epitaxial Growth, Fabrication, and Characterization Methods for Nanowire LEDs **25**
2.1 Plasma Assisted Molecular Beam Epitaxial Growth of Nanowire LEDs 25
2.2 Fabrication Procedure 27
2.2.1 Nanowire White LED Fabrication 27
2.2.2 Nanowire UV LED Fabrication 27
2.3 Luminescence Studies 29
2.3.1 Photoluminescence Studies 29
2.3.2 Electroluminescence Studies 32
2.3.3 Importance of PL and EL Spectroscopy 33
2.4 APSYS Simulation Tool 36
Chapter 3. High Performance Phosphor-Free Nanowire White LEDs **38**
3.1 Engineering the Functional Properties of Phosphor-Free Nanowire White LEDs 39
3.1.1 Growth of Nanowire White LEDs 40
3.1.2 Results and Discussions 41
3.2 Improving the Carrier Injection Efficiency of Phosphor-Free Nanowire White LEDs 45
3.2.1 Simulation Model 46
3.2.2 Effects of Surface States on Carrier Injection Efficiency of Nanowire LEDs 47
Chapter 4. Characterization of AlN Nanowires **52**
4.1 Optical Properties of Strain-Free Non-doped AlN Nanowires 52

4.1.1 Growth and Structural Characterization 53
4.1.2 Optical Characteristics 53
4.2 On the Magnesium Doping into AlN Nanowires 56
4.2.1 Optical Characterization 57
4.2.2 Electrical Characterization 61
4.3 Conclusion 63
Chapter 5. $Al_xGa_{1-x}N$ Nanowire LEDs 64
5.1 Highly Efficient Spectrally Pure 340 nm Ultraviolet Emission from $Al_xGa_{1-x}N$ Nanowire Based LEDs 64
5.1.1 Growth and Structural Characterization 65
5.1.2 Optical Characteristics 67
5.1.3 Electrical Characteristics 69
5.2 Sub-300 nm Deep Ultraviolet Emission from $Al_xGa_{1-x}N$ Homojunction Nanowire LEDs 72
5.2.1 Growth and Structural Characterization 72
5.2.2 Optical Characterization 74
5.2.3 Electrical Characterization 75
5.3 Demonstration of Deep Ultraviolet Emission at 210 nm from AlN *p-i-n* LED 77
5.4 Conclusion 79
Chapter 6. Conclusions and Future Works 80
6.1 Conclusions 80
6.2 Future Works 82
6.2.1 High Efficiency Deep UV LED 82
6.2.2 Deep UV Nanowire Laser Diodes 83
6.2.3 Utilizing the Benefits of N-polar III-Nitride Materials 84
List of Publications 86
Bibliography 89

List of Figures

Figure 1.1 Schematic illustration of a GaN wurtzite structure [47]. The Ga and N-atoms are arranged in layers and N-layer is at the top (N-polar). 2

Figure 1.2 The epitaxial growth of (a) epilayer, and (b) nanowire structure. Due to the lattice mismatched substrate, the epilayer undergoes severe strain. However, due to the lateral stress relaxation, stress is effectively accommodated in nanowire structure. 5

Figure 1.3 Electronic band structure of *c*-plane GaN surface; (a) Ga-face, (b) N-face [77]. Grey lines indicate the bulk band structure and red lines indicate energy bands due to the presence of surface states. (c) DOS for the surface structures of *c*-plane Ga-face GaN [77]. The grey areas are DOS of the bulk region and the red spikes are due to the surface states. 7

Figure 1.4 (a) Electronic band structure of *m*-plane GaN surface [77]. Grey lines indicate the bulk band structure and red lines indicate energy bands due to the presence of surface states. (b) DOS for the surface structures of *m*-plane GaN [77]. The grey areas are DOS of the bulk region and the red spikes are due to the surface states. 8

Figure 1.5 Schematic illustration of the depletion region dependence on nanowire diameter. The nanowire is fully depleted if the diameter is less than the critical value [83]. 9

Figure 1.6 EQE versus wavelength plot for visible LEDs. The EQE is very low in the 500 - 600 nm wavelength range, which is known as the 'green-gap' [8]. 11

Figure 1.7 QCSE in a structure having (a) 10% polarization, and (b) 35% polarization. QCSE is more pronounced in the structure having higher polarization. 12

Figure 1.8 Band structure near Γ point: (a) wurtzite GaN, and (b) wurtzite AlN..... 17

Figure 1.9 State of the art EQE of UV LEDs [14]. The EQE is ~0.1% for UV emission at wavelengths smaller than 250 nm. 17

Figure 1.10 IQE versus threading dislocation density plot [14]. IQE is reduced significantly as the threading dislocation increases. 19

Figure 1.11 Room temperature PL spectra of intrinsic and *n*-doped $Al_{0.3}Ga_{0.7}N$ [144]. A strong defect emission is observed for *n*-doped $Al_{0.3}Ga_{0.7}N$ at 450 nm. 20

Figure 1.12 PL spectra of *p*-doped $Al_xGa_{1-x}N$ at 10 K having different alloy compositions [130]. 21

Figure 1.13 Energy band diagram of *p*-doped AlN, demonstrating the transition between nitrogen vacancies and Mg-acceptor energy level [147]. 21

Figure 1.14 Temperature dependent PL spectra of $Al_xGa_{1-x}N$ having Al compositions of (a) 30%, (b) 50%, and (c) 80% [149]..... 23

Figure 2.1 A Veeco Gen II MBE system equipped with a radio frequency plasma assisted nitrogen source (located at the department of Electrical and Computer Engineering, McGill University)..... 26

Figure 2.2 (a) Schematic diagram of the fabricated white LED. (b) Optical image of the fabricated white LED devices. The device sizes are: 1 × 1 mm^2, 0.5 × 0.5 mm^2, 0.3 × 0.3 mm^2, and 0.1 × 0.1 mm^2. 28

Figure 2.4 Radiative and non-radiative optical transitions; Radiative transitions: A: band to band ($h\upsilon = E_g$), B: free exciton ($h\upsilon = E_g - E_X$), C and D: bound exciton ($h\upsilon = E_g - E_X - E_b$), E: donor to valence band ($h\upsilon = E_g - E_D$), F: conduction band to acceptor band ($h\upsilon = E_g - E_A$), G: donor-acceptor pair ($h\upsilon = E_g - E_D + E_A + q^2/\boldsymbol{\varepsilon r}$); Non-radiative transitions: H: defect state related, and I: Auger recombination. 30
Figure 2.5 Energy band diagram of a *p*-*n* homojunction; (a) separated *p*- and *n*-semiconductor, (b) the *p*-*n* junction with zero applied bias (W_D is the depletion width and eV_D is the potential barrier), (c) the *p*-*n* junction with an applied forward bias voltage of V [164]. 33

Figure 2.6 The eight reference color samples used to calculate CRI of the light source [169]..... 36

Figure 2.7 Flow chart of APSYS device simulation..... 37

Figure 3.1 (a) Schematic structure of the InGaN/(Al)GaN nanowire LED; (b) SEM image of the nanowire LEDs grown on *n*-Si substrate; (c) Normalized PL spectra of LED1 and LED2..... 41

Figure 3.2 (a) Normalized EL spectra of LED1 and LED2 measured at room temperature; (b) The CIE coordinates of LED1 and LED2; (c) The optical images of the emitted light of LED1 and LED2..... 42

Figure 3.3 EL spectra under different injection currents for (a) LED1 and (b) LED2. The measurement was carried out under pulsed biasing condition with 5% duty cycle at room temperature. 43

Figure 3.4 Schematic diagrams of the structures used in the simulation; (a) planar, and (b) nanowire..... 47

Figure 3.5 Comparison of carrier concentration of a planar and a nanowire structure under identical carrier excitation conditions. The carrier generation rate in the active region is set to 2.5 × 10^{27} $cm^{-3}\cdot s^{-1}$..... 48

Figure 3.6 Variation of carrier injection efficiency as a function of surface recombination velocity and nanowire diameter [191]. The carrier generation rate in the active region is set to 2.5 × 10^{27} $cm^{-3}\cdot s^{-1}$..... 49

Figure 3.7 (a) HAADF image, and (b) EDX elemental mapping of the active region of InGaN/GaN nanowire heterostructure [191]. 50

Figure 3.8 Comparison of the PL intensity of core-shell and non-core-shell nanowire LEDs. 50

Figure 4.1 (a) Schematic diagram of the AlN nanowires grown on GaN template on Si substrate. (b) The SEM image of the AlN nanowires taken with a 45^0 angle. (c) TEM image of a single AlN nanowire (10 nm above the GaN template). The arrow indicates the growth direction. 54

Figure 4.2 The low temperature (10 K) PL spectrum of (a) AlN nanowires, and (b) AlN epilayer. 55

Figure 4.3 Room temperature PL spectra of (a) AlN nanowires, and (b) AlN epilayer. .. 56

Figure 4.4 (a) Normalized PL spectra of Mg-doped AlN nanowires with different Mg flux and different growth rate at 20 K. (b) Power dependent PL spectra of sample E at 20 K; inset: ratio of integrated PL intensity of Mg-acceptor peak to that of band-edge peak versus power plot at 20 K. 59

Figure 4.5 Room temperature PL spectrum of sample E. A 197 nm frequency-quadrupled Ti-sapphire laser was used as the excitation source. 60

Figure 4.6 (a) Peak energy variation with temperature for band-edge and Mg-acceptor peaks of sample E. The solid line is the calculation by the Varshni's equation. (b) Integrated PL intensity versus inverse temperature plot for the Mg-acceptor peak. The solid line is the least square fit of the experimental data with the equation, $I_{emi} = \mathrm{I}_0/(1 + aexp(-\mathrm{E}_0/KT))$ 61

Figure 4.7 (a) Schematic illustration of the structure to calculate the resistivity of AlN: Mg nanowires; (b) Resistivity versus inverse temperature plot for AlN:Mg segment of sample F. 62

Figure 5.1 (a) Schematic diagram of the $Al_xGa_{1-x}N$ double heterostructure UV LED. (b) SEM image of the $Al_xGa_{1-x}N$ nanowires on Si substrate. 66

Figure 5.3 (a) Power dependent PL spectra measured at room temperature. (b) Temperature dependent PL spectra measured at 7 mW excitation power. 68

Figure 5.4 Integrated PL intensity versus inverse temperature plot for $Al_xGa_{1-x}N$ double heterojunction nanowire LED. 69

Figure 5.5 (a) The room temperature I-V curve of the $Al_xGa_{1-x}N$ nanowire LED for device size of 0.3×0.3 mm^2. Inset: I-V characteristics of the device under forward and reverse bias conditions in semi-log scale. (b) Typical EL spectra measured at room-temperature with continuous wave biasing condition of a 0.3×0.3 mm^2 device. 71

Figure 5.6 Relative EQEs of the $Al_xGa_{1-x}N$ nanowire LEDs measured at room-temperature by using CW and pulsed injection current with 1% duty cycle. The self heating effect is observed under CW biasing condition. 71

Figure 5.7 (a) The schematic diagram showing the $Al_xGa_{1-x}N$ homojunction nanowire based LED structure. (b) SEM image of nanowires grown on *n*-Si (111). (c) TEM image of a single nanowire. (d) HR-TEM image taken at the edge of nanowire revealing the formation of a shell around the sidewall of the nanowire. (e) Lateral elemental profile measured along a-b line in Fig.5.7(c) showing the core-shell structure. 73

Figure 5.8 (a) Room temperature PL spectra of nanowire LEDs at different power from 0.1 mW to 8 mW. (b) Integrated PL intensities versus inverse temperature plot of the DUV peak at 290 nm. The room-temperature IQE is estimated to be 41%. 74

Figure 5.9 (a) Typical I-V curve of the $Al_xGa_{1-x}N$ homojunction nanowire LED with device size of 0.3×0.3 mm^2. Inset: I-V characteristic of the device under forward and reverse bias in semi-log scale. (b) Room temperature EL spectra of the $Al_xGa_{1-x}N$ homojunction nanowire LEDs under different injection current from 1 mA to 40 mA. .. 76

Figure 5.10 Integrated EL intensity versus temperature plot for the UV homojunction LED at 10 mA injection current. The plot shows maximum peak intensity at a temperature of 150 K. 76

Figure 5.11 (a) Schematic diagram of the AlN *p-i-n* LED on GaN template on Si substrate. The room temperature PL spectra of AlN nanowires: (b) Si-doped, and (c) Mg-doped. 78

Figure 5.12 (a) The I-V characteristics of the AlN *p-i-n* LED. (b) The current dependent EL spectra of the AlN *p-i-n* LED. 78

Figure 6.1 Schematic illustration of $Al_xGa_{1-x}N$ based deep UV laser on Si substrate. 84

Figure 6.2. Simulated energy band diagram of a single QW InGaN/GaN LED device, (a) Ga-polar, and (b) N-polar [276]. 85

List of Tables

Table 1.1 Lattice parameters and thermal expansion coefficients for binary III-nitride semiconductors (GaN, AlN, InN) and the commonly used substrates (Sapphire, SiC, and Si) [55-57]. 4

Table 3.1 The CRI, CCT, and CIE coordinate values at different injection currents under pulsed biasing condition (5% duty cycle) for 0.3 × 0.3 mm^2 devices of LED1 and LED2. 44

Table 4.1: Growth parameters for Mg-doped AlN samples having different growth rates and different doping levels..... 58

List of Acronyms

APSYS	Advanced Physical Models of Semiconductor Devices
CBM	Conduction Band Minima
CCT	Correlated Color Temperature
CIE	The 1931 Commission International De L'eclairage Chromaticity Diagrams
CL	Cathodoluminescence
CRI	Color Rendering Index
DAP	Donor-Acceptor Pair
DFT	Density Functional Theory
DOS	Density of States
DPSS	Diode Pumped Solid State
DUV	Deep Ultraviolet
EBL	Electron Blocking Layer
EDX	Energy Dispersive X-ray
EHP	Electron Hole Pair
EL	Electroluminescence
ELO	Epitaxial Lateral Overgrowth
EQE	External Quantum Efficiency
FEA	Finite Element Analysis
FWHM	Full-Width-at-Half-Maxima

FX	Free Exciton
HAADF	High Angle Annular Dark Field
HCP	Hexagonal Closed Pack
HEMT	High Electron Mobility Transistor
HF	Hydro-Fluoric
IQE	Internal Quantum Efficiency
ITO	Indium Tin Oxide
LD	Laser Diode
LED	Light Emitting Diode
LO	Longitudinal Optical
MBE	Molecular Beam Epitaxy
MOVPE	Metal-Organic Vapor Phase Epitaxy
MQW	Multiple Quantum Well
NC	Nano Crystal
NADH	Nicotinamide Adenine Dinucleotide
PALE	Pulse Atomic Layer Deposition
PAMBE	Plasma Assisted Molecular Beam Epitaxy
PD	Photo Detector
PL	Photoluminescence
QCSE	Quantum Confined Stark Effect
QW	Quantum Well

RF	Radio Frequency
SAG	Selective Area Growth
SCCM	Standard Cubic Centimeter per Minute
SO	Surface Optical
SPD	Spectral Power Distribution
SRH	Shockley-Read-Hall
TD	Threading Dislocation
TE	Transverse Electric
TM	Transverse Magnetic
UV	Ultraviolet
VBM	Valence Band Maxima
VLS	Vapor-Liquid-Solid

Abstract

One of the main advantages of nanowire structures is its ability to grow dislocation-free crystal on a foreign substrate, which has been the major bottleneck for III-nitride planar structures. This unique feature, along with nanowires' reduced polarization field and high light extraction efficiency enables us to realize high performance InGaN/GaN white light emitting diodes (LEDs), as well as supreme quality AlN nanowires and AlGaN based deep ultraviolet (UV) LEDs. This dissertation reports on the achievement of high efficiency InGaN/GaN white LEDs with high color rendering index (CRI) and tunable correlated color temperature (CCT) values. Furthermore, we present the realization of dislocation-free AlN nanowires with controllable *p*-type conduction and the achievement, for the first time, of AlN nanowire UV LEDs emitting at 210 nm.

We have achieved a very high CRI value (>90) for InGaN/GaN white LEDs in both warm and cool white regions. The novelty of the approach is the easy tunability of the spectrum by changing the growth conditions at the wafer-level. Furthermore, by designing the core-shell structure, we have achieved a relatively high output power of 1.5 mW for a current density of 70 $A \cdot cm^{-2}$ for unpackaged devices, which is two orders of magnitude higher than the nanowire LED structures without shell coverage.

The achievement of dislocation-free AlN nanowires opens up the possibility to develop deep UV LEDs. We have presented strong band-edge emission, both at low temperature and room temperature, from non-doped AlN nanowires. We have grown AlN:Mg nanowires with different Mg-doping levels. Through detailed electrical measurements, we have identified hopping conduction as the major carrier transport mechanism at room temperature and the room temperature free hole concentration is estimated to be $\sim 10^{16}$ cm^{-3}, which is orders of magnitude higher than previously reported values in AlN.

We have presented the enhanced optical and electrical performances of UV LEDs in the UV-A (340 nm) and UV-B (290 nm) range. The LEDs show strong and stable emissions with high internal quantum efficiencies (IQE); the IQE of UV-A LED is 59% and UV-B LED is 41%. These values are comparable with the planar LEDs in the same wavelength range. Most importantly, we have demonstrated the realization of AlN *p-i-n* LEDs

emitting at 210 nm. This is the first demonstration of deep UV LED emission in such a short wavelength range using nanowire structures. The AlN *p-i-n* LED presents a turn-on voltage of 6 V and a low operating voltage (8 V at 20 mA). Strong electroluminescence is also observed at different injection currents. The realization of dislocation-free AlN nanowires with controllable doping and the demonstration of AlN *p-i-n* LEDs open up the possibility to achieve high performance tunable deep UV LEDs.

Abrégé

L'un des principaux avantages des structures de nanofils est leur capacité à croître libre de dislocations sur un substrat étranger, qui a toujours été un facteur limitant important pour les structures planaires à base de III-nitrure. Cette caractéristique unique, avec le champ de polarisation réduit des nanofils et l'efficacité d'extraction de la lumière élevée, nous permet de réaliser des diodes électroluminescentes (DELs) à base d'InGaN/GaN de haute performance pour la production de lumière blanche, ainsi que des DELs à base de nanofils d'AlN et d'AlGaN de haute qualité émettant dans l'ultraviolet (UV) profond. Cette thèse rend compte de la réalisation de DELs blanches à base d'InGaN/GaN à efficacité élevée avec un haut indice de rendu de couleur (IRC) et une température de couleur proximale accordable. De plus, nous présentons la réalisation de nanofils d'AlN libres de dislocations avec une conduction de type p contrôlable, et la réalisation, pour la première fois, de diodes électroluminescentes UV en nanofils d'AlN émettant à 210 nm.

Nous avons réalisé un IRC très élevé (>90) avec les DELs blanches à base d'InGaN/GaN dans les régions blanches chaudes et froides. La nouveauté de cette approche est l'accordabilité facile du spectre en modifiant les conditions de croissance au niveau de la tranche. En outre, par la conception de la structure noyau-enveloppe, nous avons atteint une puissance de sortie relativement élevée de 1,5 mW pour les dispositifs non encapsulés, ce qui représente deux ordres de grandeur de plus que les structures sans noyau-enveloppe.

La réalisation de nanofils d'AIN libres de dislocations permet de développer des DELs émettant dans l'UV profond. Nous avons présenté une forte émission à l'extrémité de la bande, à la fois à basse température et à température ambiante, à partir de nanofils d'AlN non dopés. Nous avons fait croitre des nanofils d'AIN:Mg avec différents niveaux de dopage de Mg. Grâce à des mesures électriques détaillées, nous avons identifié que la conduction par saut à distances est le mécanisme principal de transport des porteurs de charges à la température ambiante, et que la concentration de trous libres à la température

ambiante est estimée à ~10^{16} cm^{-3}, qui est plus élevée de plusieurs ordres de grandeur que les valeurs précédemment rapportées pour l'AIN.

Nous avons présenté des performances optiques et électriques améliorées des DELs UV dans l'UV-A (340 nm) et UV-B (290 nm). Ces DELs montrent une émission forte et stable avec une grande efficacité quantique interne (IQE); l'IQE des DELs UV-A est de 59% et celle des DELs UV-B est de 41%. Ces valeurs sont comparables avec les diodes planaires dans la même gamme. Plus important encore, nous avons démontré la réalisation de DELs PIN à base d'AIN émettant à 210 nm. Il s'agit de la première démonstration de DELs émettant dans l'UV profond dans une telle courte portée en utilisant des structures de nanofils. La DEL PIN à base d'AIN présente une tension d'allumage de 6 V et une tension d'alimentation basse (8 V à 20 mA). Une forte électroluminescence est également observée à différents courants d'injection. La réalisation nanofils d'AlN libres de dislocations avec un dopage contrôlable et la démonstration de DELs PIN à base d'AIN ouvre la possibilité d'atteindre des DELs UV accordables de haute performance.

Acknowledgement

At first I would like to thank the Almighty Allah for giving me the opportunity to pursue my doctoral study.

I wish to express my sincere gratitude to the persons without whom it would not be possible to complete this work. First of all, I want to express my heartfelt gratitude to my supervisors, Dr. Zetian Mi and Dr. Ishiang Shih for their tremendous support. This dissertation work would not be possible without their guidance, advice, and encouragement. They helped me with their valuable suggestions whenever I needed. I would also like to thank Dr. Vamsy Chodavarapu and Dr. Mourad N. El-Gamal for their valuable questions and comments during the examinations, suggestions and evaluation of the work.

I am greatly indebted to my lab mates for their help, encouragements, and discussions. My special thanks are to Dr. Hieu Pham Trung Nguyen, Dr. Songrui Zhao, and Dr. Qi Wang. Dr. Nguyen was always available for discussions whenever I needed and kindly had grown many samples for me. Dr. Wang introduced me to the measurement techniques and helped me with the set-ups a lot. Dr. Zhao helped me a lot with his valuable suggestions on theoretical analysis and on measurement techniques. He had also grown many samples for my measurements. I also wish to thank Dr. Shaofei Zhang for his help with simulation.

Here I list the name of my colleagues who helped me a lot during my stay at McGill: Sharif M. Sadaf, Junjie Kang, Xianhe Liu, M. Hadi Tavakoli Dastjerdi, Mehrdad Djavid, Dr. Shamsul Arafin, Dr. Hadley Myers, Sunyoung Perk, Renjie Wang, Binh Le Huy, Nhung Hong Tran, Dr. Yong-Ho Ra, Md. Golam Kibria, Md. Faqrul Alam Chowdhury, Bander AlOtaibi, and Shizhao Fan. A very special thanks to David Laleyan for translating the abstract to French. I also want to express my gratitude to Donald Pavlasek, shop supervisor at the ECE Design and Machining facility, who always come up with novel ideas for the tools needed to prepare for the measurements.

Finally, I would like to thank my family for their support and encouragement. I wish to express my earnest gratitude to my husband and my son, who were always with me and always encouraged me throughout this whole journey.

Last but not the least, I thank Natural Sciences and Engineering Research Council of Canada and the Fonds de recherché sur la nature et les technologies for their financial support on this research.

Contribution of Authors

This dissertation work is enriched with the contribution of the candidate and many other individuals. The candidate and her supervisors, Dr. Zetian Mi and Dr. Ishiang Shih defined the projects and worked closely on discussions regarding the methodology and progress of the projects. The design, optimization, and characterization were done by the candidate with the help of Dr. Songrui Zhao, Dr. Hieu Pham Trung Nguyen, and Dr. Qi Wang. The molecular beam epitaxial growth of the white and UV nanowire LEDs were performed by Dr. Hieu Pham Trung Nguyen and Dr. Songrui Zhao, respectively. The device modeling was done by the candidate with assistance from Dr. Shaofei Zhang. The TEM and SEM imaging was done by Dr. Songrui Zhao and Dr. Hieu Pham Trung Nguyen. Sharif Md. Sadaf and M. Hadi Tavakoli Dastjerdi helped with device fabrication. The optical and electrical characterizations of the nanowire white LEDs were performed by the candidate. The characterization of UV LEDs was performed primarily by the candidate with some assistance from Dr. Songrui Zhao and Dr. Qi Wang. Dr. Hongxing Jiang and his group in Texas Tech University contributed to the measurement and discussions on the AlN nanowires.

Chapter 1. Introduction

III-nitride semiconductor materials (InN, GaN, AlN, and their related alloys) are emerging as prospective candidates for today's optoelectronic devices. They are blessed with unique properties, such as high electron mobility, large absorption coefficient, high saturated electron drift velocity, and high chemical stability [1-6]. Most importantly, III-nitride materials exhibit direct band gap, from 0.65 eV (InN) to 6.1 eV (AlN), i.e., from ultraviolet (UV) to infrared (IR), covering the whole solar spectrum. The use of III-nitride materials in the applications of light emitting diodes (LEDs) [7-14], photodetectors (PDs) [15-20], solar cells [21-26], laser diodes (LDs) [27-30], high electron mobility transistors (HEMTs) [31-35], and sensors [36, 37] is a continuously advancing research area with a view of achieving efficient device performance by utilizing the unique properties of this material family.

The III-nitride materials can be crystallized in wurtzite, zinc-blende or rocksalt structure. The wurtzite structure is the thermodynamically stable structure. There are few reports on zinc-blende structure [38-42]. The formation of rocksalt structure is possible only under high pressure [43, 44]. The wurtzite structure is a hexagonally closed pack (hcp) lattice. Since the unit cell is hexagonal, it has two lattice parameters, namely, c and a. c defines the distance of two atoms in different atomic planes, and a defines the distance of atoms in the same lattice plane. The different c/a ratio of InN, GaN, and AlN is a signature of their deviation from the ideal wurtzite structure which affects their properties. Another important feature is the polarity of the material. The schematic diagram illustrating the GaN wurtzite structure is presented in Fig. 1.1. As apparent in Fig. 1.1, the Ga and N atoms are arranged in bilayer and the polarity of the material is defined by the top layer. If the top layer is metal (Ga in this case), it is metal/Ga polar and otherwise, N-polar. This polarity is determined by the growth conditions; e.g., III-nitride materials grown by metal-organic vapor phase epitaxy (MOVPE) is usually Ga-polar but the same material grown by molecular beam epitaxy (MBE) is N-polar [45, 46]. Both bulk (e.g., the polarization field) and surface properties (e.g., the band bending at the surface) depend on

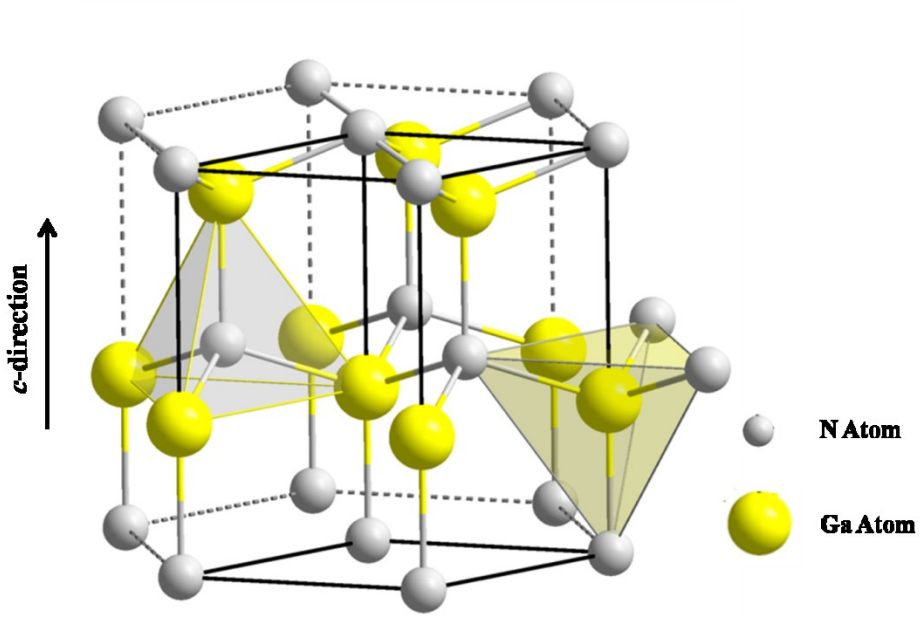

Figure 1.1 Schematic illustration of a GaN wurtzite structure [47]. The Ga and N-atoms are arranged in layers and N-layer is at the top (N-polar).

the polarity of the material and hence, is critical for the design of the devices employing the polarization and/or the surface charge feature.

Another important feature of III-nitride material is the presence of intrinsic spontaneous and strain-induced piezoelectric polarization. The built-in asymmetry of the wurtzite crystal structure is the cause of the spontaneous polarization. Due to the lack of lattice matched substrate, the III-nitride materials are grown by heteroepitaxy and as a result, experience tensile or compressive strain which leads to piezoelectric polarization. This is also present in heterostructures and can play a significant role in device performance. Quantum-confined Stark effect (QCSE), efficiency droop, non-uniform carrier distribution can be directly related to polarization effect. This effect is more prominent in planar structures than nanowires and will be described in detail in the following sections.

The characteristics of III-nitride white and UV nanowire LEDs have been studied in this thesis. In this chapter, a brief introduction of nanowire LEDs, including the challenges and advantages will be discussed. The current status of white nanowire LEDs and the need, challenges, and current status of UV LEDs will be described subsequently.

1.1 Nanowire LEDs

Nanowires are very thin structures having diameters in nanometer (nm) range. This low dimensional structure may offer quantum confinement in two directions leaving one dimension for carrier conduction. The high surface-to-volume ratio, strain relaxation through lateral surface, the size dependent band gap tunability, enhanced exciton binding energy, enhanced surface scattering are some of the unique properties of nanowires [48]. Another important advantage of nanowire is its small size. To keep up with Moore's law, circuits are getting miniaturized day by day. Having small structure widens the scope of integrating with today's miniaturized electronic devices.

In the following paragraphs, the three critical properties of nanowires related to our research on III-nitride devices, namely, strain relaxation, enhanced light extraction efficiency and the high aspect ratio will be described in detail.

1.1.1 Strain Relaxation

As mentioned previously, there is no lattice matched substrate for III-nitride materials. The most commonly used substrates are sapphire, SiC, and Si [49]. The lattice parameters of the substrates and the III-nitride binary materials are presented in Table 1.1. It is apparent from Table 1.1 that all of the substrates have large lattice mismatches and differences in thermal conductivities. This is very crucial from the growth point of view. Since the layers are grown epitaxially on the substrate, they undergo tensile or compressive strain. As the layers are above a critical thickness (typically ~ 53 (Å) for GaN for a lattice mismatch of 3% and much smaller for increased lattice mismatch), dislocations are generated in the structure. The dislocation density of GaN grown on these substrates is typically in the range of $10^8 \sim 10^{10}$ cm^{-2} [50-52]. These dislocations cause electronic states in the bandgap and potential variation throughout the structure and serve as non-radiative recombination centers, resulting in severe degradation in the optical and electrical performance of the device. Another direct consequence of the strain is the piezoelectric polarization. The performance of LEDs can be severely affected by the presence of polarization. In this respect, the nanowire structure offers a significant advantage over the planar structure. As the nanowires are grown vertically and have

small diameters, they offer lateral stress relaxation [53]. Because of this, the critical thickness to form dislocations is larger in the case of nanowires [54] and the crystal quality is superior to its planar counterpart. The process of stress relaxation in thin film and nanowire structure is schematically presented in Fig. 1.2.

Table 1.1 Lattice parameters and thermal expansion coefficients for binary III-nitride semiconductors (GaN, AlN, InN) and the commonly used substrates (Sapphire, SiC, and Si) [55-57].

Material	**Lattice Constant (Å)**	**Thermal Expansion Coefficient ($\times 10^{-6}$/K)**
GaN	$a = 3.189$	5.59
	$c = 5.185$	3.17
AlN	$a = 3.112$	4.2
	$c = 4.982$	5.3
InN	$a = 3.537$	5.3
	$c = 5.704$	4.2
Sapphire	$a = 4.765$	5.9
	$c = 13.001$	6.3
6H-SiC	$a = 3.081$	4.2
	$c = 15.117$	4.68
Si	$a = 3.840$	3.59

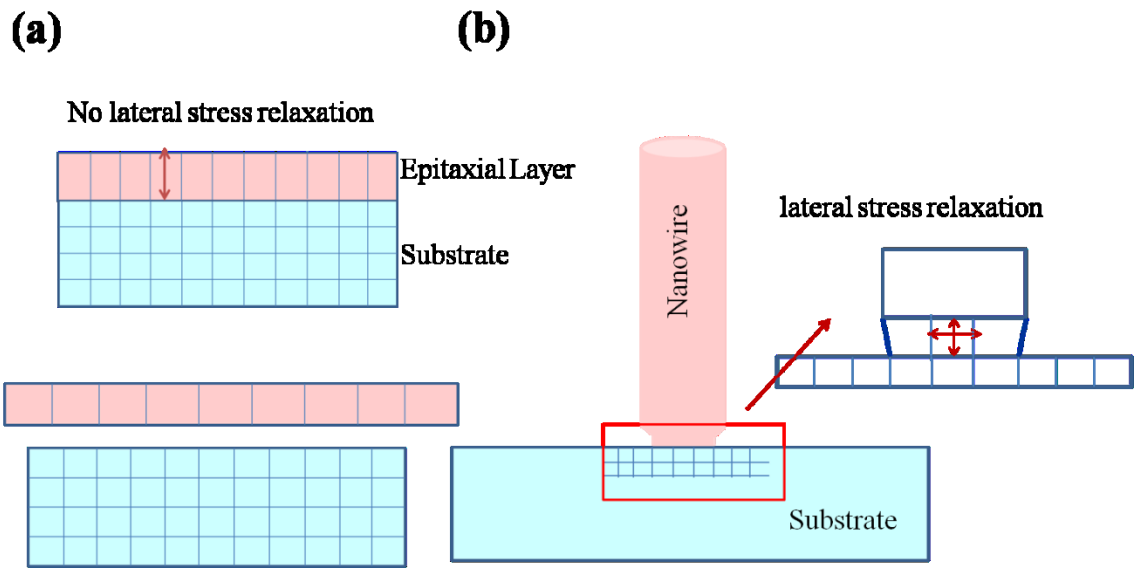

Figure 1.2 The epitaxial growth of (a) epilayer, and (b) nanowire structure. Due to the lattice mismatched substrate, the epilayer undergoes severe strain. However, due to the lateral stress relaxation, stress is effectively accommodated in nanowire structure.

1.1.2 Enhanced Light Extraction Efficiency

Light extraction efficiency is an important parameter of the LED, which, together with the internal quantum efficiency (IQE), largely determines the output power and external quantum efficiency (EQE) of the device. In the case of planar LEDs, due to the difference of the refractive index between the semiconductor material and air, light extraction is significantly limited by the total internal reflection. The theoretical light extraction efficiency achieved from a typical planar structure is about 4% [58]. Several approaches have been employed to improve the light extraction efficiency, such as shaping of LED dies, surface roughening, use of transparent substrates, and flip-chip packaging. The main principle of these approaches is to either increase the escape cone by means of a dome shaped surface, or by enabling multiple photon entry into the escape cone by surface roughening or photon recycling [59-61]. Transparent substrate is used to minimize the photon absorption by the substrate while flip-chip packaging prohibits the blocking of light by metal pads. Additionally, the use of patterned substrates, resonant cavity, and photonic crystal has been intensively studied to enhance the light extraction efficiency [58, 62-66]. The use of patterned substrate enables the scattering of photons and thus allows more photons to escape the LED surface. In resonant cavity LEDs, the active

region is embedded into a semiconductor slab sandwiched between two mirrors. The distance between the two mirrors is on the order of a wavelength and thus, they form the optical micro-cavity. In such a cavity, only optical waves with fundamental resonance mode can propagate. With a proper cavity design, it is possible to force the photons to propagate towards the escape cone and thus, to enhance the light extraction efficiency. Photonic crystals can also control the light propagation through the medium and hence, can significantly improve the light extraction efficiency [67-69]. However, such processes are complex, require careful design and increase the manufacturing cost.

Geometrically nanowire structure offers high surface-to-volume ratio, presenting more area for the photons to escape. Not only that, nanowire structure presents lower effective index [70], resulting in an increase in the escape cone and reduction in the total internal reflection. Light extraction efficiency can be enhanced by taking advantage of the guided mode by which the photons are guided towards the surface and hence, the other optical modes are eliminated. The scattering effect and improved light output coupling also help to enhance the light extraction efficiency [71-73]. It has been shown that by careful design of the nanowires, considering the diameter, fill factor, and the filler material as the design parameters, it is possible to achieve 72 ~ 79% enhancement in the light extraction efficiency [70, 74].

1.1.3 Surface States of Nanowires

Nanowires are characterized by large surface-to-volume ratio. Although this high aspect ratio is advantageous for many applications, they are also plagued with a high density of surface states. The periodicity of the crystal structure is terminated at the surface and electronic states are introduced in the forbidden band gap of the semiconductor. Several studies describe the presence of surface states and Fermi level pinning at the near surface region of GaN [75-77]. A detailed study illustrating the presence of surface states in both polar and non-polar surface of GaN employing density functional theory (DFT) is presented in [77].

The electronic band structure for *c*-plane and *m*-plane GaN surface along with the density of states (DOS) for the stable surface structure is presented in Figs. 1.3 and 1.4, respectively [77]. Two sets of surface states are identified for polar GaN surfaces. For

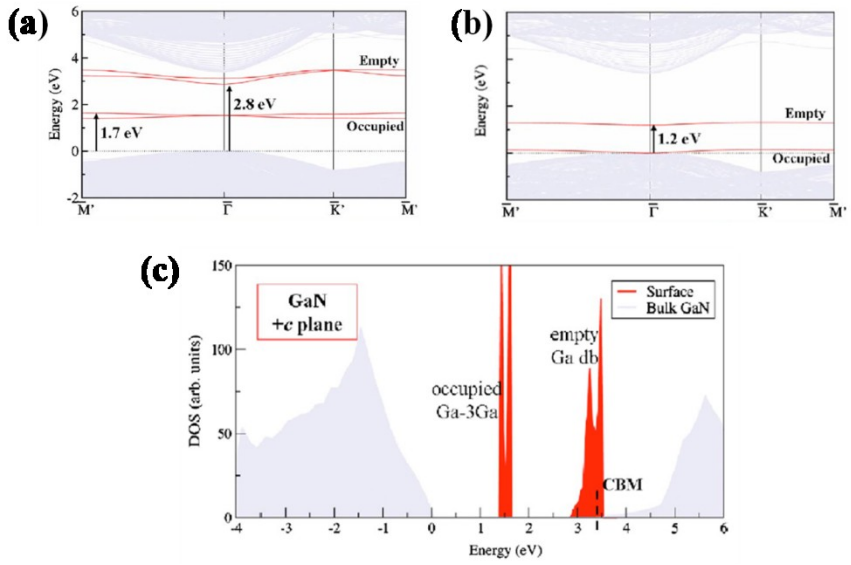

Figure 1.3 Electronic band structure of *c*-plane GaN surface; (a) Ga-face, (b) N-face [77]. Grey lines indicate the bulk band structure and red lines indicate energy bands due to the presence of surface states. (c) DOS for the surface structures of *c*-plane Ga-face GaN [77]. The grey areas are DOS of the bulk region and the red spikes are due to the surface states.

Ga-face, the upper state is situated at ~0.6 eV below the conduction band minima (CBM) whereas the lower state is situated at ~1.7 eV above the valence band maxima (VBM). The upper states are empty and are originated due to the dangling bonds of Ga-adatoms. The lower states are occupied and well localized on bonds between Ga-adatom and three Ga surface atoms. For N-face, the upper states are also originated from Ga-dangling bonds whereas nitrogen dangling bonds are responsible for the lower occupied state. The DOS plot in Fig. 1.3(c) presents the sharp peaks associated with the surface states. Due to the presence of the unoccupied surface states, the Fermi level is pinned in the forbidden band gap region. However, the energy at which the Fermi level is pinned depends on the doping of the nanowire.

For the *m*-plane surfaces, the upper state unoccupied Ga dangling bond is situated at ~0.7 eV below the CBM and its energy level is similar to the Ga-face polar surface, as presented in Fig. 1.4. However, nitrogen dangling bonds are responsible for the occupied surface states and they overlap with the valence band. This prohibits the formation of any levels within the band gap.

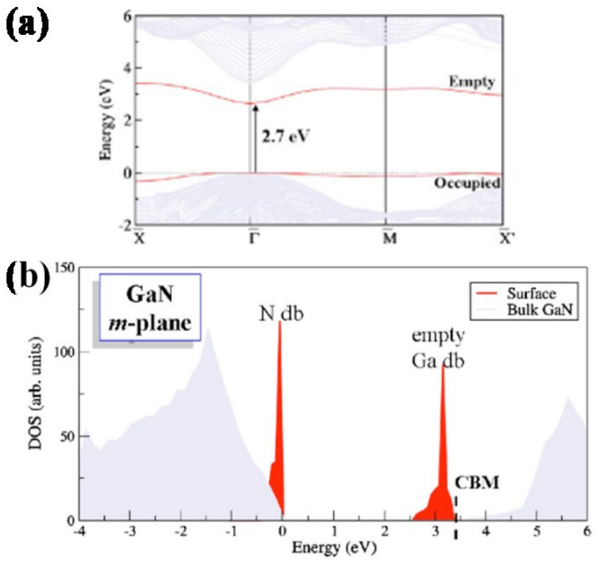

Figure 1.4 (a) Electronic band structure of *m*-plane GaN surface [77]. Grey lines indicate the bulk band structure and red lines indicate energy bands due to the presence of surface states. (b) DOS for the surface structures of *m*-plane GaN [77]. The grey areas are DOS of the bulk region and the red spikes are due to the surface states.

Surface states have many derogatory effects on the performance of nanowire devices. First and foremost, they introduce surface traps which can capture carriers from the active region, thus reducing the carrier injection efficiency. This results in the ultimate reduction of EQE of the device [78]. Furthermore, the Shockley-Read-Hall (SRH) non-radiative recombination is enhanced in the presence of surface states and results in the slow rising trend of EQE under electrical injection [79].

As mentioned previously, the Fermi level is pinned in mid-band gap region due to the presence of surface states. For *c*-plane *n*-doped GaN nanowire (lateral surface is the *m*-plane), the Fermi level is pinned at ~0.7 eV below the CBM [75, 77]. For the *c*-plane *p*-GaN nanowires, there is no occupied surface state in the band gap region of non-polar surface. However, impurity incorporation or the presence of defects causes downward surface band bending for *p*-type GaN nanowires [80, 81]. Such pinning and surface band bending result in the formation of surface depletion (accumulation) for GaN (InN) nanowires [82-85]. The effect of surface depletion is schematically presented in Fig. 1.5 [83]. The width of the depletion region depends on the doping concentration of the nanowire, the trap density at the surface, and also, on the nanowire diameter. The depletion width increases with decreasing doping concentration and increasing trap

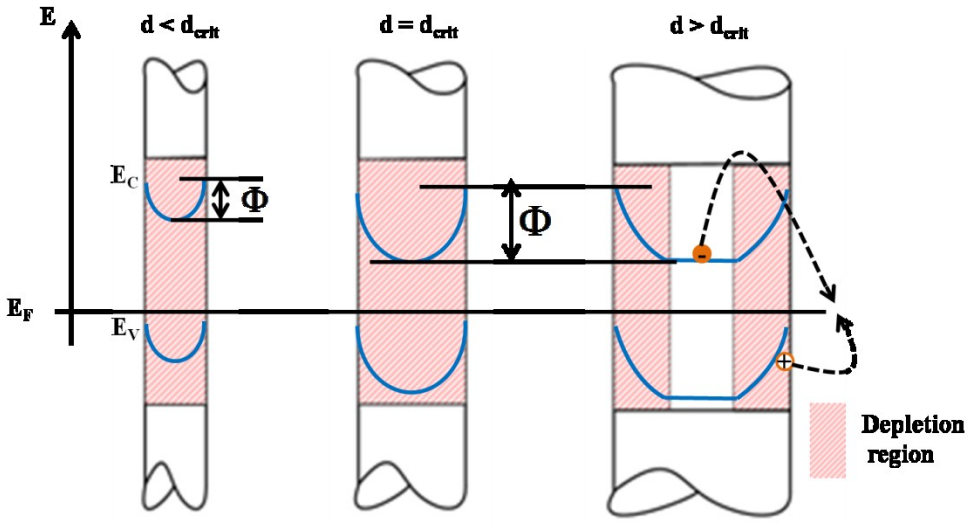

Figure 1.5 Schematic illustration of the depletion region dependence on nanowire diameter. The nanowire is fully depleted if the diameter is less than the critical value [83].

levels. Higher trap levels at the surface requires more charge to establish charge balance between surface charges and ionized impurities within the depletion region, resulting in wider depletion width. The depletion width and doping level always maintain an inverse relation, even in the case of a planar structure. Another important fact is that the depletion width decreases with increasing nanowire diameter, which is due to the relative scaling of the nanowire volume and surface area. This also implies that there must be a critical diameter below which the nanowires are fully depleted. The critical diameter is calculated to be 50 ~ 80 nm for *n*-doped (doping level is 10^{17} cm^{-3}) GaN nanowires and 100 nm for non-doped GaN nanowires [82, 83]. Due to the presence of depletion region, majority carriers are restricted only to the core region of the nanowire. This affects the device performance in terms of effective carrier concentration, carrier mobility, and conductivity of the nanowire.

1.2 III-Nitride Nanowire White LEDs

White light, which is a combination of all the basic colors including red, green, and blue, can be generated in several ways. The most common approach is to use phosphor for color conversion [86]. In this approach, phosphor is used to down-convert the emission of

a blue or UV LED into green/red light, which combines with part of the emission of the blue or UV LED and leads to the appearance of white light. However, the efficiency of this approach is generally low due to the energy loss related to the color conversion. Furthermore, tunability is very difficult in phosphor converted white LEDs. Due to the phosphor degradation, these devices are also prone to thermal and long term usage degradation. Another approach is to mix the color of different colored LEDs to generate white light directly. However, the post processing circuitry is complex and the efficiency is not great in this case. In this context, InGaN based LEDs present a welcoming alternative to generate white light. Multicolor emission, which apparently results in phosphor-free white light emission, can be achieved by varying the growth conditions, e.g., In/Ga flux ratio and substrate temperature. However, this approach is not free from shortcomings. The challenges and present status of InGaN based white LEDs are described in the following paragraphs.

The famous 'green-gap' is a well known problem in the research area of III-nitride white LEDs [7, 8]. The InGaN LEDs exhibit high EQE in the blue and violet region but a drop in EQE is observed in the green/ yellow region, as illustrated in Fig. 1.6 [8]. The increased In content in the longer wavelength region degrades the material quality and also, the polarization effects get more pronounced. On the other hand, AlInGaP LEDs depict high efficiency in longer wavelength region but performs poorly in short wavelength region due to having indirect bandgap in that region. Another vital problem of III-nitride LEDs is the presence of efficiency droop. InGaN based LEDs reach the maximum efficiency at a lower current density and then the efficiency decreases as the current increases. This makes the achievement of high power LEDs more difficult.

Several reasons are responsible for efficiency droop, namely the presence of defects, polarization field, poor hole transport, Auger recombination, and electron overflow. Considering all these effects, the IQE (η_i) can be typically described by the ABC model [87, 88],

$$\eta_i = \frac{Bn^2}{An+Bn^2+Cn^3+f(n)} \tag{1.1}$$

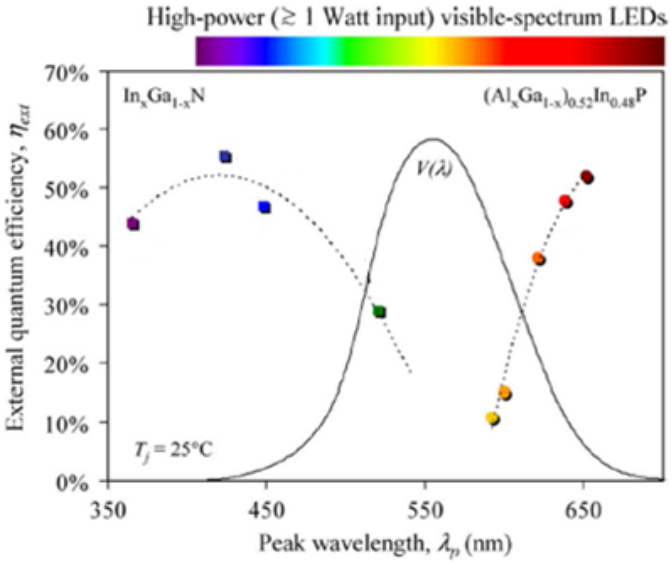

Figure 1.6 EQE versus wavelength plot for visible LEDs. The EQE is very low in the 500 - 600 nm wavelength range, which is known as the 'green-gap' [8].

where, A, B, and C are the SRH non-radiative coefficient, radiative coefficient, and Auger coefficient, respectively. The function $f(n)$ represents the carrier overflow outside the active region. The effects of these phenomena are described briefly in the following paragraphs.

Defects and Dislocations: As discussed in Section 1.1, due to the absence of lattice matched substrates, the defect density is higher in III-nitride materials. The defect density in planar GaN based heterostructures can be as high as $10^8 \sim 10^{10}$ cm^{-2} [50-52]. Generally, this high density of defects creates states in the forbidden energy gap and promotes SRH non-radiative recombination. In InGaN LEDs, localized states, such as In-clusters can be formed [89, 90], which can be beneficial from carrier localization point of view. However, at high injection current, these states get saturated and can contribute to efficiency droop [91].

Polarization: Polarization significantly affects the performance of III-nitride devices. Due to the geometrical structure and lack of lattice matched substrate, both spontaneous and piezoelectric polarizations are present in III-nitride materials. A direct consequence of the polarization is the spatial separation of electrons and holes, which is known as

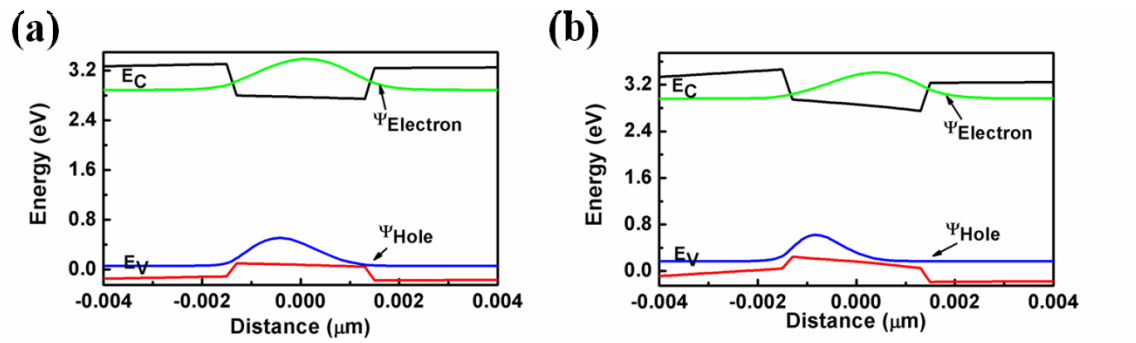

Figure 1.7 QCSE in a structure having (a) 10% polarization, and (b) 35% polarization. QCSE is more pronounced in the structure having higher polarization.

QCSE, as presented in Fig. 1.7. Due to the spatial separation of electrons and holes, the radiative recombination rate decreases which degrades the performance of LEDs.

Poor Hole Transport: In III-nitride materials, the effective mass of hole is larger than that of electron resulting in lower mobility of hole. This poor hole mobility causes non-uniform carrier distribution in active region of the LED. The holes are mostly located close to the *p*-GaN side. This is more enhanced in planar structure due to the presence of larger polarization field. This non-uniformity not only reduces the radiative recombination rate but also promotes electron overflow and Auger recombination, which further degrades the device performance. Several approaches have been investigated to circumvent this problem. The barrier thickness variation [92], insertion of a thin layer next to *p*-GaN layer [93], and *p*-doped active region are the names of a few.

Auger Recombination: Auger recombination refers to a three-carrier non-radiative recombination process. In this process, the excess energy released by the recombination of an electron-hole pair (EHP) is transferred to a third carrier as kinetic energy. This third carrier is then excited to a higher state in the same energy band and subsequently, relaxes to the respective band-edge releasing the energy. The probability of Auger recombination is proportional to the third power of carrier concentration ($R_{Auger} = Cn^3$) and thus is more prominent at high injection current. Although the direct intraband Auger recombination cannot be held responsible for the large efficiency droop observed in III-nitride materials, the scattering induced indirect Auger recombination can explain this large droop [94]. The electron-phonon interaction [95], alloy-induced-symmetry-reduction in InGaN active regions, and charge defects are some of the scattering

mechanisms that assist indirect Auger recombination. Considering the indirect Auger recombination, the coefficient of Auger recombination can be as high as ~10^{-31} $cm^6 \cdot s^{-1}$ for InGaN alloys [96-98].

Electron Overflow: Electron overflow refers to the escape of electrons from the active region. This reduces the radiative recombination rate and thus degrades the device performance. In III-nitride Ga-polar materials, due to the presence of the polarization field, the band-edge is tilted downward towards the *p*-GaN region, effectively reducing the barrier height for electrons. The non-uniform hole distribution also enhances electron overflow. These electrons can recombine with the holes in the *p*-GaN region, further degrading the device performance. In this context, an electron blocking layer (EBL) of high band gap material can be inserted between the last quantum wells (QW) and the *p*-GaN region to increase the barrier height for the electrons of the active region [99]. However, the effectiveness of this approach is limited by the presence of polarization field and the carrier injection level.

These shortcomings of III-nitride LEDs can be mitigated largely by employing nanowire structures. As mentioned in Section 1.1, nanowire structures offer less strain and polarization effects compared to the planar structure. Motivated by this, there has been substantial research going on to develop GaN based nanowire LEDs. The studies on InGaN/GaN multiple QW (MQW) heterostructures and dot-in-a-wire structures have been presented in [12, 100-110]. These studies present the comparison with thin film structures and the results indicate the superior performance of the nanowire structures. For example, the study in [101] showed a hundred times improvement in the photoluminescence (PL) intensity of InGaN/GaN MQW nano-column structure compared to the planar structure. The wavelength tunability by changing the growth condition is presented in [101, 105, 107]. High brightness nanowire LEDs, with comparable performance with planar structure at ~470 nm has been demonstrated in [105]. The reduced efficiency droop has been demonstrated in the dot-in-a-wire structure [109, 110]. It has been reported in [110] that *p*-modulation doped nanowire LEDs show virtually zero efficiency droop at a very high current density of 640 $A \cdot cm^{-2}$. The electron overflow problem can be mitigated by inserting a high bandgap AlGaN EBL next to the last *p*-GaN barrier [109]. The *p*-doping of the EBL also facilitates the hole injection and transport.

The study in [109] has shown that by incorporating *p*-type modulation doping and EBL, it is possible to achieve zero efficiency droop at an injection current as high as 2200 $A \cdot cm^{-2}$. Another significant advantage of these nanowire heterostructure LEDs is the flexibility to tune the spectral power distribution (SPD) of the emitted light. As the demand of solid state lighting increases, it has become progressively important to investigate the functional properties, such as color rendering index (CRI), and correlated color temperature (CCT) of white LEDs. In nanowire structures, it is fairly simple to incorporate different In compositions at different dots and hence, change the emission spectra by changing the growth conditions, such as the substrate temperature and/or In/Ga flux ratio. This is important to achieve the desirable CRI and CCT values, which are very important functional properties for LEDs as lighting and display applications.

1.3 Ultraviolet LEDs

As the technology advances, the UV emission is becoming more and more important in various applications, such as sterilization/ disinfection, water and air purification, medical instrumentation, biological sensors, and protein analysis. At present, mercury and Xenon lamps are used as a source of UV emission for these applications. However, these lamps are bulky and expensive, have limited lifetime, and require high voltage operation. Moreover, the emission wavelength cannot be tuned and they cause environmental pollution due to the presence of mercury [13]. On the other hand, LEDs are small in size, cheaper and mercury free, have long life time, and can be operated at low or moderate voltage. LEDs also offer the tunability of emission wavelength by bandgap engineering. It has been projected by Yole Développement in 2012 that the UV LED market will grow 43% by 2017 and reach nearly 270 million dollars [111-113].

1.3.1 Ultraviolet LEDs: The Challenges

The UV emission wavelength can be divided into three parts: UV-A (315 – 420 nm), UV-B (280 – 315 nm), and UV-C (100 – 280 nm). As we move closer to the deep UV range, it becomes more and more difficult to have high performance LEDs. The main reasons are summarized in the following paragraphs.

Crystal Quality: As mentioned in Section 1.1, due to the absence of lattice matched substrate, III-nitride LEDs are generally grown on SiC, sapphire, or Si substrate. These substrates have different lattice constants and thermal expansion coefficients. As a result, threading dislocations (TD) and defects are formed during the growth. For AlGaN, the lattice mismatch is even larger than GaN based LEDs and it can be so severe as to crack the nitride films [13]. Several approaches have been explored to reduce the extent of this problem. Insertion of a low temperature AlGaN/AlN layer [114, 115], pulse atomic layer deposition (PALE) technique to grow high quality AlGaN[116-118], and the epitaxial lateral overgrowth (ELO) [119-121] are some of the approaches. ELO is considered as one of the most successful approaches. In this method, a buffer layer is first grown on the substrate and then is covered by a thin masking film with narrow seeding window. Epitaxial growth is performed on this partially masked substrate. Initially, the epilayer starts to grow in a direction normal to the substrate by selective nucleation on the seeds. However, when the growing epitaxial layer exceeds the top surface of the mask, lateral growth initiates. The mask eventually allows the propagation of dislocations from the buffer layer to the laterally grown layer through very narrow windows and thus, reduces the dislocation density. Using this approach, it is possible to reduce the dislocation density of GaN and AlN grown on sapphire substrate from ~10^{8-9} cm^{-2} to the order of 10^{5-6} cm^{-2} and from 10^{10} cm^{-2} to 10^{9} cm^{-2}, respectively [116, 122]. The growth of AlGaN deep UV LEDs on bulk AlN substrate has also been studied [123-129]. Lower dislocation density (<10^{6} cm^{-2} for AlGaN LEDs on AlN substrate [128]) and improvement in output power (twice output power compared to the device grown on sapphire [125]) has been reported in these studies. In comparison to these techniques, nanowire structures can be a suitable alternative for UV LED application. As mentioned previously, due to the effective strain relaxation in the lateral dimension, nanowires have fewer dislocations, and as a consequence, the crystal quality is significantly better than thin film and they are less vulnerable to dislocations and cracking.

Different Growth Kinetics of Al Adatoms: The growth kinetics of AlGaN material system is different from GaN [13]. Al adatoms have larger sticking coefficient than Ga adatoms. During the layer by layer epitaxial growth, Al adatoms tend to cause islands to

nucleate, rather than forming steps by incorporating in the energetically favorable lattice sites. This disturbs the epitaxial growth, resulting in dislocations and grain boundaries.

Difficulty in Impurity Doping: Efficient doping is very difficult for AlGaN material systems. The ionization energy of the dopants increases almost linearly with the increase of the band gap and becomes very high, especially, for acceptor dopants. Mg is the most commonly used acceptor for III-nitride materials. Mg-ionization energy for GaN is ~250 meV, whereas it is ~600 meV for AlN [130]. This high activation energy results in inefficient *p*-doping and as a result, conductivity of the devices decreases. However, to have high performance device, electrical conductivity is a prime issue. Many approaches have been proposed to increase the efficiency of *p*-doping, such as polarization induced hole doping [131, 132], tunnel junction [133, 134], and Mg-delta doping [135].

Light Extraction: The valence band profile of AlN presents negative crystal field splitting (-219 meV) [136]. The valence band order of the A, B, and C bands of AlN near the Γ point is Γ_7, Γ_9, and Γ_7. Therefore, the recombination between the electrons from the conduction band with the holes in the top valence band is polarized transverse magnetically (TM), parallel to the *c*-axis ($E \parallel c$). On the contrary, the GaN structure possesses positive crystal field splitting (+38 meV) [136]. The valence band order of A, B, and C bands near the Γ point for GaN is Γ_9, Γ_7, and Γ_7. Therefore, the emitted light is polarized transverse electrically (TE), perpendicular to the *c*-axis ($E \perp c$). The band structures of AlN and GaN are presented in Fig. 1.8. For the ternary compound $Al_xGa_{1-x}N$, as the Al molar fraction increases from 0 to 1, the crystal field splitting decreases from 38 meV to -219 meV. Accordingly, the polarization of the emitted light changes from TE to TM with increasing Al molar fraction. It has been presented that the crossover between TE and TM polarization occurs at an Al molar fraction of 0.25 [137]. The polarization (and hence, the crossover point) also depends on the strain and the internal electric field present in the structure [138-142]. Since the epitaxial layers are grown along the *c*-direction, TE polarization is preferable for surface emitting LEDs. Due to the presence of TM polarization in deep UV LEDs, the photons cannot be easily extracted resulting in poor light extraction efficiency.

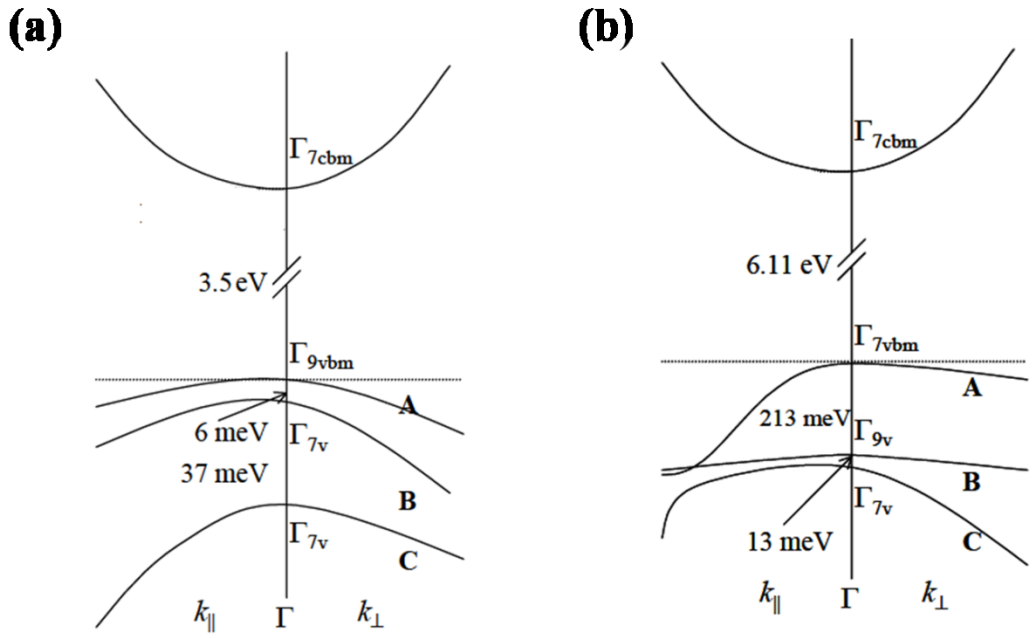

Figure 1.8 Band structure near Γ point: (a) wurtzite GaN, and (b) wurtzite AlN.

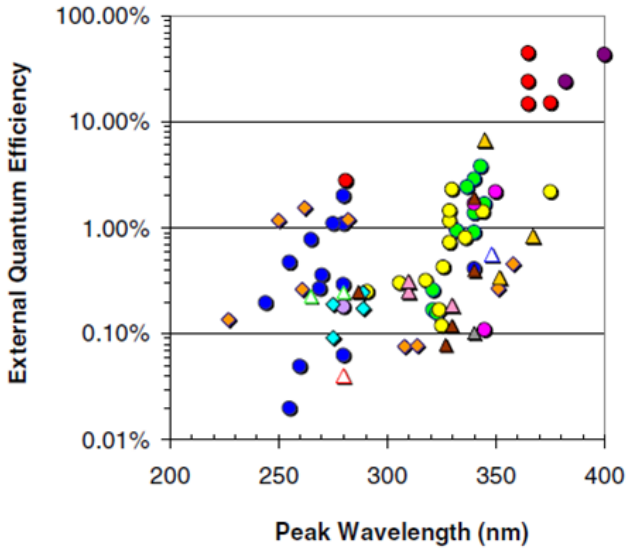

Figure 1.9 State of the art EQE of UV LEDs [14]. The EQE is ~0.1% for UV emission at wavelengths smaller than 250 nm.

For the above mentioned reasons, the power output and EQE is very low for deep UV (DUV) LEDs. Figure 1.9 presents the EQE for UV LEDs operating at different wavelength regions [14]. For a UV LED operating below 250 nm, the EQE is only ~0.1%. Such poor performance is not adequate for practical application. EQE is a performance metric combining injection efficiency, IQE, and light extraction efficiency. Let us consider these three efficiencies individually for large band gap material. As mentioned in Section 1.2, the holes are distributed non-uniformly in the active region due to low hole mobility and polarization effect. Apart from this, the hetero-interface of AlGaN/GaN also hinders efficient hole injection in the active region. Since it is very difficult to form ohmic contact for AlGaN, a thin GaN cap layer is often grown on top of AlGaN. The injected hole gets trapped at the hetero-interface of the GaN/AlGaN barrier and attracts electrons; which bypasses the active region and recombine non-radiatively in GaN region. This results in a very low hole injection in the active region. IQE is low due to the poor crystal quality and high densities of defects and dislocations.

The dependence of IQE on TDs for a 280 nm UV LED is simulated in [14] and is presented in Fig. 1.10. The dislocation density resulting from a non-optimized growth of AlGaN heterostructures on sapphire substrate is in the order of 10^{10} cm^{-2} and IQE for this high value of TDs is less than 10%, as shown in Fig. 1.10. Another challenge is to have enhanced light extraction efficiency. The conventional approach to form dome shaped structure using encapsulants may not result in improved performance in this case since most of the available encapsulants absorb light in the deep UV range. Furthermore, the emitted light is TM polarized due to the unique negative crystal field splitting property of AlN. This TM polarization of emitted light makes it more difficult to collect photons from the surface emitting LEDs and thus, reduces the light extraction efficiency.

1.3.2 Optical Properties of Ultraviolet LEDs

Due to the poor crystal quality and impurity dopant induced states in the bandgap, the presence of various peaks other than the band-edge peak is observed in the PL spectra. To understand the mechanism and to improve the performance of the device, it is imperative to understand the origin of these defect peaks. A study on these defect peaks is presented in this section.

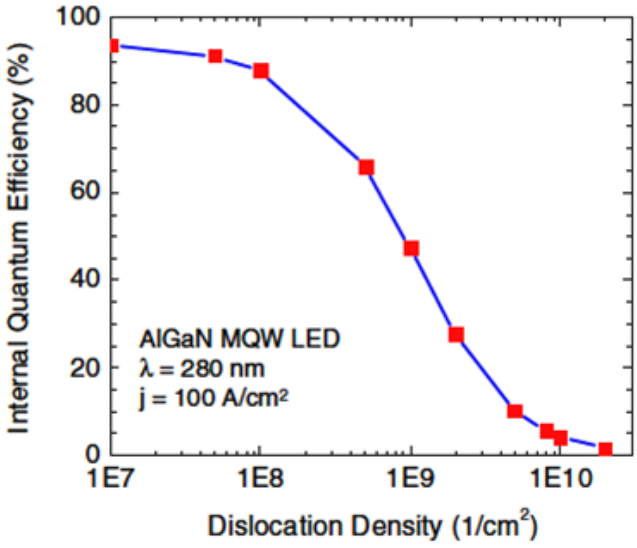

Figure 1.10 IQE versus threading dislocation density plot [14]. IQE is reduced significantly as the threading dislocation increases.

The origin of the defect peaks has been studied in [143-145]. The PL spectra of intrinsic and *n*-doped $Al_{0.3}Ga_{0.7}N$ are presented in Fig. 1.11. It is apparent from Fig. 1.11 that both intrinsic and *n*-doped $Al_{0.3}Ga_{0.7}N$ have a near band edge emission peak at 295 nm, but a blue emission peak is present for *n*-doped $Al_{0.3}Ga_{0.7}N$ at 450 nm. This peak is present in the intrinsic $Al_{0.3}Ga_{0.7}N$ also, but the intensity is about two orders of magnitude lower than the *n*-doped sample. The reason of this defect peak emission is the deep levels introduced by the dopant impurity. A theoretical model is presented in [144], where the deep level concentrations are divided into two parts: (a) neutral or unoccupied (N_0) and (b) negative or occupied (N_T). Any transition between conduction/ valence band and any of these two levels cause the broad emission peak at 450 nm.

The problem of defect peak is more prominent in the case of Mg-doping. Incorporation of Mg-dopant introduces strong compensating intrinsic defects, thus originating defect peaks and lowering the electrical conductivity. A systematic study of these defect peaks is presented in [130]. The near band-edge and defect peaks of *p*-$Al_xGa_{1-x}N$ alloys having different alloy compositions ($x = 0 \sim 1$) are presented in Fig. 1.12 [130]. *p*-GaN has a defect peak at 2.81 eV, which is due to the donor-acceptor pair (DAP) transition between a deep level donor and Mg-acceptor. As the Al molar fraction increases, the defect peak

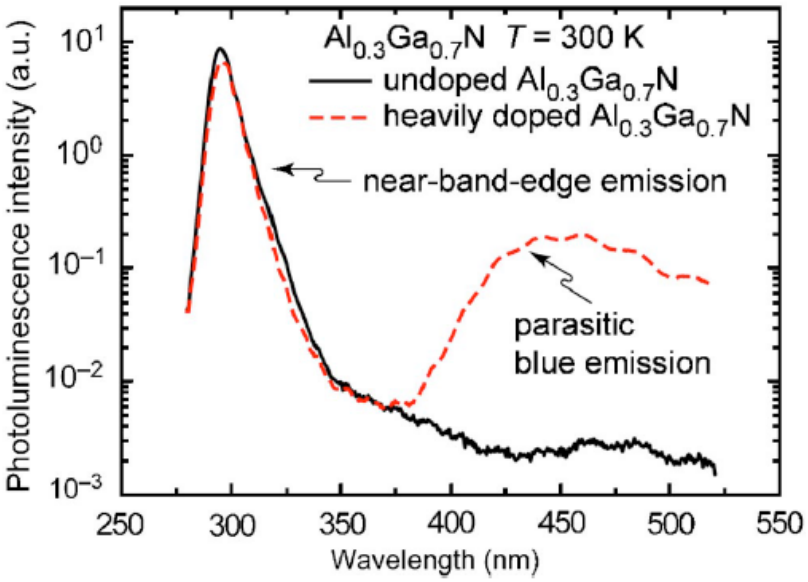

Figure 1.11 Room temperature PL spectra of intrinsic and *n*-doped $Al_{0.3}Ga_{0.7}N$ [144]. A strong defect emission is observed for *n*-doped $Al_{0.3}Ga_{0.7}N$ at 450 nm.

is blue shifted and is at 4.7 eV for AlN. The presence of another two peaks, at 5.55 eV and at 6.02 eV is observed for AlN. The peak at 6.02 eV is due to the transition of exciton bound to the neutral Mg-acceptor and the peak at 5.55 eV is due to the transition between conduction band or shallow donor levels to neutral Mg-acceptor energy level. The peak position of 5.55 eV assigns the Mg-acceptor levels to be at 0.5 eV, which is consistent with the reported values of Mg-ionization energy [146]. This is a signature of the Mg-doping of AlN and this peak is also present at 5.31 eV and at 4.96 eV for $Al_{0.8}Ga_{0.2}N$ and $Al_{0.7}Ga_{0.3}N$, respectively.

As mentioned previously, the defect peaks are originated due to the presence of strong compensating defects. In Mg-doped AlN, nitrogen vacancies, both nitrogen vacancy with one positive charge (V_N^{1+}) and nitrogen vacancy with three positive charges (V_N^{3+}) work as the compensating defects. Nitrogen vacancy with two positive charges (V_N^{2+}) is unstable. The formation energy of nitrogen vacancies reduces as the Fermi level moves closer to the valence band and it is found that the formation energy of V_N^{3+} is lower than

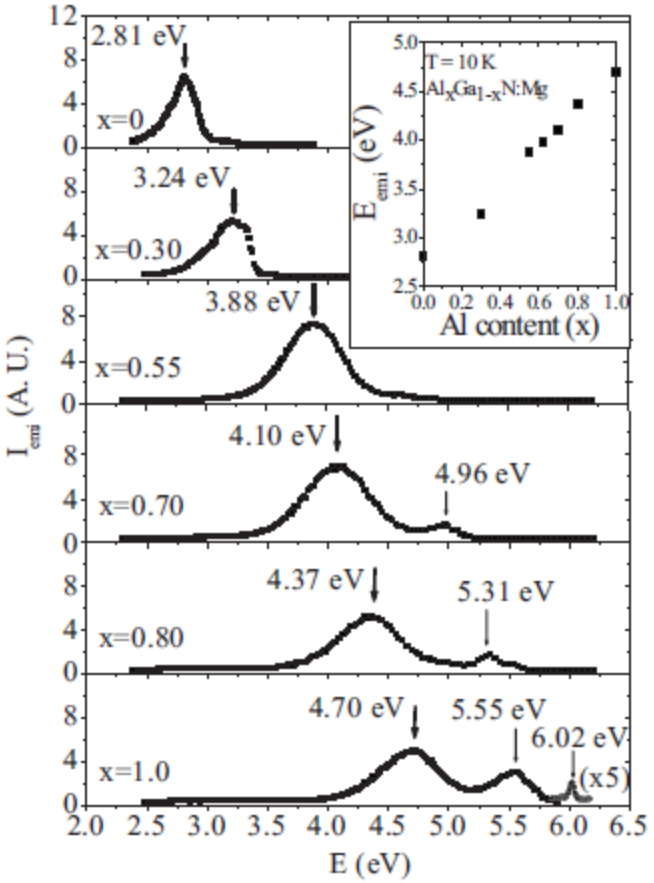

Figure 1.12 PL spectra of *p*-doped $Al_xGa_{1-x}N$ at 10 K having different alloy compositions [130].

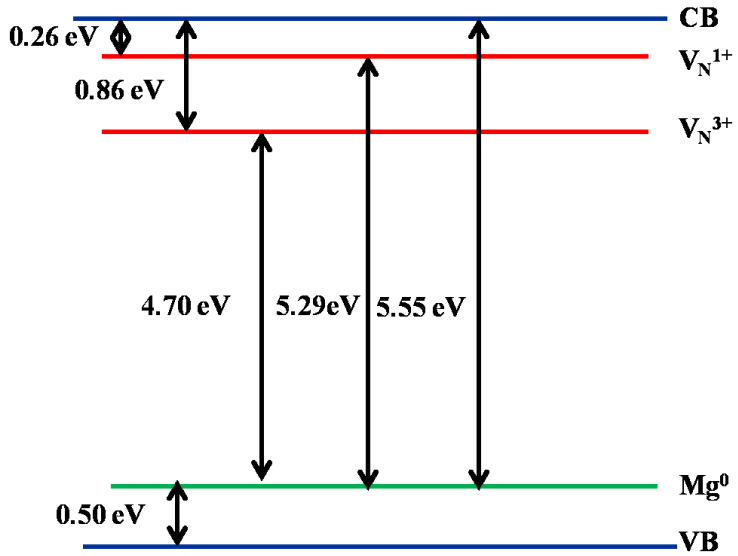

Figure 1.13 Energy band diagram of *p*-doped AlN, demonstrating the transition between nitrogen vacancies and Mg-acceptor energy level [147].

that of V_N^{1+} [147]. Thus the formation of V_N^{3+} is more favorable and the emission line at 4.7 eV is consistent with the transition involving V_N^{3+} and Mg-acceptor energy level. V_N^{1+} is shallower than V_N^{3+} and no emission line is observed concerning the transition of V_N^{1+} and Mg-acceptor energy level. A band diagram is constructed considering the nitrogen vacancy energy levels and is presented in Fig. 1.13 [147].

One of the key reasons of the low electrical conductivity of $Al_xGa_{1-x}N$ with high Al contents is the presence of these defects. By changing the growth condition it is possible to suppress the impurity transition. It has been presented in [130] that by increasing the V/III ratio, the impurity transition at 4.7 eV can be effectively suppressed. The Mg-doped $Al_{0.7}Ga_{0.3}N$ layer grown with higher V/III ratio exhibits relatively low resistivity of 10^5 Ω-cm, at room temperature. However, with the presence of 4.7 eV peak, it behaves like an insulator.

Another significant problem in achieving deep UV LED is the composition fluctuation. It is very difficult to grow deep UV LED having uniform Al composition throughout the active region. This phenomenon has been intensely studied for $Al_xGa_{1-x}N$ nanowires grown by plasma assisted MBE (PAMBE) [148-150]. Nanowires have better crystal quality than thin film and they are virtually defect free due to the lateral stress relaxation. Therefore, the reason for this localization is not due to any impurity transition. The temperature dependent PL spectra for $Al_xGa_{1-x}N$, with $x = 30\%,\ 50\%$, and 80% are presented in Fig. 1.14 [149].

The PL spectra of $Al_{0.3}Ga_{0.7}N$ and $Al_{0.5}Ga_{0.5}N$ exhibit single emission peak at all temperatures. However, the PL spectra of $Al_{0.8}Ga_{0.2}N$ shows two emission bands, the high energy band disappears at temperatures greater than 240 K but the low energy peak is present at all temperatures. The reason of different temperature quenching of these two peaks might be that the non-radiative centers become more active at higher temperatures for the high energy peak. The origin of the alloy fluctuation lies in the growth kinetics; which causes different nucleation mechanism for $Al_xGa_{1-x}N$ on top of GaN template. However, such fluctuation can be reduced by changing the growth temperature, which is experimentally reported in [150].

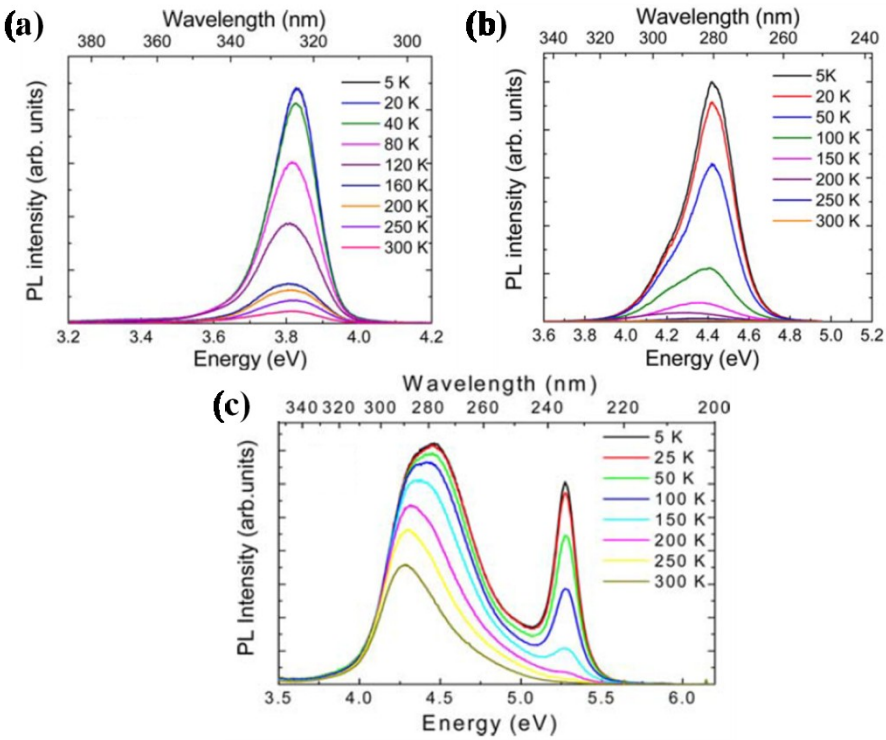

Figure 1.14 Temperature dependent PL spectra of $Al_xGa_{1-x}N$ having Al compositions of (a) 30%, (b) 50%, and (c) 80% [149].

1.4 Organization of the Thesis

In this thesis work, the functional properties of nanowire white LEDs and optical and electrical characteristics of nanowire UV LEDs have been intensely studied. We have demonstrated that our nanowire white LEDs can exhibit a CRI value as high as 97.7 in the warm white region. We have analyzed the surface state effects of nanowire LEDs and subsequently, designed core-shell structure with enhanced performance. The successful growth of AlN nanowires (non-doped and Mg-doped) with enhanced optical performance have been demonstrated. The achievement of deep UV emission at 210 nm has also been presented in this research work.

Chapter 1 presents an overview of the development of III-nitride nanowire based white and UV LEDs. The high density of defects and dislocations, presence of polarization field, electron overflow, and Auger recombination are the limiting factors for achieving high performance III-nitride planar devices. These limiting factors and the advantages of

nanowire structures in this context have been investigated in detail. The additional challenges associated with UV LEDs have also been discussed.

Chapter 2 describes the growth mechanism of III-nitride nanowires. The fabrication procedure of white and UV LEDs and the optical and electrical characterization techniques are also discussed.

In Chapter 3, the functional properties, such as CRI and CCT of InGaN/(Al)GaN nanowire white LEDs are investigated. We present that by changing the growth condition at the wafer level, it is possible to achieve a very high CRI value. Our nanowire LEDs present a CRI value of 97.7 in the warm white region and 95.6 in the cool white region. We also investigate the surface states effect of nanowire structures. We present that the surface passivation schemes can result in drastically improved performance. Our core-shell structure can exhibit two orders of magnitude higher power than the non-core-shell structure.

The non-doped and Mg-doped AlN nanowires are characterized in Chapter 4. We present the dislocation-free non-doped AlN nanowires with enhanced performance compared to the planar counterpart. We also report the achievement of controllable Mg-doping in AlN nanowires by changing the growth condition.

The optical and electrical performances of UV LEDs emitting at 340 nm, 290 nm, and 210 nm are presented in Chapter 5. The most important achievement described in this chapter is the demonstration of 210 nm emission from an AlN *p*-*i*-*n* nanowire structure. This is the first report of achieving deep UV emission in such a short wavelength range using nanowire structure.

Finally, summary of this thesis work and a guideline to future works are discussed in Chapter 6.

Chapter 2. Epitaxial Growth, Fabrication, and Characterization Methods for Nanowire LEDs

The detailed study of the performance characteristics of III-nitride nanowire LEDs is the main focus of this research work. In this chapter, the nanowire LED growth mechanism, fabrication process, and characterization principles are described, which provide the foundation for the subsequent chapters on the design and performance characterization of these unique devices. Our III-nitride nanowires are grown on Si substrate by PAMBE, fabricated, and then subsequently characterized, both optically and electrically. Before growing the nanowire structures, the characteristics are investigated by simulating the structure. In what follows, the nanowire growth mechanism, fabrication procedure, and the optical and electrical characterization techniques are discussed in detail. A brief description of the software tool has also been provided.

2.1 Plasma Assisted Molecular Beam Epitaxial Growth of Nanowire LEDs

The two methods to grow nanowires are the bottom-up approach and the top-down approach. In the top-down approach, the nanowires are fabricated from the epitaxial structures using dry etching, wet chemical etching, or reactive ion beam etching [151-154]. However, the structural quality of such nanowires is largely limited by the etching method employed, the etching induced defects and the presence of dislocations of the bulk materials. On the other hand, the bottom-up approach can offer, in principle, virtually dislocation free nanowires. It is possible to achieve nanowires with atomic perfection in both lateral direction and growth direction by changing the growth conditions. Vapour-liquid-solid (VLS) phase epitaxy [155], selective area growth (SAG) [156-158], and the spontaneous growth of nanowires under nitrogen rich conditions [159, 160] are the methods commonly employed in the bottom-up approach.

In our work, III-nitride nanowires are grown by catalyst-free PAMBE under nitrogen rich conditions. MBE has the advantage to grow high purity material with atomically flat interface. Furthermore catalyst-free MBE offers the advantage of increased material purity because of the absence of any foreign metal catalyst. In PAMBE, radio frequency

(RF) plasma is used to create atomic nitrogen (N) species from nitrogen molecule (N_2). This catalyst-free or self-catalytic growth process is a diffusion induced growth process wherein the differences in diffusion coefficients, surface energies, sticking coefficients cause the growth of nanowires [160]. The length, diameter, shape of nanowires, wire density and uniformity depend on the growth conditions, such as, III/V flux ratio, substrate temperature, and growth rate. For instance, nanowire density, and Ga nucleation density (in case of GaN nanowire growth) can be controlled by adjusting the growth temperature [161], and the III/V flux ratio [162], respectively.

All the nanowire heterostructures discussed in this thesis are grown by the Veeco Gen II MBE system equipped with a RF plasma assisted nitrogen source. The image of the MBE system is presented in Fig. 2.1. Three main vacuum chambers namely an introduction chamber, a buffer chamber, and a growth chamber comprises the MBE system. The Si substrates, after cleaning by hydro-fluoric acid (HF), are loaded into the introduction chamber and subsequently transferred to the buffer and growth chamber after proper degassing. Group III elements (Ga, In, Al) reside in the effusion cells and are thermally evaporated by heating the effusion cells. Plasma assisted radio frequency excitation provides the N source. The group III fluxes are controlled by changing the effusion cell

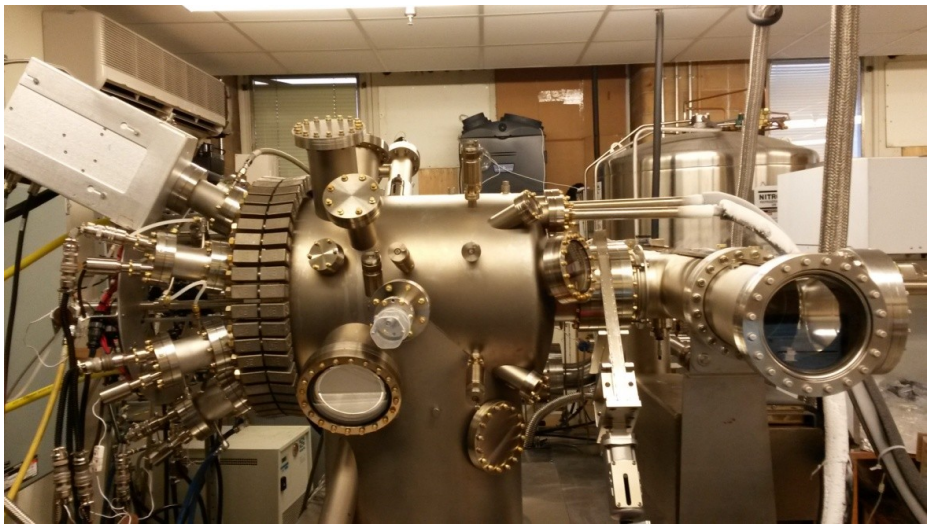

Figure 2.1 A Veeco Gen II MBE system equipped with a radio frequency plasma assisted nitrogen source (located at the department of Electrical and Computer Engineering, McGill University).

temperatures whereas the amount of N plasma is controlled by adjusting the plasma power and nitrogen flow rate. When the effusion cells are heated, the group III atoms impinge on the substrate surface to react with the active nitrogen to form the III-nitride materials.

2.2 Fabrication Procedure

In this section, the fabrication procedure of nanowire white and UV LEDs is discussed. The fabrication procedure is almost the same for both white and UV LEDs. However, for white LED fabrication, polyimide and indium tin oxide (ITO) are used for planarization and current spreading, respectively. Neither polyimide nor ITO is transparent in the deep UV range. Furthermore, the top metal contact also absorbs deep UV emission. Therefore, the fabrication of nanowire UV LEDs is more challenging and requires special care.

2.2.1 Nanowire White LED Fabrication

For white LED fabrication, the nanowires are first spin coated by polyimide resist layer for passivation and planarization. The top of the nanowires is revealed by performing O_2 dry etching of the nanowires followed by standard photolithography to pattern the samples into various sizes (0.1×0.1 mm^2, 0.3×0.3 mm^2, 0.5×0.5 mm^2, and 1×1 mm^2). The top and bottom metal contacts are then deposited. The top *p*-metal contact is composed of Ni (5 nm)/ Au (5 nm)/ indium tin oxide (ITO: 200 nm), whereas, Ti (20 nm)/ Au (120 nm) forms the bottom *n*-contact. ITO layer works as the current spreading layer. To facilitate hole transport, metal grid patterns are deposited on the device surface. The fabricated devices with top and bottom contacts are annealed at 500 °C in nitrogen ambient for 1 minute, followed by a second annealing at 300 °C in vacuum for one hour after ITO deposition. The schematic diagram and the optical image of the fabricated devices are illustrated in Fig. 2.2(a) and Fig. 2.2(b), respectively.

2.2.2 Nanowire UV LED Fabrication

The nanowire UV LED fabrication is more challenging than the white LED fabrication. In white LED, polyimide is used for planarization and passivation. However, polyimide is not transparent in the deep UV range and cannot be used for deep UV LED fabrication.

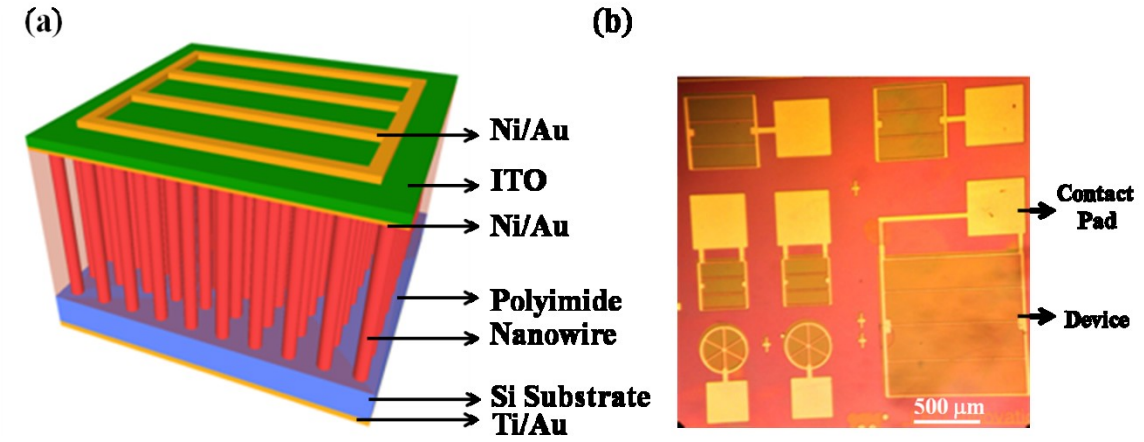

Figure 2.2 (a) Schematic diagram of the fabricated white LED. (b) Optical image of the fabricated white LED devices. The device sizes are: 1 × 1 mm^2, 0.5 × 0.5 mm^2, 0.3 × 0.3 mm^2, and 0.1 × 0.1 mm^2.

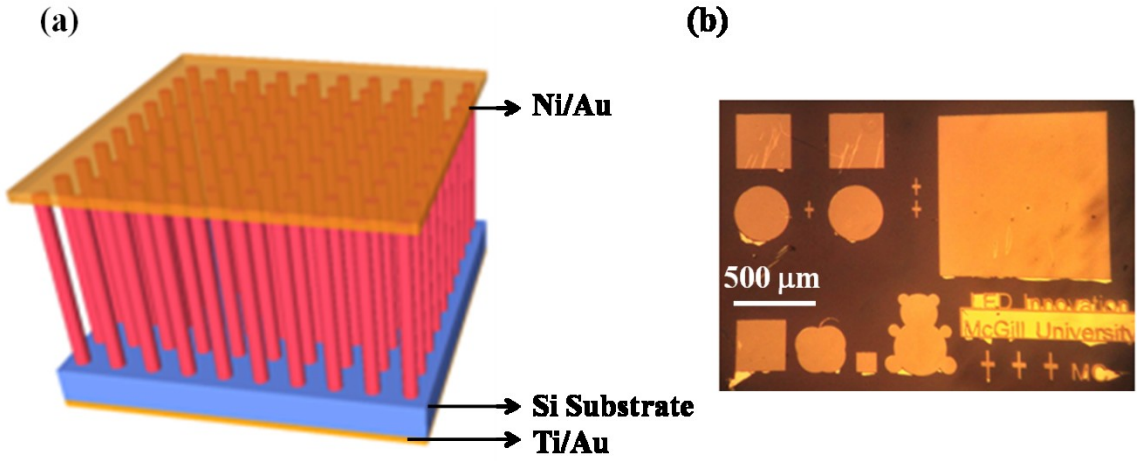

Figure 2.3 (a) Schematic diagram of the fabricated UV LED. (b) Optical image of the fabricated UV LED devices. The device sizes are: 1 × 1 mm^2, 0.5 × 0.5 mm^2, 0.3 × 0.3 mm^2, and 0.1 × 0.1 mm^2.

The AlN nanowire LED fabrication consists of back and front metal contact deposition. Ti (10 nm)/ Au (30 nm) and Ni (15 nm)/ Au (15 nm) are deposited as the bottom and top contacts, respectively. The top metal contact is deposited at a tilting angle of 30°. The schematic diagram and the optical image of the fabricated devices are illustrated in Fig. 2.3(a) and Fig. 2.3(b), respectively.

The nanowire deep UV LED fabrication method is at its infancy and needs to be optimized to ensure good device performance. For instance, deep UV transparent polymer should be used for planarization and passivation. Furthermore, Ni/Au layer is used as the front *p*-metal contact, but Ni/Au is semi-transparent in the UV range. Replacing this with a UV transparent electrode can enhance the light extraction efficiency to a great extent. There are not many transparent conductors in the deep UV range. The use of *p*-type diamond and $\beta - Ga_2O_3$ as UV-transparent *p*-electrode should be considered in this context [163].

2.3 Luminescence Studies

Luminescence, in general, is the spontaneous emission of light under excitation. Luminescence is classified according to the excitation mechanism. If the excitation is achieved by the injection of photons it is called photoluminescence (PL); if by the action of electron bombardment it is called cathodoluminescence (CL); if by the action of an electric field or injection with a *p-n* junction it is called electroluminescence (EL). In this work, PL and EL are used as probes to study the optical and electrical properties of nanowire LEDs.

2.3.1 Photoluminescence Studies

In photoluminescence spectroscopy, light is used as the excitation source. When light is incident on the material, photon is absorbed and excites electrons from the conduction band to the valence band and EHP is generated. The electrons and holes relax to the respective band edges by phonon emission and then recombine across the band gap. The recombination could be radiative or non-radiative. In radiative recombination process, a photon is emitted following the annihilation of an EHP. The radiative recombination process is more prominent in direct band gap semiconductors. In indirect band gap

semiconductors, the additional assistance of a phonon is required to conserve the momentum, resulting in extremely low efficiency. Therefore, indirect band gap materials are not suitable for optoelectronic device applications. In the case of non-radiative recombination, the energy is dissipated as heat through the emission of phonon.

The radiative recombination process can take place across the band gap of the semiconductor through various transition mechanisms. These transitions are described briefly in the following paragraphs and are presented in Fig. 2.4.

Band-to-Band Transition (Porcess A): Band-to-band transition refers to the radiative recombination of an electron in the conduction band with a hole in the valence band. This can occur in very pure crystals at relatively high temperatures. When impurity is introduced in the material (either intentionally or unintentionally), states are created in the energy band. Electrons and holes are trapped in those states and can recombine with each other radiatively or non-radiatively. These transitions will be discussed below (Processes E, F, and G). On the other hand, at low temperature, the band-to-band transition transfers to excitonic transition as discussed below (Processes B, C, and D).

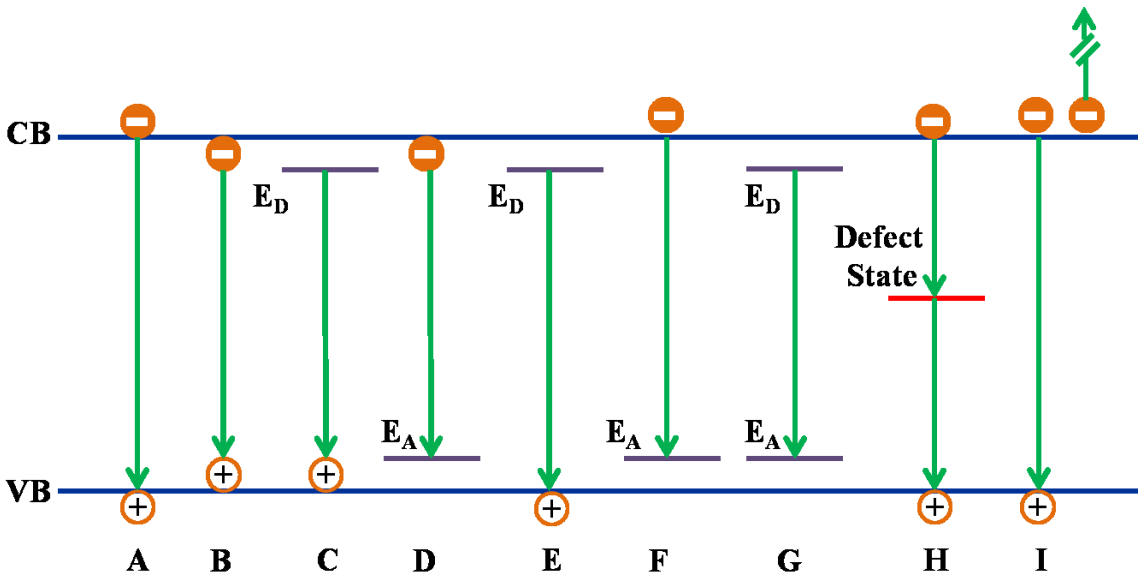

Figure 2.4 Radiative and non-radiative optical transitions; Radiative transitions: A: band to band ($h\upsilon = E_g$), B: free exciton ($h\upsilon = E_g - E_X$), C and D: bound exciton ($h\upsilon = E_g - E_X - E_b$), E: donor to valence band ($h\upsilon = E_g - E_D$), F: conduction band to acceptor band ($h\upsilon = E_g - E_A$), G: donor-acceptor pair ($h\upsilon = E_g - (E_D + E_A) + q^2/\varepsilon r$); Non-radiative transitions: H: defect state related, and I: Auger recombination.

Excitonic Transition (Processes B, C, and D): Both free and bound excitonic transitions are observed at low temperature in a very pure crystal. The free exciton is composed of an electron in the conduction band and a hole in the valence band bound together by Coulomb interaction. Photon ($h\upsilon = E_g - E_x$) is emitted by the recombination of electron and hole. The emission spectrum is sharp since the exciton levels are well defined.

Bound excitonic transitions are observed in intentionally doped high purity material. The exciton can be bound with an impurity atom (either donor or acceptor). The energy of the bound exciton is lower than the free exciton energy by the binding energy of the exciton to the impurity ($h\upsilon = E_g - E_x - E_b$).

Excitonic transitions are often observed at low temperatures, where the binding energy of the exciton is larger than the thermal energy. As the temperature increases (thermal energy becomes greater than the binding energy), the excitons become unstable and band-to-band transitions are observed in the PL spectra.

Band-Edge to Donor/Acceptor Transition (Processes E and F): This process refers to the transition of a free carrier to a bound carrier and is commonly observed in semiconductor materials. The transition involves the recombination of an electron in the conduction band to the neutral acceptor or the recombination of neutral donor to a valence band hole ($h\upsilon = E_g - E_D$ or $h\upsilon = E_g - E_A$).

Donor-Acceptor Pair (DAP) Transition (Process G): In DAP transition, the recombination occurs when an electron moves from the neutral donor to the neutral acceptor. Since both donor and acceptor are ionized after such a transition, Coulomb attractive force works between them and therefore, the energy of the emitted photon is, $h\upsilon = E_g - E_A - E_D + \frac{q^2}{\varepsilon r}$, where q is the elementary charge, ε is the dielectric constant, and r is the donor-acceptor distance. Since the photon energy depends on r and r can vary in a large range, the DAP transition results in a broad emission spectrum.

Non-Radiative Recombination (Processes H and I)*:* Non-radiative recombinations are originated, in most of the cases, due to the presence of defects in the crystal. These defects include dislocations, vacancies, interstitials, and foreign atoms. These defects have energy levels within the band gap of the semiconductor. The transition between the

carriers (electrons and/or holes) to these defect levels results in the emission of a phonon, which is dissipated as heat.

Another important non-radiative recombination process is Auger recombination. In Auger recombination, the energy due to the recombination of an EHP is used to excite another carrier, which transits to a higher energy level in the same band. This excited carrier then relaxes back to the respective band-edge by losing the energy by multiple phonon emission. The energy and momentum is also conserved for Auger recombination. Auger recombination is dominant at very high excitation intensity or high carrier injection currents and can be neglected at lower carrier concentration.

2.3.2 Electroluminescence Studies

Electroluminescence refers to the radiative recombination due to the injection of the minority carriers into a semiconductor *p*-*n* junction. Electroluminescence study is performed on the fully fabricated device. The basic principle of EL for a *p*-*n* junction is briefly summarized below.

The energy band diagram of a *p*-*n* junction is presented in Fig. 2.5. When the *p*-*n* junction is formed, the electrons (holes) from the *n*- (*p*-) region diffuse to the *p*- (*n*-) region. This results in the formation of positive (negative) space charge in the *n*- (*p*-) region. In the vicinity of the interface, an electric field is established from *n*- to *p*- region. This electric field prevents further diffusion of carriers to the opposite end and thus establishes an equilibrium condition. The Fermi levels are equalized and a potential barrier sets in from *n*- to *p*- region. The electric field is localized in a narrow region near the junction. This narrow region is depleted of any free carriers and is called the depletion region. When a forward bias voltage is applied to this *p*-*n* junction, both the depletion width and the internal potential barrier decreases and the excess electrons (holes) are injected from the *n*- (*p*-) region to the *p*- (*n*-) region. Recombination is initiated due to such mixing of high concentration of minority and majority carriers. If the recombination is radiative, the resulting luminescence is called electroluminescence.

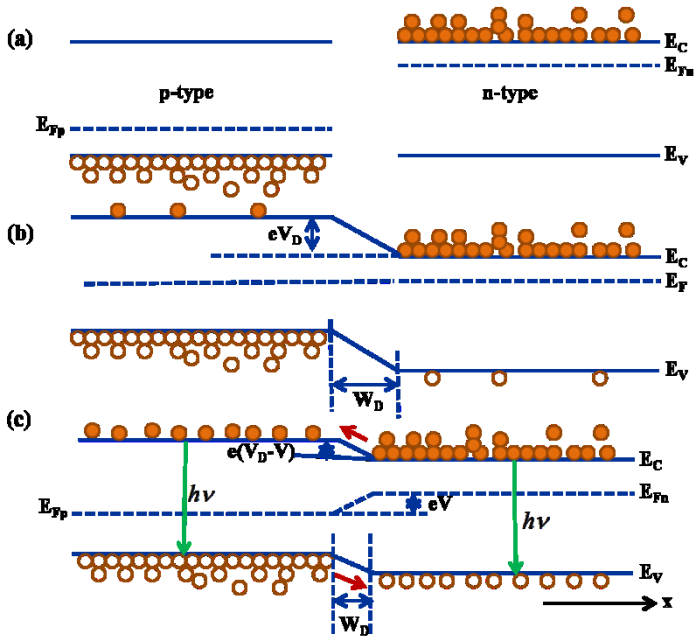

Figure 2.5 Energy band diagram of a *p-n* homojunction; (a) separated *p-* and *n-*semiconductor, (b) the *p-n* junction with zero applied bias (W_D is the depletion width and eV_D is the potential barrier), (c) the *p-n* junction with an applied forward bias voltage of V [164].

2.3.3 Importance of PL and EL Spectroscopy

A plethora of information can be revealed by analyzing the PL and EL spectra, which is discussed in the following paragraphs.

Band gap: PL can be used to determine semiconductor band gap. The peak position of the PL spectra corresponds to the band gap of the semiconductor in most cases. For ternary alloys, the alloy composition can also be determined employing the Vegard's law. However, band gap depends on carrier concentration and may be reduced under heavy doping, due to the band tailing effect. Also the PL peak in a heavily doped semiconductor may show higher energy than the bandgap, due to the Burstein-Moss effect. Therefore, such band gap determination is dependent on the doping level of the material.

Stress: Stress is an important issue for III-nitride materials since they are grown by lattice-mismatched heteroepitaxy. Due to the mismatch in lattice constants and thermal expansion coefficients between the epitaxial layer and the substrate, the epitaxial layer experiences strain. If the lattice constant of the epitaxial layer is larger (smaller) than the substrate, it experiences biaxial compressive (tensile) stress which can be decomposed in

two components: a hydrostatic component and a uniaxial component. The hydrostatic component alters the lattice constant, which changes the band gap and therefore, a shift in the PL peak position is observed. The uniaxial component affects the valence band degeneracy at zone-center ($\Gamma = 0$), often resulting in the splitting of the valence bands into light hole and heavy hole sub-bands. Since these bands participate in carrier excitation and recombination, any change in their order is observed in the PL spectrum; either by a shift in the peak position or by the splitting of single PL peak into multiple peaks. Thus PL can effectively probe the effect of strain in the material. PL spectroscopy can also be used to quantitatively measure the magnitude and direction of the strain [165].

Crystal Quality: Material quality can be estimated by the intensity and full-width-at-half-maxima (FWHM) of the PL signal. A strong intensity and narrow FWHM corresponds to good material quality. This can be additionally supported by the absence of any defect related peaks.

IQE and EQE: IQE (η_{IQE}) and EQE (η_{EQE}) are two important performance metrics for optoelectronic devices. Fundamentally, EQE can be expressed as the ratio of the number of photons emitted into free space per unit time to the number of electrons injected to the device per unit time. For LEDs, it is a combination of injection efficiency (η_{inj}), η_{IQE}, and light extraction efficiency (η_{ext}), i.e., $\eta_{EQE} = \eta_{inj}\eta_{IQE}\eta_{ext}$. η_{inj} is defined as the ratio of the injected electron to the active region to the total number of electrons injected into the device. η_{inj} is considered unity for planar structure; however, as will be discussed in Chapter 3, η_{inj} is very low for nanowire structures with the presence of surface recombination. η_{IQE} is defined as the ratio of the number of photons emitted from the active region per second to the number of electrons injected in the active region per second. In LEDs, not all the photons recombined radiatively can escape the device and emit into the free space. As discussed in Chapter 1, the light extraction efficiency is limited by the total internal reflection of the emitted photon and can be as low as 4% for a typical planar structure [58]. This affects severely the device performance and therefore, aptly included in the EQE calculation.

The IQE can be deduced from the temperature dependent PL/EL measurement. This deduction of η_{IQE} is based on the assumption that at cryogenic temperature the defect related recombination is nearly zero due to thermal freeze-out effect. Therefore, the PL/EL intensity is at its maximum value at low temperature. η_{IQE} is calculated as the ratio of room temperature integrated PL/EL intensity to the low temperature integrated PL/EL intensity. However, it should be mentioned that this assumption might not be true for all material systems. For instance, it has been reported that the PL intensity of InGaN LED is not always saturated at low temperature [166]. Furthermore, IQE calculated in this method depends on the excitation level and the doping density of the material [167, 168].

The EQE can be calculated from the power dependent PL/EL measurement. The rate of the increase of the integrated intensity with increasing power gives the estimation of η_{EQE} . For III-nitride LEDs, η_{EQE} generally shows droop at higher injection current. Electron overflow, Auger recombination, inhomogeneous carrier distribution, etc. have been identified as the cause of the droop, as discussed in Chapter 1. The QCSE can also be estimated from the power dependent PL/EL measurement by observing the shift in the peak position with increasing power.

CRI: CRI is an important functional property of white light sources. It defines the color rendering ability of the light source. It depends on the spectral power distribution of the light source and can be derived from the EL spectrum. Conventionally, Planckian black body radiator is assumed to have a CRI of 100. The CRI of the light source is calculated by comparing the color rendering of the light source to that of a reference source. Eight standard color samples are illuminated by the test light source and the reference source. The standard color samples are presented in Fig. 2.6. The CRI of the i-th sample is defined by, $CRI_i = 100 - \Delta C_i$, where ΔC_i represents the quantitative color change of the sample when illuminated by the reference and the test light source. The general CRI is then calculated by averaging these special eight CRI's, i.e., $CRI = \frac{1}{8}\sum_{i=1}^{8} CRI_i$. The smaller the color deviation (ΔC) between the two sources, the higher the CRI value of the light source. The CRI is very high if the SPD of the light source closely resembles the black body radiation spectrum.

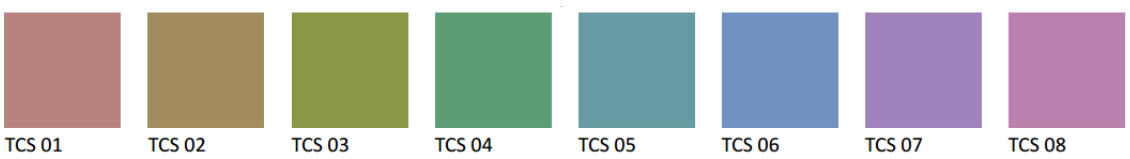

Figure 2.6 The eight reference color samples used to calculate CRI of the light source [169].

2.4 APSYS Simulation Tool

Simulation tools help us to optimize the design and understand the device characteristics and performance by critically correlating the simulation results with the experimental data. For instance, polarization effect is significant in III-nitride materials and more prominent in planar structure than nanowire structure. How this polarization affects the carrier distribution and radiative recombination can be understood clearly by analyzing the band structure, wave function, and carrier distribution obtained by simulating the structure. The extent of polarization also depends on the structure of the device, such as the thickness of the quantum wells in the active region. The thickness can be optimized by simulating devices with varying thicknesses and comparing their performances. Thus, simulation tools help to optimally design the device structure and critically analyze the performance.

In this thesis, we have used advanced physical models of semiconductor devices (APSYS), from Crosslight software for device modeling. APSYS is a 2D/3D modeling software based on finite element analysis (FEA). This software deals with advanced physical models, e.g., heterojunction models, thermal analysis models, and hot carrier transport models. Although band structure engineering and quantum mechanical model is at the core of the software, by simulating the device structure we can achieve various useful information relevant for the device operation, such as the current-voltage (I-V) characteristics of the device, energy band diagram at different bias levels, wave functions, carrier concentration, and potential distribution etc. Various optical modules are included in the software so that optical properties can also be analyzed.

The software works on three input files, namely, the layer file, the solution file, and the plot file. The device structure is specified in the layer file. It includes structure dimensions, doping, and alloy compositions. The material properties, bias conditions, any

other specific parameters can be defined in the solution file. This is the main simulation input for APSYS and it consolidates all the models and runs the appropriate physical models to simulate the structure. Device parameters, such as, mobility, carrier lifetime, recombination coefficients can also be specified in the simulation according to the requirements. Then the plot file is used to plot all the information needed by the user. Fig. 2.7 shows the flow chart of this process.

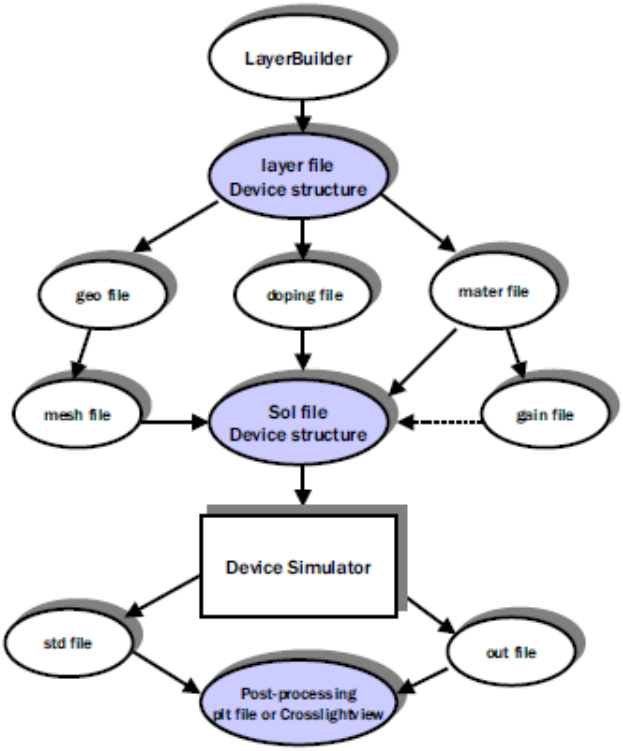

Figure 2.7 Flow chart of APSYS device simulation.

APSYS has been widely used to simulate III-Nitride material device characteristics. It can successfully incorporate the special properties of III-nitride materials, such as, wurtzite structure, spontaneous and piezoelectric polarization effect, and effect of metal and N-polarity on the devices. Apart from these, the software provides special tools to study the surface state effects. Since this research work is based on nanowire LEDs and nanowires suffer the most from the surface state effects, this tool is intensely utilized to study the surface state effects of the nanowire LEDs in this work.

Chapter 3. High Performance Phosphor-Free Nanowire White LEDs

Solid state lighting is a prime candidate for future lighting applications. As the demand for highly efficient phosphor-free white LED is increasing day-by-day, their operational properties, e.g., IQE and EQE and functional properties, e.g., CRI and CCT need to be carefully investigated. In this regard, phosphor-free white light emission based on III-nitride nanowire structures has been intensively studied and shown great promise for applications in solid state lighting [7, 10]. Compared to their conventional planar counterparts, III-nitride nanowires can exhibit greatly reduced dislocation densities, polarization fields, and QCSE due to the effective lateral stress relaxation [9-11, 170-173]. Excellent crystal quality achieved by nanowire structures can result in high IQE [174, 175]; however, the inefficient hole transport mechanism of nitride materials [176, 177] and the effect of surface states [178] result in low QE of nanowire LEDs. On the other hand, to have a good CRI and appropriate CCT, it is necessary to have the flexibility to tailor the SPD, and nanowire LEDs offer this flexibility to a great extent [110]. It will be demonstrated in this chapter that nanowire heterostructure LEDs can generate very high CRI values of 94 – 98 in both warm white and cool white regions.

Although the high surface-to-volume ratio of nanowires is advantageous for many applications, it also promotes non-radiative recombination and compromises the device performance because of having high density of surface states. It has been demonstrated that at room temperature under moderate current injection (100 $A \cdot cm^{-2}$), the SRH recombination accounts for up to 40% of the total recombination in typical axial nanowire LEDs [79]. This results in poor carrier injection efficiency, slow rising trend of QE, and low output power. As a consequence, the output power of nanowire LED is very low, often in the range of μW or even lower [179]. The effect of surface states can be mitigated by employing in-situ or ex-situ surface passivation schemes. For the ex-situ passivation process, the nanowire LEDs need to undergo external treatment, which often adversely affects their optical and electrical performance [180, 181]. In this chapter, we present the performance of InGaN/GaN nanowire LEDs which can be dramatically

improved by employing an in-situ deposited AlGaN surface passivation layer. Simulation results demonstrate that carrier injection efficiency improves significantly by reducing the surface recombination velocity. The experimental results clearly show a significant increase (by nearly two orders of magnitude) in the output power compared to the non-passivated nanowire LEDs.

3.1 Engineering the Functional Properties of Phosphor-Free Nanowire White LEDs

Solid state lighting offers several advantages over the conventional incandescent and fluorescent lamps; such as high efficiency, long lifetime, and reduced environmental impact. With the increasing demand of solid state lighting, it is imperative that they exhibit good CRI and appropriate CCT; which are two vital properties for any lighting applications. CRI is a measure to define how closely a light source can replicate the true color of an object. CCT defines the appearance of the light source. To engineer CRI and CCT values, the flexibility to tailor the SPD of the light source is required, which can be achieved by using solid state lighting. To date, the approaches for generating white light generally involve the use of yellow phosphor with blue or UV LEDs; red, green and blue phosphor with UV LEDs; and oxyfluoride or fluoride phosphor with violet LEDs [86, 182]. However, the functional properties of the emitted light depend on the phosphor compositions and the coating techniques, which are difficult to optimize without compromising the device efficiency. An alternative of using phosphor for down-conversion is to use semiconductor nano-crystals (NC). Monosized CdSe NCs or a combination of different-sized CdSe/ZnS NCs can generate white light with broad spectrum and good CRI values [183, 184]. However, the size variation of NCs causes reabsorption due to Forster type energy transfer and lowers the efficiency of the devices [185]. In this context, nanowire LEDs can offer significantly improved performance. Multicolor emission has been achieved by using various nanostructures including InGaN/GaN well/disk-in-a-wire and core-multi-shell structures [174, 186-188]. All semiconductor-based white LEDs have also been demonstrated by using InGaN ternary nanowires [12], InGaN/GaN nano-disks [107], etched InGaN quantum wells [189] and recently, the InGaN/GaN dot-in-a-wire structures [79, 110, 190].

In this section, we study the functional properties of white light generated by InGaN/(Al)GaN dot-in-a-wire LEDs grown by MBE. Additionally, the incorporation of quantum dots in the nanowire LED active regions may effectively provide superior carrier confinement, promising high efficiency LEDs with tunable emission. On the other hand, in our nanowire LEDs, the emission spectra and SPDs of nanowire white LEDs can be readily adjusted by varying the growth parameters at the wafer-level. The novelty of this approach is the simplicity in tailoring the spectrum to achieve desirable CRI and CCT values. We have presented here that, our phosphor-free InGaN/(Al)GaN nanowire LEDs can have CRI>90 in both warm and cool white regions, which are the highest values ever reported for phosphor-free white LEDs.

3.1.1 Growth of Nanowire White LEDs

The schematic diagram of InGaN/(Al)GaN nanowire white LEDs is presented in Fig. 3.1(a). The dot-in-a-wire LED heterostructures were grown by RF PAMBE on *n*-Si substrate. The growth temperature for GaN nanowires was ~750 °C. The plasma forward power and nitrogen flow rate were kept at 350 W and 1 standard cubic centimeter per minute (sccm) during the growth. The active region of the LED device includes ten InGaN/(Al)GaN dots. Each dot consists of ~3 nm InGaN. The active region is then capped by a *p*-doped AlGaN EBL to prevent electron overflow [109] and followed by a *p*-GaN layer. The peak emission and SPD of the white light emission can be controlled by adjusting the In composition in the quantum dot active region which can be achieved by varying the growth conditions including the substrate temperature and/or In/Ga flux ratio. The In composition varies from ~10% to 50% along the growth direction, resulting in a wide spectrum having different color components [110, 190, 191] and stable and robust white light emission due to the large inhomogeneous broadening.

Figure 3.1(b) shows the SEM image of a typical nanowire white LED sample. The nanowires are vertically aligned and uniformly distributed on Si substrate. The density of the nanowires is estimated to be ~ 10^{10} cm^{-2}. Figure 3.1(c) presents the normalized PL spectra of two nanowire LEDs. The PL spectra were measured using a 405 nm laser at room temperature. The two nanowire LEDs were grown at two different conditions to engineer the peak wavelength and the SPD. The substrate temperature was varied from ~

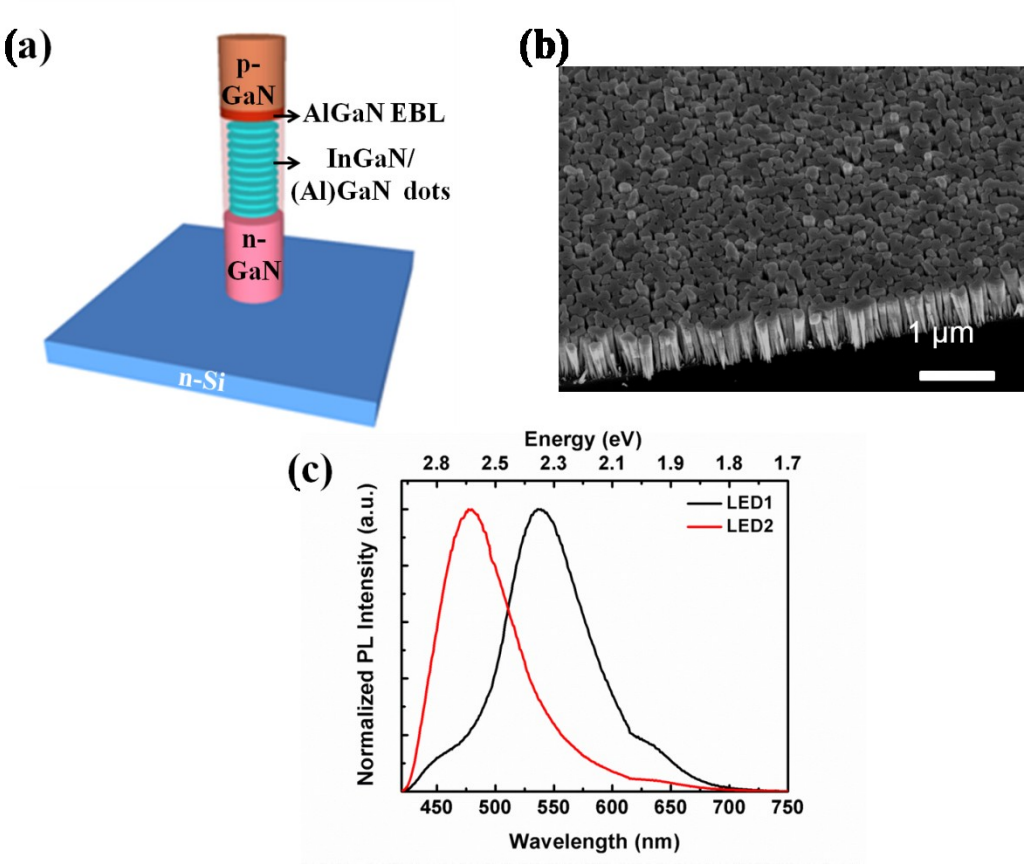

Figure 3.1 (a) Schematic structure of the InGaN/(Al)GaN nanowire LED; (b) SEM image of the nanowire LEDs grown on *n*-Si substrate; (c) Normalized PL spectra of LED1 and LED2.

600 °C to 680 °C to modulate the In compositions in the active regions of these LEDs resulting in the differences in peak emission wavelengths and SPDs. Shown in Fig. 3.1(c), the peak wavelengths of LED1 and LED2 are varied in the range of ~480 to 550 nm. LED1 and LED2 both have wide SPD with different spectral contents indicating that they will demonstrate different CRI and CCT values.

3.1.2 Results and Discussions

The nanowires are fabricated using the standard white LED fabrication technique as described in Section 2.2.1. In our study, the dot-in-a-wire structures can offer a wide range of CCT values by changing the growth parameters, whereas keeping a high CRI value. Both CRI and CCT depend on the SPD of the emitting light source. However, it has been challenging to achieve high CRI (>90) in the cool or neutral white region

because high CRI requires that the SPD should incorporate the long wavelength components of visible spectra whereas cool/neutral CCT requires short wavelength components in the SPD. The normalized EL spectra of the two LED devices are presented in Fig. 3.2 (a). LED1 and LED2 both have broad spectra with FWHM of 186 nm and 169 nm, respectively. The multiple emission peaks are directly related to the compositional variations of the quantum dots in the LED active region. LED1 and LED2 have SPD in the range of 400 - 800 nm, and 380 - 760 nm, respectively. Due to the wider spectrum, LED1 demonstrates a higher CRI value compared to LED2. The measured CRI values for LED1 and LED2 are 97.7 and 95.6, respectively. LED1 has a CCT of 2357 K (warm white) and the Commission Internationale d'Eclairage (CIE) 1931 coordinates of

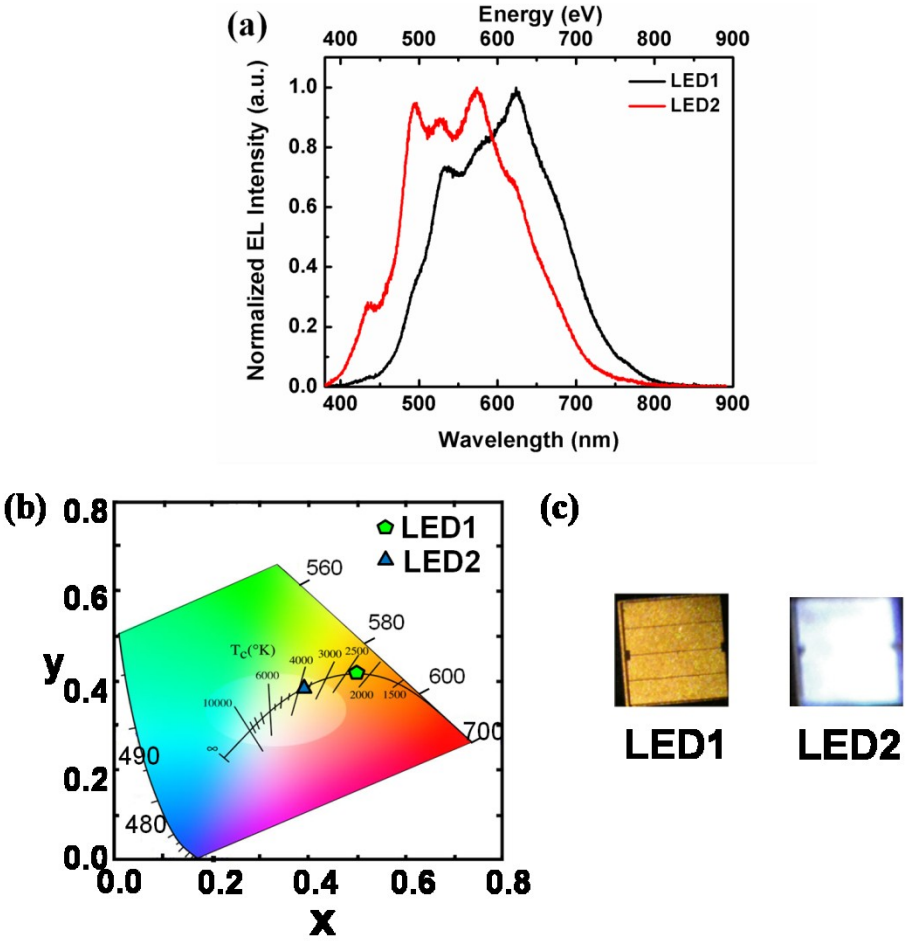

Figure 3.2 (a) Normalized EL spectra of LED1 and LED2 measured at room temperature; (b) The CIE coordinates of LED1 and LED2; (c) The optical images of the emitted light of LED1 and LED2.

(0.50, 0.42). The SPD of LED2 incorporates short wavelength components, thus emitting neutral white light (CCT ~ 3838 K), which is suitable for indoor lighting applications. It also demonstrates a high CRI value of 95.6, and the CIE 1931 coordinates of (0.39, 0.38). The CIE coordinates of LED1 and LED2 and the optical images of strong light emitted by LED1 and LED2 are shown in Figs. 3.2(b) and 3.2(c), respectively. Moreover, cool white light emission with relatively high CRI values can also be achieved by varying the InGaN quantum dot compositions.

Figure 3.3 shows the current dependent EL spectra of 0.3 × 0.3 mm^2 devices measured under pulsed biasing conditions (5% duty cycle) at room temperature. The CRI, CCT and CIE coordinates do not show significant variations with current, confirming stable operation. Shown in Table 3.1, in the current injection range of 40 to 70 mA, LED1 shows relatively stable CRI values (96.2 - 97.7) and CCT (2357 K -2589 K), and nearly constant chromaticity coordinates (x ≈ 0.48 - 0.50 and y ≈ 0.42 - 0.43). LED2 has slightly lower CRI values, which is in the range of ~94.2 - 95.6, compared to LED1. The CCT of LED2 varies from 3838 K to 4035 K, with nearly stable chromaticity coordinates (x ≈ 0.38 - 0.39 and y ≈ 0.38 - 0.39). Additionally, peak positions of the EL spectra from these

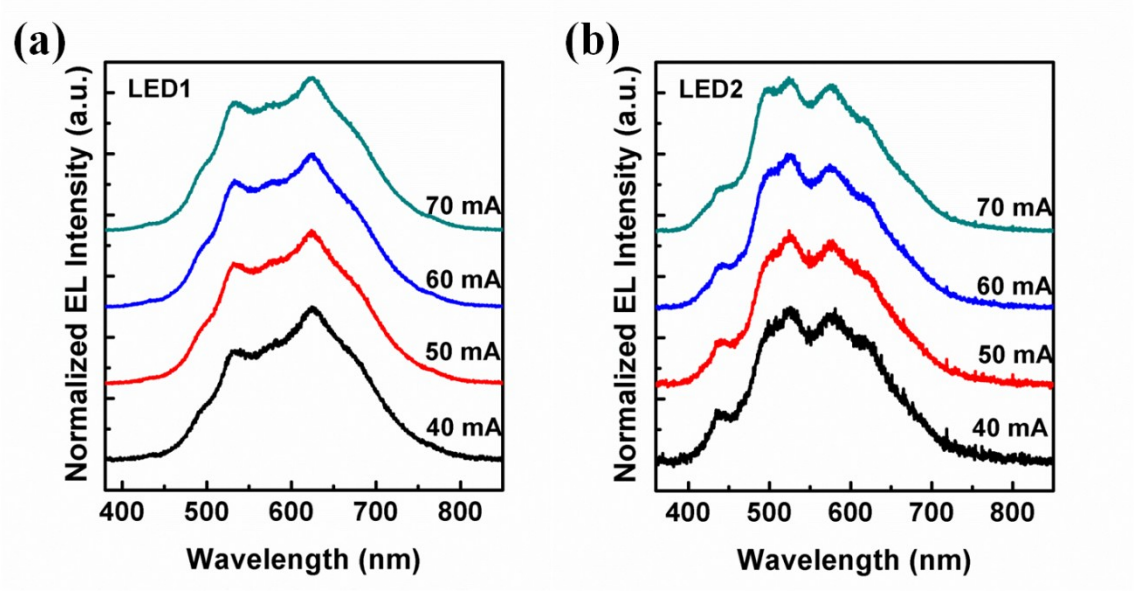

Figure 3.3 EL spectra under different injection currents for (a) LED1 and (b) LED2. The measurement was carried out under pulsed biasing condition with 5% duty cycle at room temperature.

LEDs are stable with increasing current. This demonstrates that the effect of QCSE is less significant in nanowire LEDs due to the effective strain relaxation through lateral surfaces. The highly stable emission is also directly related to the large inhomogeneous broadening of the dot-in-a-wire structures.

In summary, we have developed phosphor-free InGaN/(Al)GaN dot-in-a-wire nanoscale LEDs which can emit white light in the warm and cool white regions. The nanowire LED spectrum can be tuned readily to achieve excellent characteristics. Our LEDs demonstrate stable and unprecedentedly high CRI values with CIE coordinates in the warm and cool white regions of the chromaticity diagram.

Table 3.1 The CRI, CCT, and CIE coordinate values at different injection currents under pulsed biasing condition (5% duty cycle) for 0.3×0.3 mm^2 devices of LED1 and LED2.

Device	Current (mA)	CRI	CCT (K)	CIE Coordinates (x, y)
LED1	40	97.7	2357	(0.50, 0.42)
	50	96.2	2461	(0.49, 0.43)
	60	97.1	2494	(0.49, 0.43)
	70	96.7	2589	(0.48, 0.43)
LED2	40	95.6	3838	(0.39, 0.38)
	50	95.5	3841	(0.39, 0.39)
	60	94.7	3940	(0.39, 0.39)
	70	94.2	4035	(0.38, 0.39)

3.2 Improving the Carrier Injection Efficiency of Phosphor-Free Nanowire White LEDs

III-nitride nanowire structures are emerging as a promising candidate for optoelectronic devices. Both axial and radial InGaN/GaN heterostructures have been intensely studied [12, 105, 107, 110, 192-197]. In InGaN/GaN core-shell radial heterostructure, the InGaN MQWs are grown radially on the side facets of GaN nanowire. The non-polar side facets offer the advantages of reduced polarization field and increased surface emission area. However, the core-shell radial InGaN/GaN nanowires are often grown by MOVPE and due to the structural inhomogeneity and difficulty in incorporating high In content for green and red emission, it is very difficult to achieve high efficiency white core-shell LEDs. Furthermore, due to the non-planar fabrication technique associated with radial structure, it is challenging to fabricate large area devices with good ohmic contact and homogeneous current spreading. In this context, the axial InGaN/GaN nanowire heterostructures grown by catalyst-free PAMBE shows great promise. Color tunable emission of such nanowire heterostructures have been demonstrated in a wide wavelength range. The fabrication process of such nanowire arrays grown on Si substrate is also similar to that of commercial planar LEDs. However, axial nanowires suffer severely from the presence of surface states and defects, which often lead to unacceptably large non-radiative surface recombination. It can further deplete mobile carriers and significantly increase the device resistance. The enhanced non-radiative recombination results in poor carrier injection efficiency, small QE and low output power. The surface recombination velocity of GaN is ~10^4 cm/s [198, 199]. However, due to the strain and defects induced in InGaN/GaN nanowire LEDs, much higher surface recombination velocity is expected. Therefore, the surface recombination is more severe in InGaN LEDs with high In content, especially in the green and red wavelength regions.

In this section, we have investigated the effect of surface recombination on the carrier injection efficiency of InGaN/GaN nanowire LEDs. We present that the carrier injection efficiency can be improved to a great extent by reducing the surface recombination velocity, i.e., by designing the core shell structure. We have presented that the core-shell structure can outperform the non-core-shell structure by demonstrating an output power

as high as 1.5 mW, which is nearly two orders of magnitude higher than the non-core-shell structure [191].

3.2.1 Simulation Model

We have modeled the effect of surface states on nanowire LEDs by using APSYS, Crosslight [200]. We have used the 'interface' model to simulate the surface state effects. The 'interface' model specifies the semiconductor interface, which could be between semiconductor and vacuum, between semiconductor and air, or between different semiconductors. Three different kinds of models are used with this 'interface' statement to describe the physics of interface: (i) 'recomb': this model defines the surface recombination velocity, i.e. the rate of recombination between electrons and holes at the surface of the semiconductor. A zero surface recombination velocity indicates that the surface is free of any defects whereas the surface severely plagued with surface states has a high surface recombination velocity. (ii) 'trap': this parameter defines the surface traps, which could be either donor or acceptor type traps. They are quantified by 'trap density' and 'trap level'. 'trap density' is a measure of how badly the surface is affected by defects and dislocations whereas 'trap level' is the associated defect energy level measured from the conduction band edge. (iii) 'charge': this parameter defines fixed interface charge density, which could be either positive or negative. The model 'recomb' is used to simulate the effect of non-radiative recombination at the surface, whereas 'trap' and 'charge' models are used to simulate the band bending due to the Fermi level pinning at the surface and the carrier depletion from the surface, respectively. Our simulation is based on the 'recomb' model.

Our dot-in-a-wire LEDs consist of InGaN active regions followed by GaN barriers. We are more interested in analyzing the effects of the surface states on the effective carrier concentration, on injection efficiency, and on radiative recombination rate. With this view in mind, we have developed a simple LED model consisting of only one 3 nm $In_{0.25}Ga_{0.75}N$ quantum well, followed by GaN barrier layers. The schematics of planar and nanowire structures that we have used in our simulation are presented in Fig. 3.4. The carriers are generated by optical pumping. The wavelength of the optical pump was set at 405 nm. The SRH lifetime related to bulk recombination, the Auger recombination

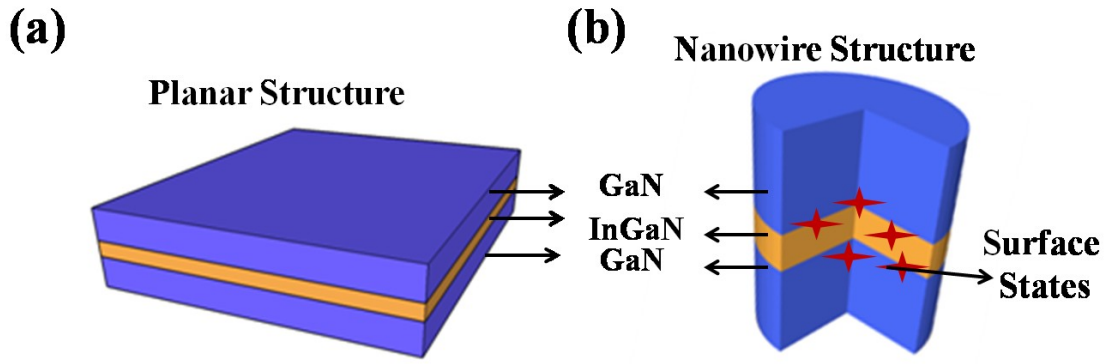

Figure 3.4 Schematic diagrams of the structures used in the simulation; (a) planar, and (b) nanowire.

coefficient, and the carrier generation rate for the planar structure are set to 100 ns, 1×10^{-33} $cm^6\cdot s^{-1}$, and 2.5×10^{27} $cm^{-3}\cdot s^{-1}$, respectively.

3.2.2 Effects of Surface States on Carrier Injection Efficiency of Nanowire LEDs

The planar structure is considered to be free of any surface states (i.e. zero surface recombination velocity) and all the carriers remain confined in the active regions. However, the carrier generation in nanowire is severely affected by the presence of surface states and defects. Figure 3.5 presents the carrier concentration for a planar structure and a nanowire of diameter 100 nm. The surface recombination velocity is set to 5×10^4 cm/s for the nanowire LED. As apparent from the figure, the nanowire LED exhibits much lower carrier density compared to the planar structure for the same level of carrier injection. Furthermore, the carrier distribution is not uniform along the diameter of the nanowire. Higher concentration is observed at the central core region, which signifies the presence of non-radiative recombination at the surface. To study the dependence of carrier concentration on surface recombination velocity and diameter, we define carrier injection efficiency (η_e) as the ratio of the effective carrier density in the nanowire structure (N_{eff}) to the injected carrier density (N_{inj}), which is the equivalent carrier density for the planar structure.

$$\eta_e = N_{eff}/N_{inj} \tag{3.1}$$

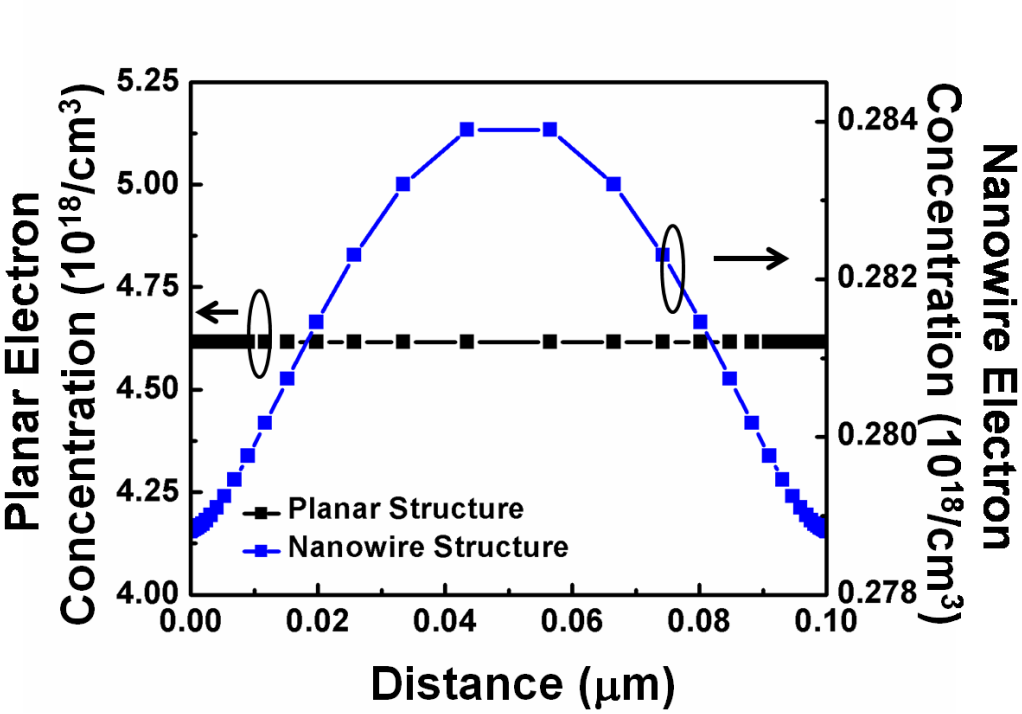

Figure 3.5 Comparison of carrier concentration of a planar and a nanowire structure under identical carrier excitation conditions. The carrier generation rate in the active region is set to 2.5×10^{27} cm^{-3}·s^{-1}.

In our simulation, we calculated carrier injection efficiency as a function of surface recombination velocity for nanowires with different diameters. Surface recombination velocity is directly related to the density of surface states. The variation of η_e with respect to surface recombination velocity for different diameters is presented in Fig. 3.6. It is apparent from the figure that η_e increases with increasing diameter. However, as the diameter increases, the benefits associated with high surface-to-volume ratio, such as lateral stress relaxation and large light extraction efficiency are compromised. This is an important design issue to achieve high power LED devices and should be considered very carefully. It is seen from Fig. 3.6 that for a fixed diameter nanowire LED, η_e decreases significantly with the increase of surface recombination velocity. For a nanowire with 100 nm diameter, η_e decreases from 24% to 6% for a surface recombination velocity increase from 5×10^3 cm/s to 5×10^4 cm/s. This large reduction calls for some effective method to passivate the surface of nanowires. In this regard, we have developed the unique dot-in-a-wire core-shell LED structures [191] which can effectively reduce the

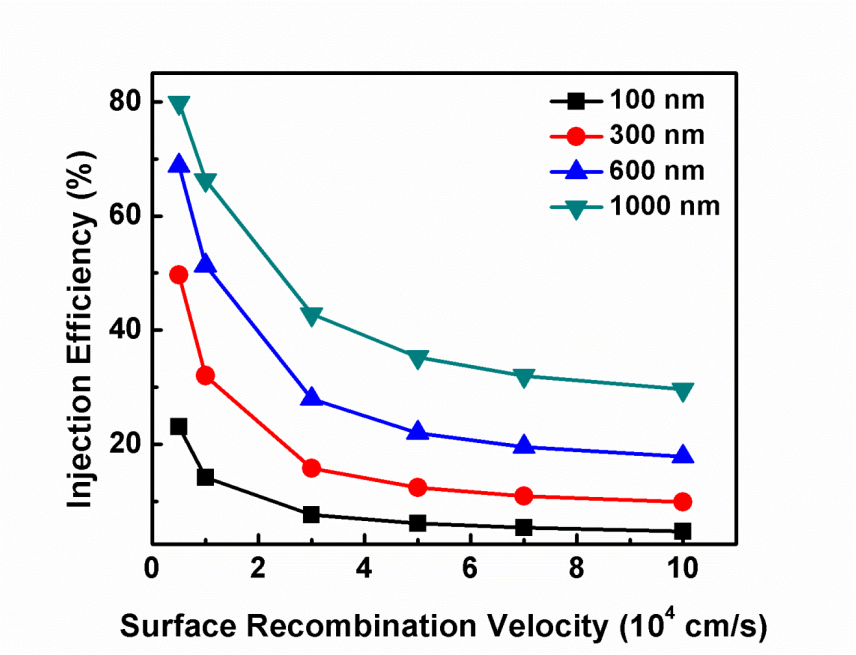

Figure 3.6 Variation of carrier injection efficiency as a function of surface recombination velocity and nanowire diameter [191]. The carrier generation rate in the active region is set to 2.5×10^{27} $cm^{-3} \cdot s^{-1}$.

surface recombination velocity resulting in an enhanced device performance. For surface passivation, the nanowire structure is surrounded by AlGaN shell. The presence of high bandgap material at the surface of the core nanowire prevents the carriers to escape from the active region and thus enhances the carrier injection efficiency. The high angle annular dark field (HAADF) image is presented in Fig. 3.7(a) [191]. The figure clearly shows the formation of the shell surrounding the nanowire surface. The energy dispersive X-ray (EDX) elemental mapping is presented in Fig. 3.7(b) [191], showing the presence of the InGaN/GaN active region and the AlGaN shell.

To prove that the core-shell dot-in-a-wire structure enhances the LED performance, we have performed the PL measurement on the core-shell and non-core-shell structure under the same optical excitation conditions (exciting laser: 405 nm; excitation power: 20 mW). Figure 3.8 presents the PL spectra of these LEDs and we observe that the PL intensity for the core-shell LED is ~6-7 times stronger than the non-core-shell LED. This enhancement clearly indicates that the shell can provide better lateral confinement by preventing the carriers leaking out of the active region. This core-shell LED exhibits an output power as high as ~1.5 mW at room temperature, which is more than 2 orders of

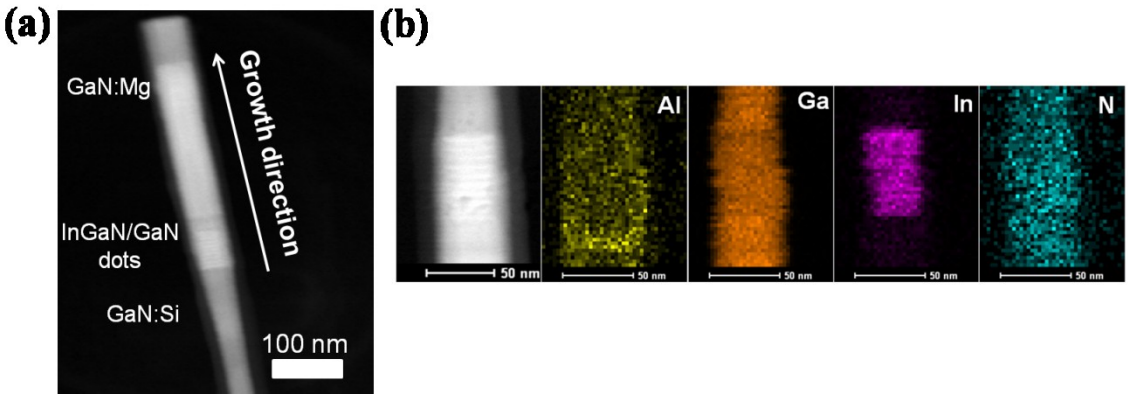

Figure 3.7 (a) HAADF image, and (b) EDX elemental mapping of the active region of InGaN/GaN nanowire heterostructure [191].

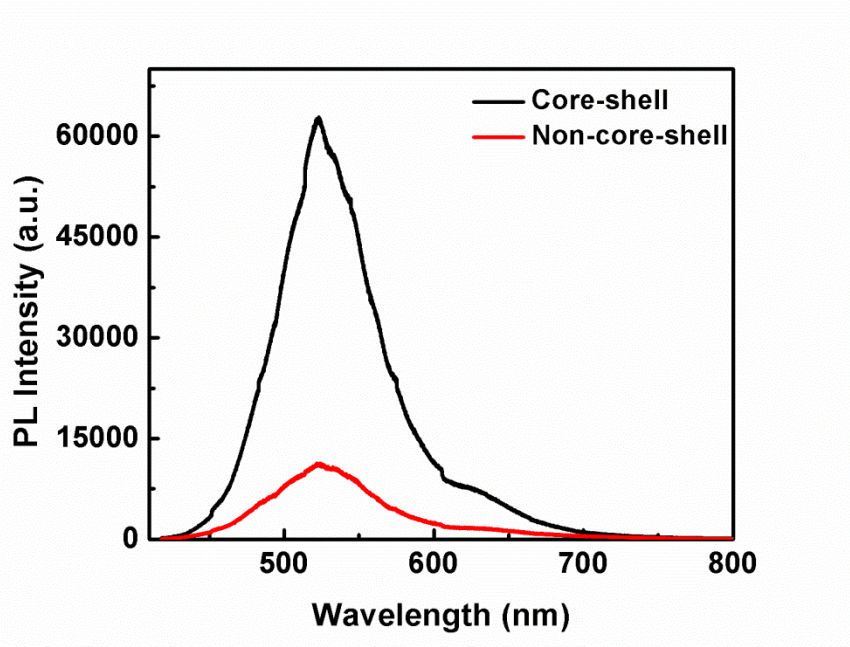

Figure 3.8 Comparison of the PL intensity of core-shell and non-core-shell nanowire LEDs.

magnitude stronger than the non-core-shell LED structure [191].

In this section, we have demonstrated that the non-radiative surface recombination is one of the bottlenecks for achieving high efficiency nanowire LEDs. We show that carrier injection efficiency of a 100 nm diameter nanowire can be as low as 6%, compared to the near-unity carrier injection efficiency of planar LED structures. In addition to surface recombination velocity and nanowire diameter, the carrier injection of nanowire LEDs can also be varied by the surface band bending. The band bending depends on the doping and diameters of nanowires and may result in the depletion or accumulation of charge carriers in the near surface region. As the carriers (electron/hole) are injected in the device active region, they may be spatially separated, to a certain extent, by the lateral electric field of nanowires associated with the surface band bending, which can reduce non-radiative surface recombination. Therefore, the carrier injection efficiency can be further improved by optimizing the surface band structure through controlled dopant incorporation [201]. However, doping of the nanowire may introduce defects and traps, which contributes to enhanced non-radiative recombination, which should be carefully considered in designing the core-shell nanowire LED structures.

Chapter 4. Characterization of AlN Nanowires

The characteristics of both non-doped and Mg-doped AlN nanowires have been studied in this chapter. As mentioned in Chapter 1, both the growth and characterization of AlN has been very challenging. It is very difficult to grow good quality AlN due to the lack of lattice matched substrate, the difference in growth kinetics of Al and Ga, and the difficulties in achieving efficient doping [13, 14]. In comparison to planar structures, AlN nanowires can offer significantly improved properties since the densities of defects and dislocations can be drastically reduced in nanowire structures [53]. Furthermore, due to the reduced formation energy of substitutional doping in the near surface region of the nanowires, nanowire structures offer enhanced surface doping and conductivity [202]. In this chapter, the optical properties of non-doped and Mg-doped AlN nanowires have been analyzed in detail. The non-doped AlN nanowires clearly exhibit strong free exciton emission at 20 K and at room temperature. The enhanced optical performance of the AlN nanowires confirms its superior quality over AlN epilayer. The AlN:Mg nanowires present the band-edge emission peak and also, the Mg-acceptor related peak. Detailed temperature dependent electrical measurements on the AlN:Mg nanowires reveal that the hopping conduction is the dominating carrier transport mechanism at room temperature. From these measurements, the free hole concentration is estimated to be ~10^{16} cm^{-3}, or higher at room temperature.

4.1 Optical Properties of Strain-Free Non-doped AlN Nanowires

In this section, the optical properties of the non-doped AlN nanowires are thoroughly investigated. The advantages of nanowire structures can be seen in the enhanced performance of the nanowires, such as stronger optical emission at room temperature compared to its planar counterpart. The peak position of the emission spectra further confirms the strain-free nature of the AlN nanowires. The presence of optical phonon replicas are also observed, which are designated as the surface optical (SO) phonon modes, rather than the commonly observed longitudinal optical (LO) phonon replicas in AlN epilayer.

4.1.1 Growth and Structural Characterization

The AlN nanowires were grown on Si substrate by catalyst-free PAMBE. To promote the formation of AlN nanowires, a GaN template was grown on Si substrate first. For the GaN nanowire growth, initially a thin Ga seeding layer of 0.6 nm was deposited on Si substrate before introducing nitrogen. The schematic diagram of the AlN nanowire on GaN template is presented in Fig. 4.1(a). The growth condition of GaN nanowires is the same as described in section 3.1.1. However, higher temperature is required for AlN growth to provide enough mobility to Al adatoms [203]. The substrate temperature is increased to ~858 °C for AlN nanowire growth and the Al flux ratio is kept at 6×10^{-8} Torr. The nitrogen flow rate and the forward plasma power were kept the same as described in Section 3.1.1. Fig. 4.1(b) presents the SEM image of the AlN nanowires. The nanowires are vertically aligned and uniformly distributed on the Si substrate. The diameter of the AlN nanowires is estimated to be 100 nm and the density is 10^{10} cm^{-2}. A high resolution TEM image is presented in Fig. 4.1(c). The crystalline planes are clearly observed in the TEM image and also the absence of misfit dislocations and stacking fault is confirmed. A 0.25 nm interplanar spacing is determined indicating that the growth direction is along the *c*-axis [204-206].

4.1.2 Optical Characteristics

The optical characteristics of the AlN nanowires have been carefully studied. For the PL measurements, a 197 nm frequency quadrupled Ti-sapphire laser was used as the excitation source. The low temperature (10 K) PL spectra of the AlN nanowire and AlN epilayer are presented in Fig. 4.2. The growth condition of the AlN epilayer is described elsewhere [136, 207]. The thickness of the AlN epilayer is 1 μm, which is comparable to the height of the AlN nanowires. Furthermore, the diameters of AlN nanowires are in the range of 100 nm and for such large diameters, quantum confinement effect can be neglected. These factors enable the direct comparison of excitonic transitions of AlN nanowires and epilayer. Three distinct peaks are observed in the low temperature PL spectra of both AlN nanowire and epilayer. For AlN nanowires, the peaks are at 6.03 eV (205.6 nm), at 5.93 eV (209.1 nm), and at 5.83 eV (212.7 nm). The first peak is

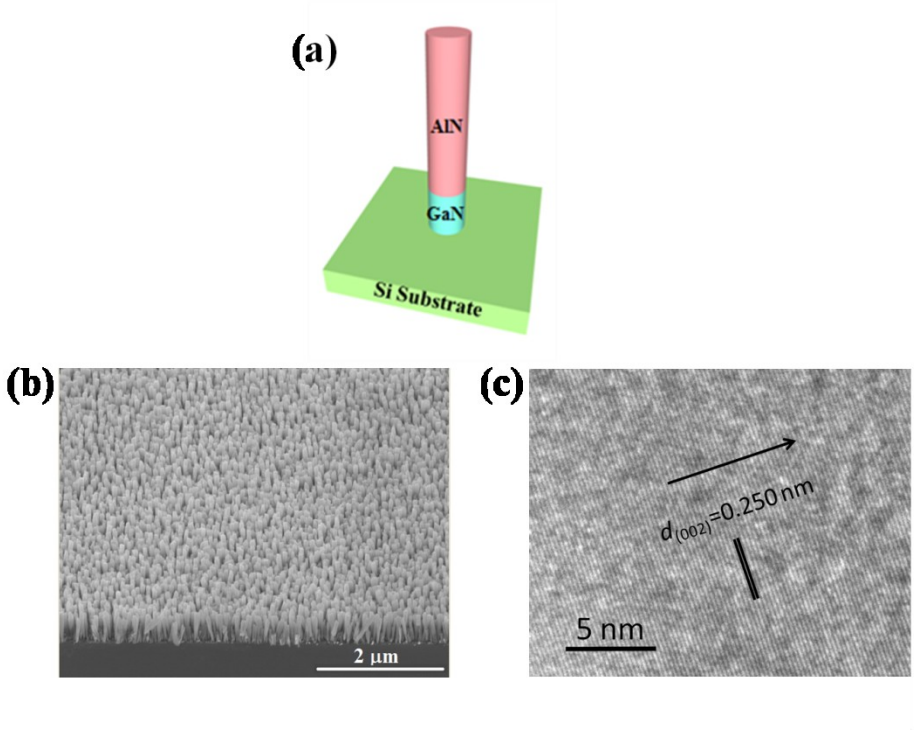

Figure 4.1 (a) Schematic diagram of the AlN nanowires grown on GaN template on Si substrate. (b) The SEM image of the AlN nanowires taken with a 45° angle. (c) TEM image of a single AlN nanowire (10 nm above the GaN template). The arrow indicates the growth direction.

designated as the free exciton (FX) emission ($n = 0$ line), and the other two peaks are the two phonon replicas. For AlN epilayer, the FX transition is observed at 6.06 eV, and the phonon replicas are at 5.95 eV and at 5.84 eV, which is similar to the previous report of AlN epilayers grown on sapphire substrate [208]. To analyze the difference of peak emission wavelengths of AlN nanowires and epilayer, it is of interest here to present the comparative study of the peak emission and the quality of AlN epilayers grown on different substrates [209]. AlN epilayer grown on sapphire substrate experiences a compressive strain and the peak emission has a blue shift compared to the strain free case. The AlN epilayers grown on the AlN substrate experience no lattice mismatch and therefore, are almost strain free. The FX emission of the AlN homoepilayer has been reported at 6.03 eV [209], which is similar to the FX transition observed in AlN nanowires. This confirms that the nanowires are virtually strain-free and of supreme crystalline quality. Furthermore, the FWHM of the FX emission of AlN nanowires is 21 meV whereas that for AlN epilayer is 33 meV. The narrower FWHM is another

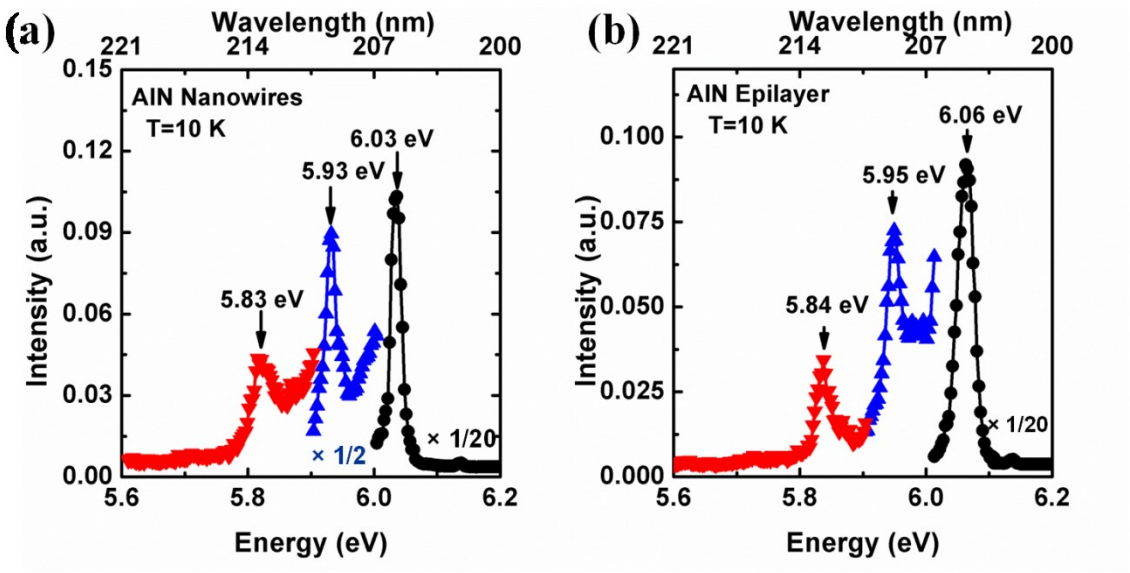

Figure 4.2 The low temperature (10 K) PL spectrum of (a) AlN nanowires, and (b) AlN epilayer.

indication that the AlN nanowire has better crystalline quality compared to the AlN epilayer.

The supreme crystalline quality is further evidenced from the room temperature PL spectrum of AlN nanowires. Figure 4.3 presents the room temperature PL spectra of both AlN nanowires and AlN epilayer. AlN nanowires have FX emission peak at 5.96 eV, which is stronger than the FX emission peak of AlN epilayer at 5.99 eV. This superior optical emission not only indicates the enhanced crystalline quality of AlN nanowires but also suggests the reduced surface state effects on the excitonic transition of AlN nanowires. The carriers in AlN have a large effective mass, and hence, a small Bohr radius (~ 1.2 nm) and large binding energy (~ 60 meV). Therefore, the recombination process is dominated by the excitons even at room temperature and the carrier non-radiative recombination via surface states/defects is greatly minimized.

Apart from the free excitonic transition, the presence of two phonon replicas is observed in the low temperature PL spectrum of AlN, as presented in Fig. 4.2. The energy separation between the phonon replicas of AlN nanowires is 100 meV, whereas that for AlN epilayer is 110 meV. The phonon replicas have been identified as LO phonon replicas for AlN epilayers [208]. However, the large difference in the separation energy (10 meV) of the phonon replicas of AlN epilayer and nanowire calls for more

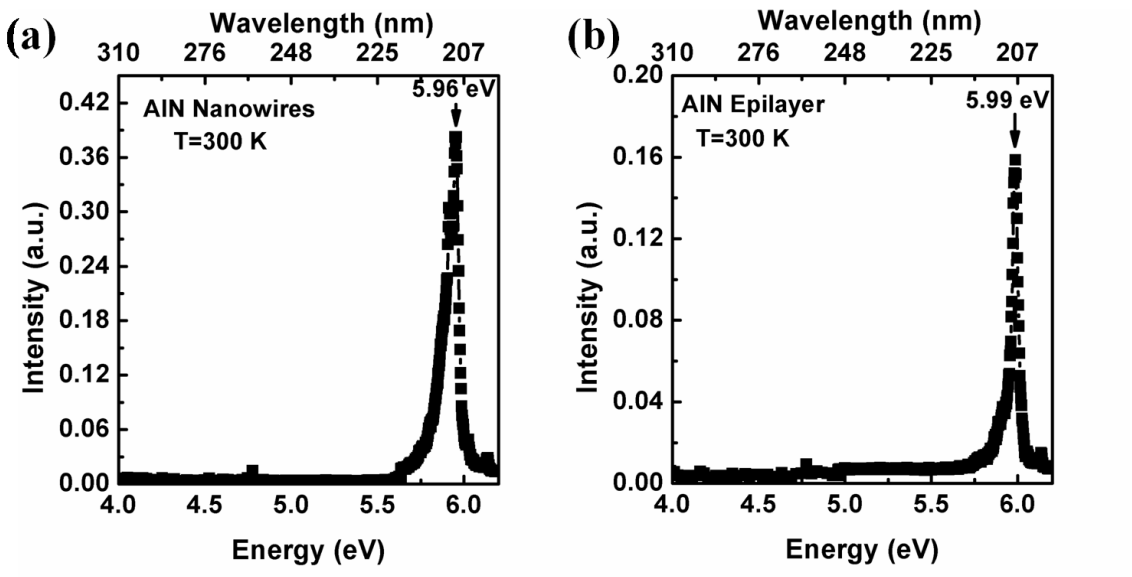

Figure 4.3 Room temperature PL spectra of (a) AlN nanowires, and (b) AlN epilayer.

investigation. The SO phonon mode, which arises from the abrupt termination of the crystal structure at the surface, can be a suitable candidate for the observed phonon replicas in AlN nanowires. Such SO phonon modes have been observed in nanowire structures [210-216] and vary with the morphology, density, size of the nanowires, and the dielectric constant of the environment [214]. Based on Loudon's uniaxial crystal model and within the framework of the dielectric continuum model, the estimated SO phonon energy in AlN nanowires can be varied from 84 meV to 110 meV [216]. Hence, the phonon replicas observed in AlN nanowires are most likely due to the interaction between SO phonons and electrons via Frohlich electron-phonon coupling. This has been also confirmed by Raman spectroscopy measurement, as presented in [217].

4.2 On the Magnesium Doping into AlN Nanowires

In this section, the optical and electrical properties of Mg-doped AlN nanowires have been discussed. At room temperature, with the increase of Mg-doping concentration, the Mg acceptor energy level related transition appears in PL spectra indicating an enhanced Mg incorporation. The electrical conduction on the other hand indicates an activation energy of 23 meV in the 300 K – 450 K temperature range, which is significantly smaller than the Mg ionization energy (~600 meV) in AlN [146], suggesting the *p*-type conduction being mostly related to hopping mechanism and/or impurity band conduction

[218, 219]. Meanwhile, the electrical measurements at higher temperature range present the possibility of different activation energy at elevated temperatures. The increase of activation energy with temperature indicates the involvement of the thermal activation process, and at a sufficiently higher temperature, thermally activated carriers should dominate the transport mechanism. The detailed optical transitions related to different energy levels are also discussed in the text.

4.2.1 Optical Characterization

The growth conditions of the AlN nanowires are the same as described in Section 4.1.1. To study the effect of Mg-doping, a series of AlN:Mg nanowire samples were grown and studied, listed in Table 4.1. Samples A, B, and C were grown with an Al flux of 4.0×10^{-8} Torr, and Mg flux of 2.6×10^{-9} Torr, 1.6×10^{-8} Torr, and 9.1×10^{-8} Torr, respectively. Samples D and E were grown with Al flux of 2.0×10^{-8} Torr, and Mg flux of 2.6×10^{-9} Torr and 9.1×10^{-8} Torr, respectively. The axial growth rate is ~ 3.5 nm/ min for samples A, B and C, and 1.5 nm/ min for samples D and E.

Temperature variable PL measurements were performed on as grown Mg-doped AlN nanowires using a 193 nm ArF exciton laser as the excitation source. Figure 4.4(a) presents the PL spectra of the AlN:Mg nanowires at 20 K. We observe a narrow peak at 205 nm (6.05 eV), and a broad peak at 227.4 nm (5.45 eV) for samples C, D, and E. We designate the first peak as the high energy peak, P_H and the second broad peak as the low energy peak, P_L. P_H is due to the excitons bound to neutral Mg-acceptor impurities (I_1 line in AlN). The energy separation between P_H and P_L is about 0.6 eV, which is consistent with the Mg-activation energy in AlN [147]. Various defect related transitions have been identified for planar AlN [130, 220, 221]. These defect emissions are mainly due to the nitrogen/cation vacancies and related complexes in AlN. In previously reported AlN:Mg epilayers, the optical transition involving the deep level donor and Mg-acceptor is observed at 4.7 eV and the transition involving shallow donor and deep acceptor is observed at 3.9 eV [146]. These facts rule out the possibility of the low energy peak at 227.4 nm (5.45 eV) to be a defect peak and, therefore, PL can be attributed to the DAP transition between a shallow donor and Mg-acceptor energy level [146, 147]. The ionization energy of the shallow donor can be derived from the temperature dependent

Table 4.1: Growth parameters for Mg-doped AlN samples having different growth rates and different doping levels.

Samples	Al-Flux (Torr)	Mg-Flux (Torr)
A	4.0×10^{-8}	2.6×10^{-9}
B	4.0×10^{-8}	1.6×10^{-8}
C	4.0×10^{-8}	9.1×10^{-8}
D	2.0×10^{-8}	2.6×10^{-9}
E	2.0×10^{-8}	9.1×10^{-8}

PL intensity (discussed later) and deduced to be ~80 meV for AlN:Mg nanowires, which is in reasonable agreement with the previous reported values (~60 meV) for AlN epilayer [146]. The ionization energy of the Mg-acceptor can be deduced as, $E_0 = E_g - 5.45 - 0.08 = 0.61\ eV$, where $E_g = 6.14\ eV$ is the band gap of AlN at 20 K. This Mg-acceptor related peak increases with Mg-dopant incorporation. Moreover, it is more pronounced for samples D and E, grown with reduced growth rate (low Al flux), indicating that a slower growth rate significantly enhances Mg-incorporation. This observation is further supported by the comparison between samples A (high Al flux) and D (low Al flux), which were both grown with the same Mg flux of 2.6×10^{-9} Torr. It is seen that no Mg-acceptor related transition can be observed for sample A, whereas such a transition can be clearly measured in sample D. The direct correlation between the emission peak at 227.4 nm with Mg-dopant incorporation provides unambiguous evidence for the presence of Mg-acceptors in AlN. The strong dependence of Mg-dopant concentration on variations of the growth conditions is a result of several competitive processes, including the enhanced Mg-acceptor incorporation due to the reduced formation energy for the Al-substitutional Mg-doping in the near-surface region of nanowires as well as the Mg atom desorption at elevated growth temperature [222, 223].

The power and temperature dependent PL studies were performed. In what follows, we focus on the highly Mg-doped AlN sample with reduced growth rate (sample E). The power dependent PL properties at 20 K are shown in Fig. 4.4(b). The inset of Fig. 4.4(b)

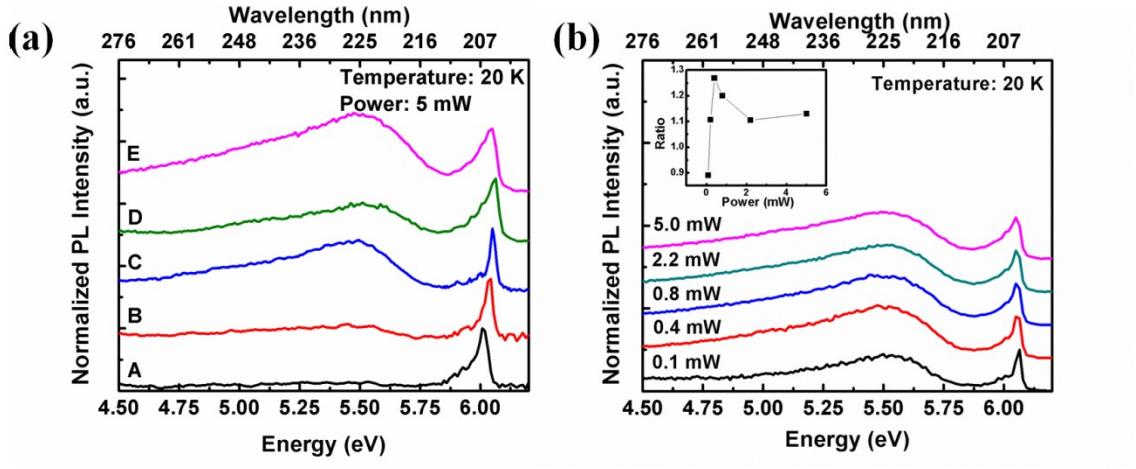

Figure 4.4 (a) Normalized PL spectra of Mg-doped AlN nanowires with different Mg flux and different growth rate at 20 K. (b) Power dependent PL spectra of sample E at 20 K; inset: ratio of integrated PL intensity of Mg-acceptor peak to that of band-edge peak versus power plot at 20 K.

presents the ratio of the peak intensities of Mg-acceptor peak to the band-edge peak. We observe that the ratio increases in the low power regime but decreases with further increasing excitation power. This is related to the saturation of the Mg-acceptor energy level under high excitation conditions. In addition, the power dependence of the peak energies reveals that both the high energy and low energy peaks undergo a red shift with increasing excitation power. The DAP recombination usually causes a blue shift with increasing power and has been observed in GaN [224] and InN [225]. It is suggested that the observed red shift is likely a combination of band gap renormalization [226] and laser induced heating effect. This effect has been observed in GaN nano-particles [227] and also in GaN/AlN quantum dots [228].

It is observed from the low temperature PL spectra of Fig. 4.4(a) that the low energy peak, P_L, is quite broad. To investigate this peak more closely, the PL spectrum was measured at room temperature using a frequency-quadrupled Ti-sapphire laser with an emission wavelength at 197 nm, 76 MHz repetition rate, and an average optical power of ~1 mW as the excitation source. The room temperature PL spectrum of sample E is presented in Fig. 4.5. In addition to the band-edge peak at 5.95 eV, three other peaks were observed at 5.34 eV, at 4.57 eV, and at 3.9 eV. The peak at 5.34 eV can be identified as the Mg-acceptor related transition (the energy separation of the band-edge

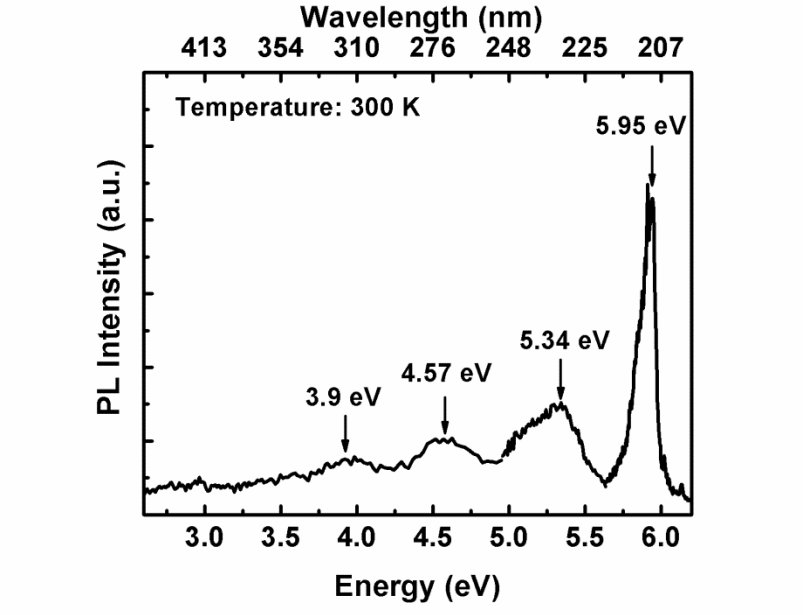

Figure 4.5 Room temperature PL spectrum of sample E. A 197 nm frequency-quadrupled Ti-sapphire laser was used as the excitation source.

peak and the peak at 5.34 eV is 0.61 eV). The emission peaks at 4.57 eV and at 3.9 eV are attributed to the DAP transitions. The transition involving a deep donor and Mg-acceptor energy level is responsible for the peak at 4.57 eV whereas the peak at 3.9 eV is due to the transition involving a shallow donor and a deep acceptor. Such transitions were also observed in Mg-doped AlN epilayers [147].

The temperature dependent PL properties were investigated for the highly doped AlN sample under an excitation power of 5 mW using the 193 nm ArF excimer laser as the excitation source. As the temperature increases, both peaks undergo a red shift. This is consistent with the band gap narrowing with temperature [146]. The evolution of the peak energy with temperature is presented in Fig. 4.6(a). The temperature dependent band-gap change can be explained by the Varshni's equation [229], $E_g(T) = E_g(0) - \frac{\alpha T^2}{(\beta+T)}$, shown as the solid line in Fig. 4.6(a), with the following parameters, $E_g(0) = 6.05\,eV$, $\alpha = 1.8\,meV/K$, and $\beta = 1462\,K$. These values agree well with the standard values of AlN in this temperature range [230]. We have also studied the evolution of the Mg-acceptor peak with temperature. The integrated PL intensity as a function of inverse temperature is plotted in Fig. 4.6(b). The solid line is the least square fit of experimental data with the

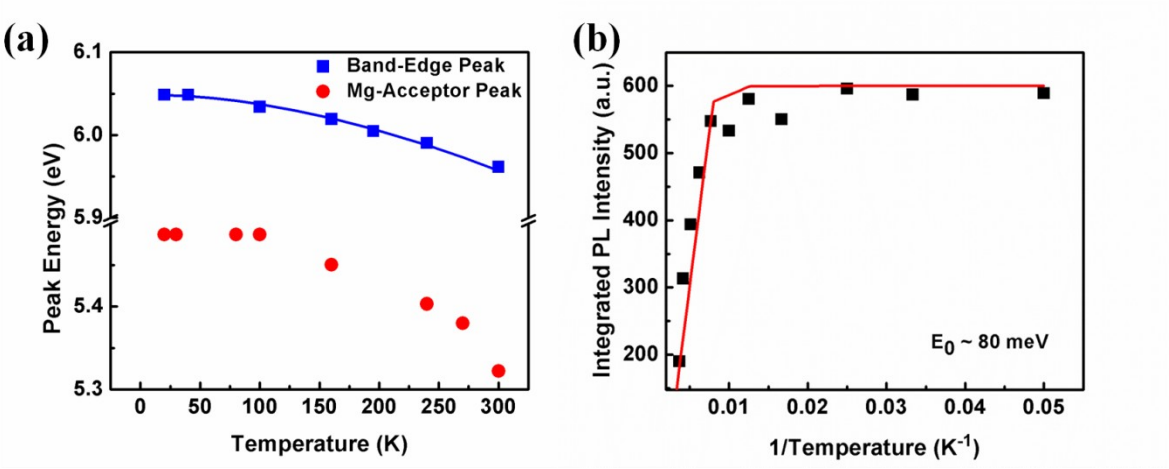

Figure 4.6 (a) Peak energy variation with temperature for band-edge and Mg-acceptor peaks of sample E. The solid line is the calculation by the Varshni's equation. (b) Integrated PL intensity versus inverse temperature plot for the Mg-acceptor peak. The solid line is the least square fit of the experimental data with the equation, $I_{emi} = I_0/(1 + aexp(\frac{-E_0}{KT}))$.

equation $I_{emi} = I_0/(1 + a\exp(-E_0/KT))$, where I_{emi} denotes the integrated PL intensity at various temperatures, I_0 represents the integrated PL intensity at 0 K, and E_0 is the activation energy of the PL emission intensity. For the Mg-acceptor peak, this fitted activation energy is ~80 meV, suggesting that the Mg-related transition is due to the DAP transition involving a Mg-acceptor energy level and a shallow donor. This activation energy is also comparable to the values (~60 meV) reported for AlN epilayers [146].

4.2.2 Electrical Characterization

We have subsequently investigated *p*-type conductivity by measuring the temperature-dependent I-V characteristics of large area AlN:Mg nanowire arrays. The device structure (sample F) is schematically shown in Fig. 4.7(a), which consists of a GaN/InGaN tunnel junction grown on heavily *n*-doped Si substrate, a 90 nm thick AlN: Mg section followed by a 10 nm AlGaN contact layer. The growth condition of AlN:Mg section is similar to the growth condition of sample E. The tunnel junction was designed to facilitate the carrier transport from *n*-Si substrate to the *p*-AlN layer. To subtract the resistance associated with the substrate, tunnel junction and contact region, another identical structure (sample F′) but without the AlN:Mg section was fabricated. The difference in resistivity of these two structures can provide a reasonable estimation of the AlN:Mg

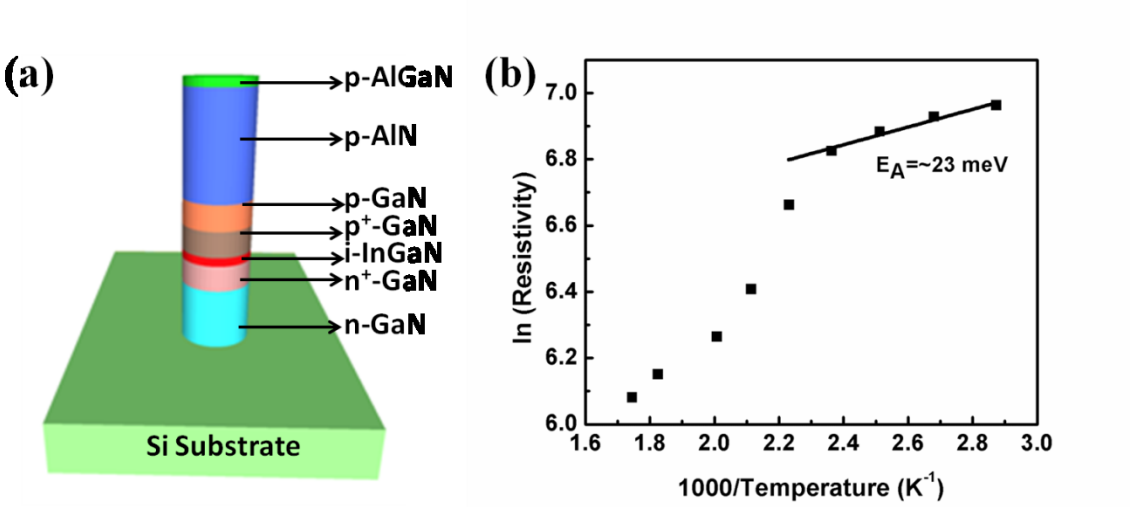

Figure 4.7 (a) Schematic illustration of the structure to calculate the resistivity of AlN: Mg nanowires; (b) Resistivity versus inverse temperature plot for AlN:Mg segment of sample F.

nanowire resistance. The nanowires were fabricated following the procedures described in Section 2.2.1. The I-V characteristics were measured in the temperature range of 298 K to 573 K and the resistance is calculated by the slope of the I-V curve in the forward bias region. The variation of AlN:Mg resistivity with inverse temperature is plotted in Fig. 4.7(b), which clearly reveals the presence of more than one activation energy. To discern the mechanism responsible for conduction at different temperature regions, the calculated resistivity is fitted to the equation, $\rho(T) = \rho_0 \exp\left(\frac{E_A}{KT}\right)$; where E_A is the thermal activation energy of resistivity. E_A is derived to be ~23 meV for the AlN:Mg segment. Such an unusal low activation energy, compared to the Mg-acceptor energy level (~600 meV), suggests that the hole transport mechanism is mainly governed by hole hopping and/ or impurity band transitions [218, 219]. In the hopping conduction, carriers hop from one localized state to another; the localized states could be at the same or at different energy levels. It is observed in Fig. 4.7(b) that the experimental data and the fitting curve follow each other closely in the temperature range of 300 K – 450 K and there is a deviation at higher temperature range. This deviation suggests that at higher temperatures the thermal activation of carriers starts to play a role and at a sufficiently high temperature, thermal activation would be the dominating hole transport mechanism. This phenomenon has also been observed for $Al_{0.7}Ga_{0.3}N$ [218], InGaN [231], and GaN

[219]. With the room temperature resistivity value of 697 Ω-cm and assuming an upper boundary of hole hopping mobility of 1 $cm^2 \cdot V^{-1} \cdot s^{-1}$ [232], the room temperature hole concentration of the AlN:Mg segment of sample F is found to be in the order of 10^{16} cm^{-3}, which is orders of magnitude higher than previously reported AlN:Mg epilayers [232]. The excellent *p*-type conductivity of AlN:Mg nanowires can be partly attributed to the drastically reduced nitrogen-vacancy related defects during the growth of nanowire structures under nitrogen-rich conditions as well as the enhanced dopant incorporation in nanowire structures [223].

4.3 Conclusion

The growth and optical performance of AlN nanowires have been presented in this chapter. The AlN nanowires demonstrate strong FX emission peak at low temperature and even at room temperature. Compared to the AlN epilayer, AlN nanowires exhibit supreme crystalline quality which is indicated by the narrow FWHM and strong emission at 300 K. The phonon replicas are identified as the SO phonon replicas instead of the commonly observed LO phonon replicas in AlN epilayer. The successful Mg-doping of AlN nanowires has also been demonstrated. By changing the growth parameters, the doping level can be controlled and AlN nanowires with different Mg-doping levels can be successfully grown. The fundamental optical properties regarding power and temperature dependence have also been discussed in detail. A detailed analysis of the hole conduction at different temperature ranges has been presented. It has been shown that the hopping conduction dominates the carrier conduction mechanism at 300 K ~ 450 K temperature range and the free hole concentration at room temperature is estimated as 10^{16} cm^{-3}.

Chapter 5. $Al_xGa_{1-x}N$ Nanowire LEDs

The growth and performance characteristics of nanowire III-nitride UV LEDs operating at UV-A (340 nm), UV-B (290 nm), and UV-C (210 nm) range have been discussed in this chapter. Compared to III-nitride InGaN/GaN based LEDs, AlGaN LEDs pose more challenges in terms of growth, fabrication, and characterization. These challenges in growth include the larger lattice mismatch of AlGaN with the conventionally used substrates (Si, sapphire, SiC), the different growth kinetics of Al adatom, and difficulty in impurity doping. The large lattice mismatch results in higher dislocation density and consequently, poor material quality, resulting in poor IQE. Larger sticking coefficient of Al adatom causes the formation of grain boundaries and dislocation. Furthermore, the large band gap of AlGaN (specially, in DUV range) poses additional challenge for impurity doping. The impurity activation energy increases almost linearly with band gap and the Mg-acceptor energy is as high as 600 meV for AlN. However, nanowire LEDs can address these issues to a great extent. By virtue of effective strain relaxation through lateral surfaces, nanowires can offer better crystal quality. Impurity doping is also enhanced in nanowire structures due to the reduced formation energy of substitutional doping in the near surface region of nanowires. Another important fact is that, deep UV emission is absorbed by many materials, including polyimide, ITO. This poses additional challenge in UV LED fabrication. Furthermore, due to the unique valence band structure of AlGaN, the emitted light is polarized; making the light extraction even more difficult. In this chapter, the characteristics of UV LEDs emitting at 340 nm, 290 nm, and 210 nm have been investigated. The optical and electrical properties of these LEDs have been studied intensely and the enhanced performance of these LEDs has been reported. We report IQEs as high as 59% for 41% for 340 nm and 290 nm LEDs, respectively.

5.1 Highly Efficient Spectrally Pure 340 nm Ultraviolet Emission from $Al_xGa_{1-x}N$ Nanowire Based LEDs

UV LEDs have a wide range of applications in biosensors and medical devices. Among these applications, there is a special importance for UV emission at 340 nm. It can be used for the measurement of fluorescent life time of reduced nicotinamide adenine

dinucleotide (NADH). NADH is an important coenzyme found in all living cells and plays an important role in the chemical reaction to generate energy. This NADH has a strong absorbance at 340 nm and a fluorescent peak at 450 ~ 460 nm [233-235]. The UV emission at 340 nm can also be used to optically control neurons, and in flash photolysis to stimulate the caged compound to release active molecules. This has a very important application in implantable neurotransmitters [236, 237]. The conventional UV light sources are not ideal for such applications due to their large sizes, inflexibility, and toxic side effects. In this context, nanowire UV LEDs can be used efficiently for such applications. They offer small size, flexibility and enhanced tunability. In this section, the highly stable and spectrally pure emission at 340 nm from $Al_xGa_{1-x}N$ heterojunction LED will be presented. The devices present enhanced optical and electrical performance with highly stable emission characteristics.

5.1.1 Growth and Structural Characterization

The schematic diagram of the AlGaN nanowire UV LED is presented in Fig. 5.1(a). The LED was grown on *n*-Si (111) substrate by PAMBE in nitrogen rich conditions. *n*-GaN nanowires were spontaneously grown on the Si substrate at 750 – 800 °C. A 40 nm undoped $Al_{0.12}Ga_{0.88}N$ active region, sandwiched between 100 nm *n*-$Al_{0.36}Ga_{0.64}N$ and 100 nm *p*- $Al_{0.36}Ga_{0.64}N$ were grown on *n*-GaN. A thin 30 nm *p*-GaN was grown on top to achieve better ohmic contact. The nitrogen flow rate and the plasma forward power were kept at 1 sccm and 350 W during the growth. The Al composition in the active region and cladding layers were controlled by varying the Al/Ga flux ratio. The SEM image, presented in Fig. 5.1(b), shows that the nanowires are vertically aligned and distributed uniformly throughout the wafer. To analyze the structural characteristics in detail, the HAADF-STEM image and the EDXS line scans are presented in Fig. 5.2. The contrast in the HAADF image in Fig. 5.2(a) clearly shows the formation of the $Al_xGa_{1-x}N$ heterostructures along with the GaN region. This can also be confirmed from the EDXS line scanning presented in Figs. 5.2(c). The line scan along the axial direction (line a-b in Fig. 5.2(a)) is presented in Fig 5.2(c). As we move from a to b, Ga signal is stronger (Al signal is close to zero) in the region closer to point a, indicating the formation of the *p*-GaN region. As we move towards point b, Ga signal intensity decreases and Al signal

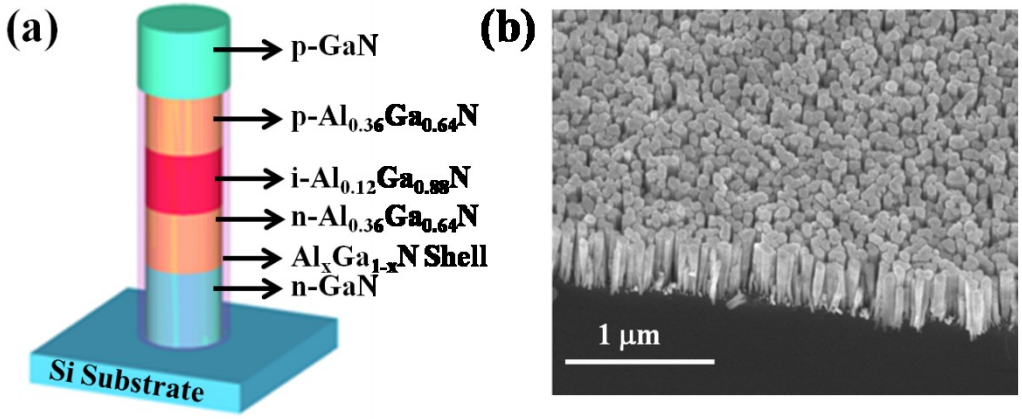

Figure 5.1 (a) Schematic diagram of the $Al_xGa_{1-x}N$ double heterostructure UV LED. (b) SEM image of the $Al_xGa_{1-x}N$ nanowires on Si substrate.

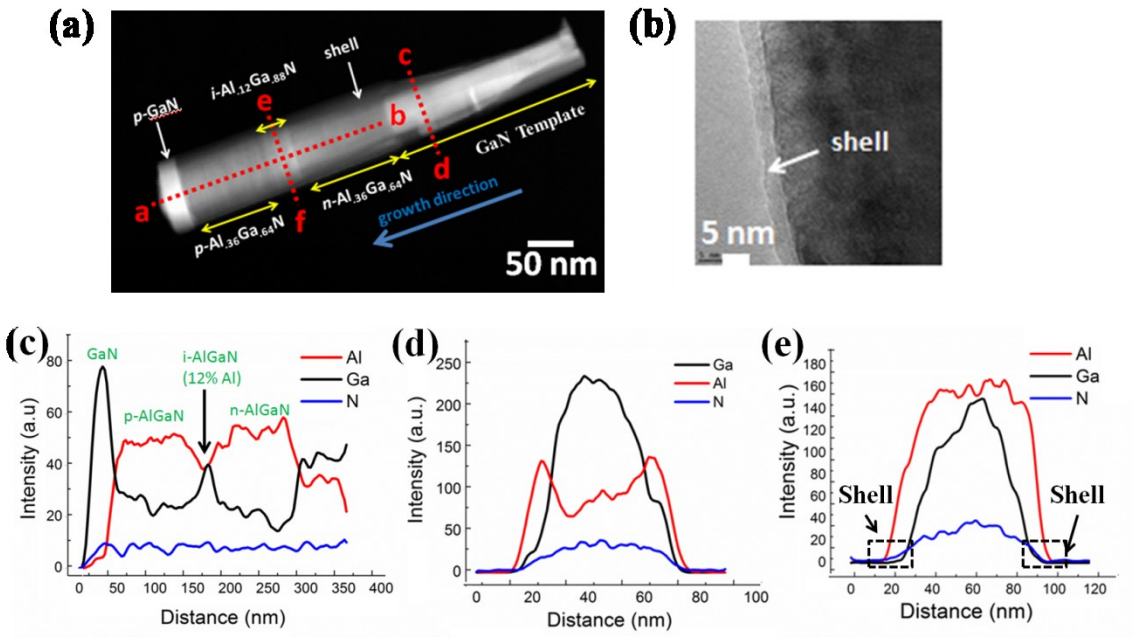

Figure 5.2 (a) The double heterostructure and the Al-rich shell is presented in the HAADF-STEM image of a single nanowire.(b) The formation of shell is confirmed from the HR-TEM image taken at the edge of the active region. The EDXS line scans are presented along (c) line a-b, (d) c-d, and (e) e-f.

intensity increases. However, in the middle of a-b line, a small increase in Ga signal intensity is observed indicating a lower Al concentration in that region. This confirms the formation of the $Al_xGa_{1-x}N$ heterostructures. It is worth mentioning here that due to the relatively short diffusion length of the Al adatom, an Al rich $Al_xGa_{1-x}N$ shell is formed along the lateral direction of the nanowire. Figure 5.2(b) presents the high resolution TEM image taken at the edge of the active region and the color contrast clearly exhibits the formation of the Al-rich shell along the lateral dimension of the nanowire LED. This is again confirmed by the EDXS line scan along the lateral direction: along line c-d (presented in Fig. 5.2(d)) and line e-f (presented in Fig. 5.2(e)). Line c-d is across the GaN template region; however, the line scan in Fig. 5.2(d) presents a strong Al signal at the surface and a dip in between confirming the formation of $Al_xGa_{1-x}N$ shell surrounding the GaN core region. Line e-f is across the active region; the presence of the shell is not as clear as it is along line c-d. The reason is that the shell thickness is not uniform and is gradually varied from 15 nm to a few nm along the growth direction. However, the presence of this shell can be identified by the faster rising trend of the Al signal compared to the Ga signal in the near surface region of Fig. 5.2(e) (highlighted by the black box). As discussed in Section 3.2, the formation of such a shell in the lateral direction is advantageous since it can suppress non-radiative recombination at the surface to a great extent and thus helps to improve the quantum efficiency of the device.

5.1.2 Optical Characteristics

The optical properties are investigated by means of power and temperature dependent PL spectroscopy. A 266 nm diode pumped solid state (DPSS) Q-switched laser is used as the excitation source for the PL measurement. The room temperature power dependent PL spectra are presented in Fig. 5.3(a). Four peaks are observed at high power from the PL spectra. However, at very low power (5 μW) the emission from the active region ($Al_{0.12}Ga_{0.88}N$) at 340 nm (E_1) dominates. This is due to the effective carrier confinement of the active region in the double heterojunction structure. As the power increases, two other peaks, emitting at 310 nm (E_2) and 295 nm (E_3) are revealed. E_3 peak is due to the emission from the $Al_{0.36}Ga_{0.64}N$ cladding layers having high Al composition. The origin of the E_2 peak is probably defect associated radiative recombination in doped $Al_xGa_{1-x}N$.

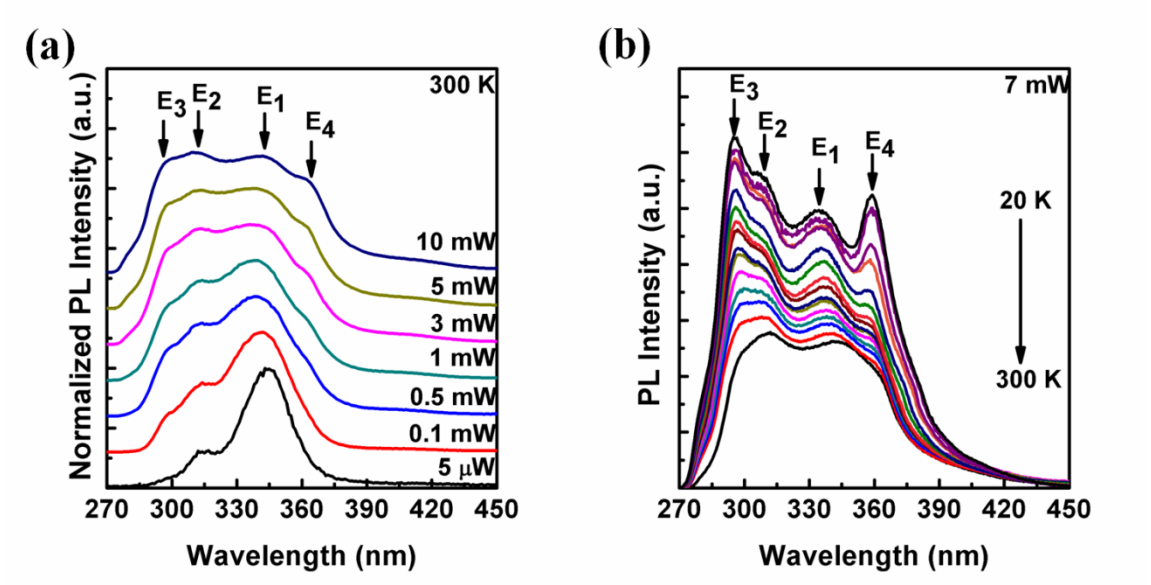

Figure 5.3 (a) Power dependent PL spectra measured at room temperature. (b) Temperature dependent PL spectra measured at 7 mW excitation power.

Such sub-band parasitic emission is often observed in $Al_xGa_{1-x}N$ MQW deep UV LEDs [238, 239]. As the excitation power increases, photo-excited carriers with a high thermal energy escape from the active region and recombine in the cladding layers. Furthermore, the cladding layers also absorb the laser and generate stronger emission with increasing power. This results in the saturation of the E_1 peak and the stronger E_3 peak with increasing power. At very high power, the emission from the GaN is also observed at 364 nm (E_4).

Temperature dependent PL spectra (from 20 K to 300 K) at an excitation power of 7 mW are presented in Fig. 5.3(b). Strong emission from the cladding layers are observed at low temperature. At low temperature, the non-radiative recombination centers are inactive and hence, they have negligible effect on the optical properties of the cladding layers. Moreover, the strong absorption of the top *p*-type cladding layer and the relatively large material volume of the cladding layers result in the strong emission of E_2 and E_3 peaks. A strong E_4 peak is also observed at low temperature. However, as the temperature increases, the defects and the non-radiative recombination centers become more active, resulting in the reduction of these peaks. The reduction of the active region peak, E_1, is smaller compared to the reduction in E_2, E_3, and E_4 with increasing temperature, demonstrating superior crystal quality and better carrier confinement of the active region.

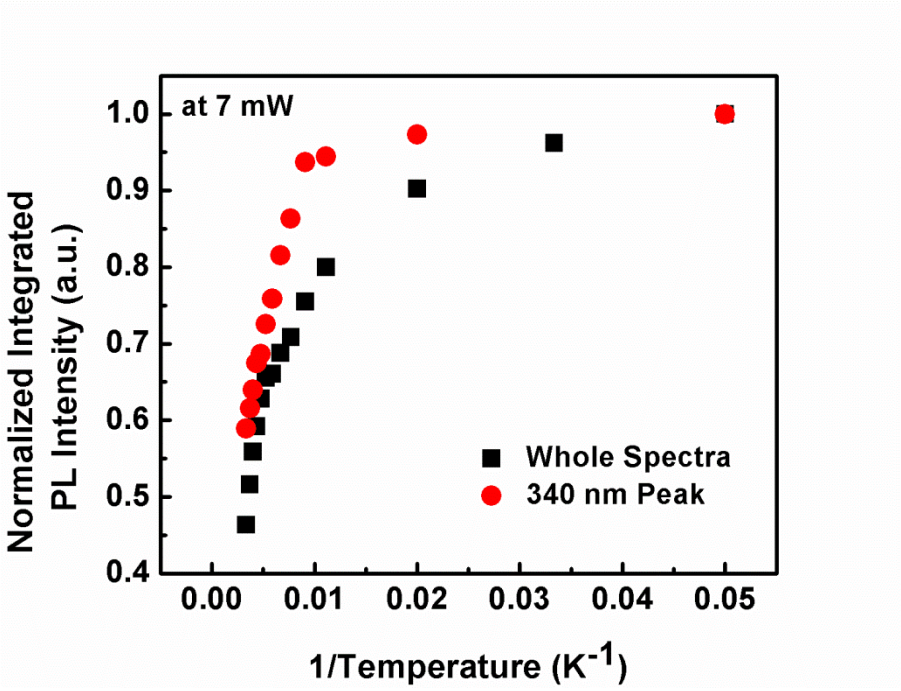

Figure 5.4 Integrated PL intensity versus inverse temperature plot for $Al_xGa_{1-x}N$ double heterojunction nanowire LED.

The comparison of low temperature and room temperature PL intensity provides an estimation of the IQE of the device. Figure 5.4 shows the normalized integrated PL spectra versus inverse temperature plot. We observe that the room temperature intensity at 7 mW remains about 46% of the low temperature intensity at the same power, demonstrating an IQE of 46%. However, this integrated PL intensity consists of emission from all layers, including cladding layers and GaN layer. So the evolution of the E_1 peak with inverse temperature is also analyzed. From this plot, we observe that the room temperature intensity is at about 59% of its low temperature value. This IQE is higher than the IQE of undoped $Al_xGa_{1-x}N$ under similar conditions. This improvement in the IQE is due to the superior crystal quality and better carrier confinement in both lateral and vertical directions, provided by the shell region and cladding layers, respectively.

5.1.3 Electrical Characteristics

The fabrication of the $Al_xGa_{1-x}N$ UV LEDs is carried out following the standard fabrication technique as described in Section 2.2.1. In III-nitride nanowires, the formation energy for substitutional doping in the near surface region is minimized which results in

enhanced conductivity [240] and hence, good electrical performance is expected from nanowire LEDs. The I-V curve of a 0.3 × 0.3 mm^2 device is presented in Fig. 5.5(a). It shows good diode characteristics under forward bias condition, with 6.3 V at 20 mA injection current. The estimated series resistance is ~50 Ω. Such good results outperform the ZnO based nanowire LEDs in the near UV/ UV regions [241-245] and are even comparable to the thin film MQW LEDs with the same peak emission wavelength [234, 246-249]. The leakage current under reverse bias condition is 4×10^{-6} A at -10 V, which is higher compared to the thin film UV LEDs [250]. This high leakage current may be due to the insufficient insulation provided by polyimide. Furthermore, surface recombination at the side wall of the nanowire can be a source of high leakage current. A good filling material with high resistance and surface passivation scheme can reduce the high leakage current to a great extent.

Figure 5.5(b) presents the current dependent EL spectra of the UV device. Devices from different region of the wafer show similar EL spectra, confirming good uniformity over the wafer. The EL shows a strong and stable emission at 340 nm, without any parasitic emission at the visible wavelength range. The parasitic emission due to the presence of deep level defects is often observed in $Al_xGa_{1-x}N$ MQW based UV LEDs [145, 238]. We also observe a very small shift (< 2 nm) in the peak position with increasing current. This confirms that nanowire LEDs have negligible polarization field due to effective lateral stress relaxation. The FWHM of the EL spectra is about 30 nm and is almost independent of the injection current.

The relative EQE curve is presented in Fig. 5.6, under CW and pulsed biasing condition. The EQE under 1% duty cycle at pulsed biasing mode does not show any droop at a current density as high as 350 $A \cdot cm^{-2}$. This signifies the fact that polarization effect and defect related Auger recombination are negligible for nanowire LEDs [79]. However, under CW biasing mode, droop is observed at a current density of 100 $A \cdot cm^{-2}$. This is due to the self heating effect [251, 252] and poor thermal conductivity of nanowire LEDs. Utilizing a good passivation material with high thermal conductivity will reduce this thermal issue to a great extent.

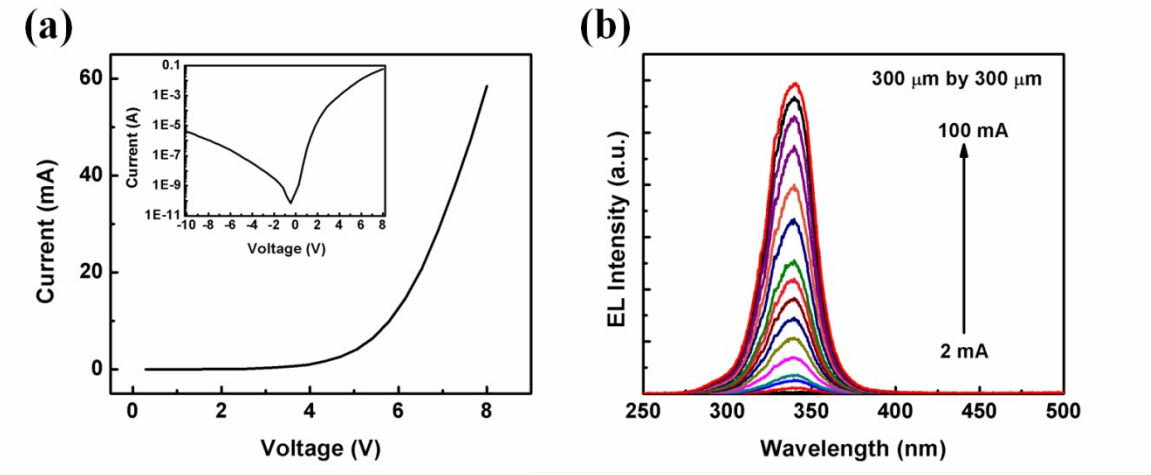

Figure 5.5 (a) The room temperature I-V curve of the $Al_xGa_{1-x}N$ nanowire LED for device size of 0.3 × 0.3 mm^2. Inset: I-V characteristics of the device under forward and reverse bias conditions in semi-log scale. (b) Typical EL spectra measured at room-temperature with continuous wave biasing condition of a 0.3 × 0.3 mm^2 device.

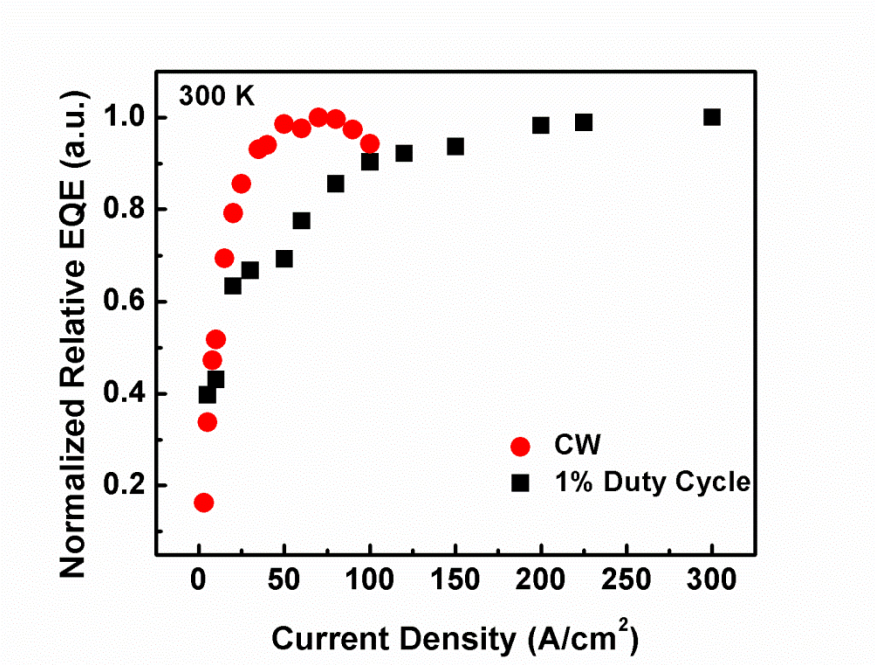

Figure 5.6 Relative EQEs of the $Al_xGa_{1-x}N$ nanowire LEDs measured at room-temperature by using CW and pulsed injection current with 1% duty cycle. The self heating effect is observed under CW biasing condition.

5.2 Sub-300 nm Deep Ultraviolet Emission from $Al_xGa_{1-x}N$ Homojunction Nanowire LEDs

In this section, the UV emission from $Al_xGa_{1-x}N$ homojunction structure at 290 nm has been presented. The optical and electrical characteristics reveal the stable emission at 290 nm. An IQE of 41% has been achieved, which is comparable to the planar MQW based UV LEDs in this range. This high IQE value can be attributed to the enhanced material quality and the formation of the core-shell structure which can reduce the surface non-radiative recombination.

5.2.1 Growth and Structural Characterization

The schematic diagram of the homojunction $Al_xGa_{1-x}N$ nanowire LED is presented in Fig. 5.7(a). The LED is grown on *n*-doped GaN template on *n*-Si (111) substrate. A 90 nm thick Mg-doped $Al_{0.38}Ga_{0.62}N$ layer works as the active region. This layer is sandwiched between highly *n*- and *p*-doped $Al_{0.38}Ga_{0.62}N$ layers, both having thicknesses of 90 nm. The top *p*-doped $Al_{0.38}Ga_{0.62}N$ layer serves as the cladding layer and also facilitates hole transport. A highly Mg-doped 15 nm GaN layer is grown on the top as the contact layer. This homojunction UV LED structure can offer lower potential barrier compared to the heterostructure since Al-rich cladding layer is avoided here. To facilitate the carrier transport and to reduce the device resistance, Al composition is linearly graded from *n*- and *p*-doped $Al_{0.38}Ga_{0.62}N$ layer to GaN layer [253]. These graded layers are good for reducing the lateral spread of current by offering a more uniform resistivity. Figure 5.7(b) presents the SEM image of the nanowires. The nanowires are vertically aligned and uniformly distributed over the wafer. The nanowire density is estimated to be 10^{10} cm^{-2}. The TEM image is presented in Fig. 5.7(c). It shows that the nanowires are of tapered structure, having large diameter at the top. The formation of the core-shell structure is confirmed by the high resolution TEM image, presented in Fig 5.7(d). The TEM image is taken at the edge of the active region and in the high resolution image, the interface separating the core and the Al-rich shell is clearly indicated. This is also confirmed by the EDXS line scanning of the nanowire along lateral direction. The Al signal shows shoulder at the edges and a dip in the middle, confirming the presence of Al-rich shell region.

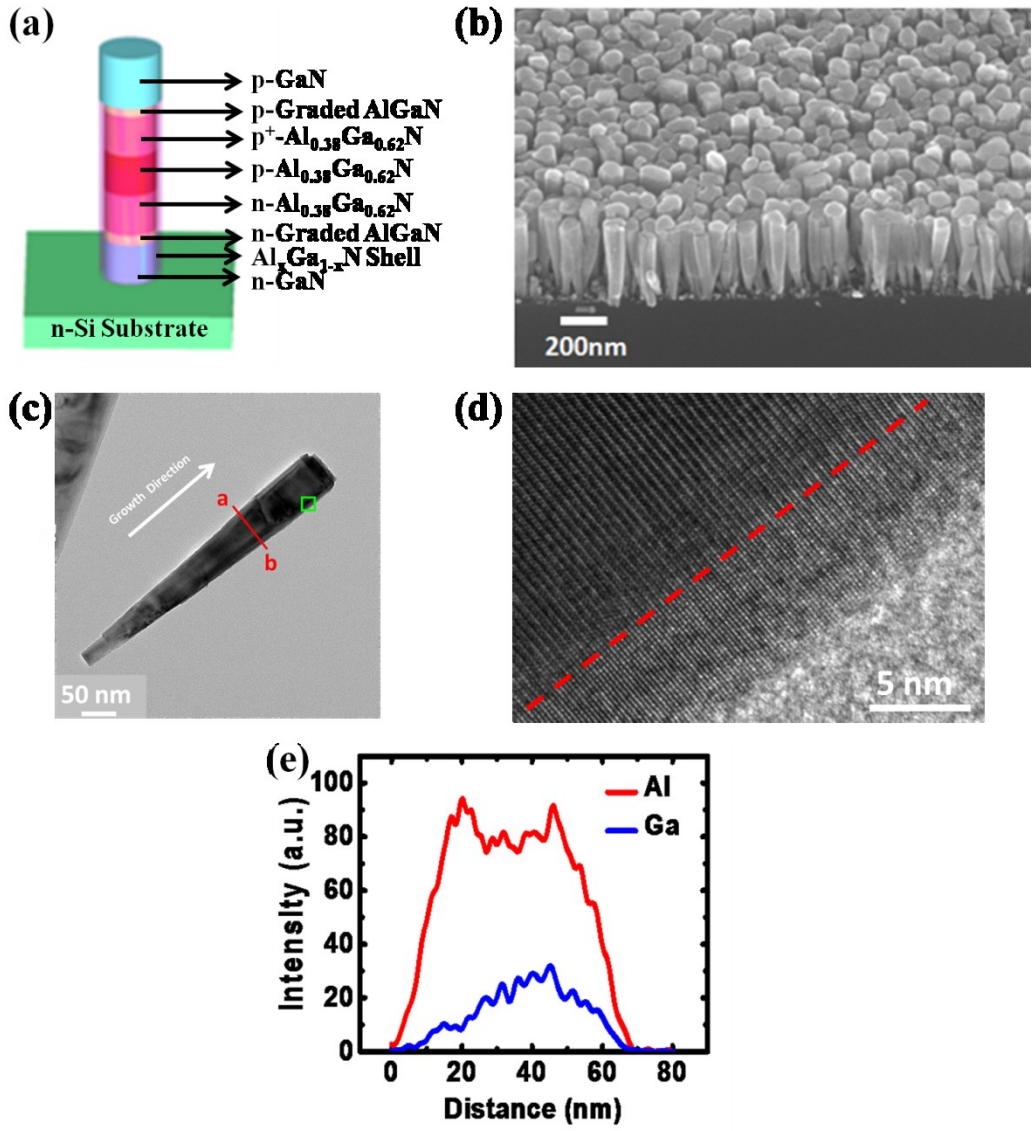

Figure 5.7 (a) The schematic diagram showing the $Al_xGa_{1-x}N$ homojunction nanowire based LED structure. (b) SEM image of nanowires grown on *n*-Si (111). (c) TEM image of a single nanowire. (d) HR-TEM image taken at the edge of nanowire revealing the formation of a shell around the sidewall of the nanowire. (e) Lateral elemental profile measured along a-b line in Fig.5.7(c) showing the core-shell structure.

5.2.2 Optical Characterization

Optical properties of the nanowire UV LEDs have been investigated using power dependent and temperature dependent photoluminescence spectroscopy. The optical excitation source is the same as described in section 5.1.2. Figure 5.8(a) shows the normalized power dependent (from 0.1 mW to 8 mW) PL spectra measured at room temperature. The PL exhibits three peaks at 290 nm, at 365 nm, and at 450 - 550 nm. The first peak at 290 nm is originated from the $Al_{0.38}Ga_{0.62}N$ active region of the LED. At low excitation power, the peak from active region dominates. This peak undergoes negligible blue shift with increasing power, demonstrating the minimized QCSE in nanowire LEDs. The peak at 365 nm is the emission from the top *p*-GaN region. This peak undergoes a red shift at high excitation power exhibiting the laser heating effect on the thin GaN region. The broad emission peak at 450 – 550 nm is due to the deep level defect in the doped $Al_xGa_{1-x}N$ layers and is readily saturated as the power increases from 0.1 mW to 0.8 mW.

The IQE of this deep UV nanowire LED is studied from the temperature dependent PL spectroscopy. The normalized PL intensities as a function of inverse temperature is plotted in Fig.

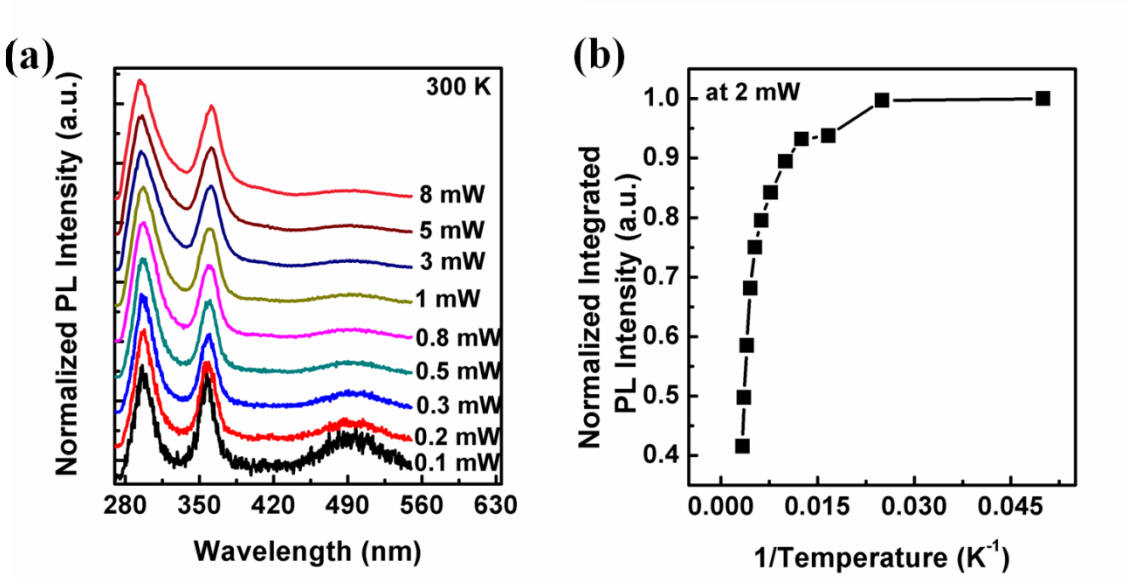

Figure 5.8 (a) Room temperature PL spectra of nanowire LEDs at different power from 0.1 mW to 8 mW. (b) Integrated PL intensities versus inverse temperature plot of the DUV peak at 290 nm. The room-temperature IQE is estimated to be 41%.

5.8(b) at an excitation power of 2 mW. Figure 5.8(b) presents that the ratio of the room temperature intensity to low temperature intensity, i.e., the IQE is around 41%. Such a high IQE value can be directly related to the drastically reduced defect densities in nanowire structures and reduction in surface recombination velocity due to the formation of the core-shell structure.

5.2.3 Electrical Characterization

The deep UV nanowire LEDs are fabricated using the standard fabrication procedures as described in section 2.2.1. The room temperature I-V characteristic of a 0.3 × 0.3 mm^2 device is presented in Fig. 5.9(a). A forward current of 25 mA at 12 V applied forward voltage is observed which points to a high resistance value compared to the planar $Al_xGa_{1-x}N$ LEDs. This may indicate that the growth of *p*-$Al_xGa_{1-x}N$ layer needs to be optimized since the doping window to achieve good conductivity is very narrow [254]. The leakage current is comparable to the planar LED structures despite of the surface state effects and insufficient passivation issues of nanowire LEDs. Figure 5.9(a) shows that the leakage current is 3×10^{-7} A at a reverse voltage of -10 V. The current dependent EL spectra of the same device measured under continuous wave biasing mode are presented in Fig. 5.9(b). A strong emission at 290 nm, originating from the $Al_{0.38}Ga_{0.62}N$ active region, is observed at high injection current. However, at low injection currents the peak at 290 nm appears as a weak shoulder and the presence of two defect related emission peaks at 310 nm and 500 nm are observed. These two peaks get saturated with a slight increase of injection current from 1 mA to 3 mA. On the other hand, the band-edge emission peak increases rapidly with increasing current and eventually becomes the dominating peak in the EL spectra. The peak at 310 nm evolves as a weak shoulder accompanying the main peak. The band-edge emission peak presents very little shift with increasing power indicating the presence of very low polarization field in the nanowire structure.

The temperature depended EL is also studied for this device. Figure 5.10 presents the integrated EL intensity versus temperature plot. In the low temperature regime (80 K ~ 150 K), the intensity increases with increasing temperature; then starts to decrease after reaching the maximum at 150 K. At low temperature, the defects have negligible effect;

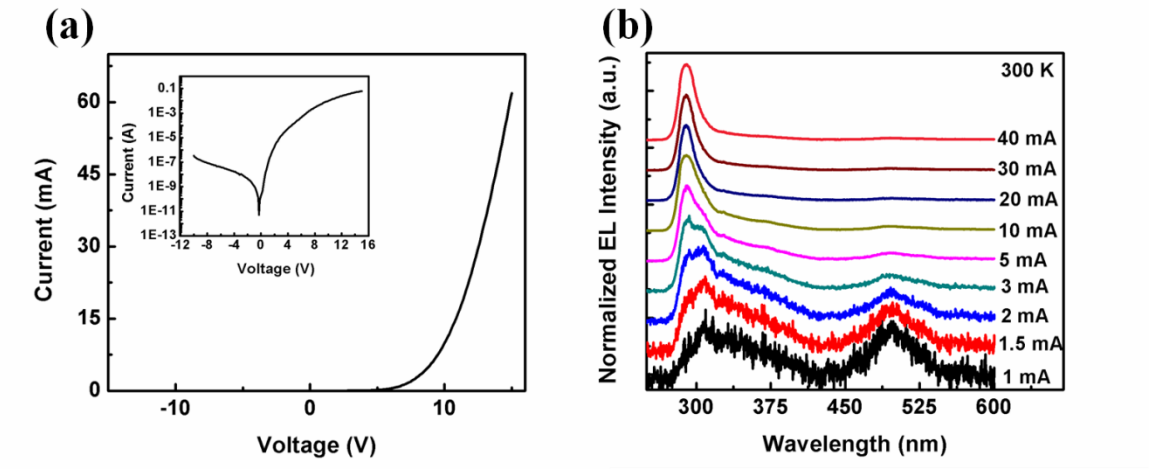

Figure 5.9 (a) Typical I-V curve of the $Al_xGa_{1-x}N$ homojunction nanowire LED with device size of 0.3 × 0.3 mm^2. Inset: I-V characteristic of the device under forward and reverse bias in semi-log scale. (b) Room temperature EL spectra of the $Al_xGa_{1-x}N$ homojunction nanowire LEDs under different injection current from 1 mA to 40 mA.

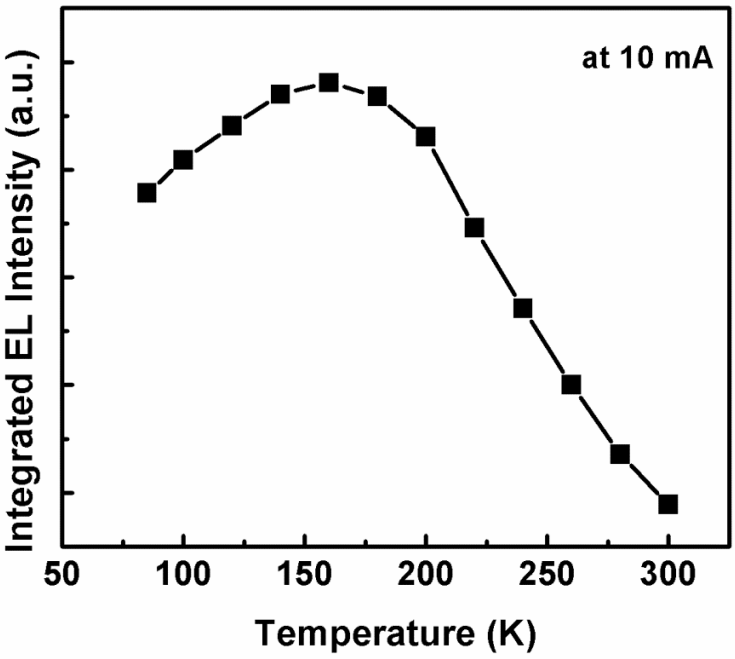

Figure 5.10 Integrated EL intensity versus temperature plot for the UV homojunction LED at 10 mA injection current. The plot shows maximum peak intensity at a temperature of 150 K.

however, the mobility of carriers; especially of holes, is also low. As the temperature increases, the mobility and effect of defects, traps and surface states become more prominent [255-259]. These two competing factors control the temperature dependent behavior and it is apparent from Fig. 5.10 that, prior to 150 K, the mobility of the carriers plays a significant role and after that, the effect of traps and surface states become more important.

5.3 Demonstration of Deep Ultraviolet Emission at 210 nm from AlN *p-i-n* LED

With the demonstration of enhanced optical performance of AlN nanowires in Chapter 4, it is possible to realize deep UV AlN LED emitting at 210 nm. The major challenges of achieving AlN LEDs are determined by the properties of AlN itself. In Chapter 4, it has been presented that the AlN nanowires grown by PAMBE demonstrate excellent optical properties. The free exciton emission at 6.03 eV at low temperature suggests the strain-free nature of the AlN nanowires [209, 217]. This has also been confirmed by the structural analysis presented in Section 4.1.1. Such strain-free AlN nanowires exhibit an IQE as high as 80%, confirming again the good material quality. Furthermore, the challenges of Mg-doping are critically addressed and the realization of AlN:Mg nanowires with different Mg doping has been demonstrated in Section 4.2. In this context, this chapter presents the successful realization of AlN *p-i-n* LED, which is the first demonstration of AlN nanowire LEDs at this wavelength range. The schematic diagram of AlN LED is presented in Fig. 5.11(a). The LEDs are grown on heavily Si-doped GaN template on *n*-Si substrate. The thickness of the GaN template layer is 80 nm. This layer is followed by a 90 nm Si-doped AlN, a 60 nm non-doped AlN, and a 15 nm Mg-doped AlN layers. A thin 10 nm AlGaN layer is deposited at the top as the contact layer. The Al nominal concentration is calculated to be 20% by the $Al/(Al + Ga)$ flux ratio. The growth parameters for the GaN template is the same as described in Section 4.1.1. For the AlN LED, the Si cell temperature is 1250 °C, which is equivalent to a doping lower boundary of 5×10^{17} cm^{-3} [240]. The Mg-cell temperature is 280 °C, which results in a Mg concentration of 1×10^{21} cm^{-3} in an AlN:Mg planar structure [80]. However, the free hole concentration for AlN nanowire with this doping level is deduced to be 1×10^{16} cm^{-3}, following the procedure described in Section 4.2.2. The PL spectra of

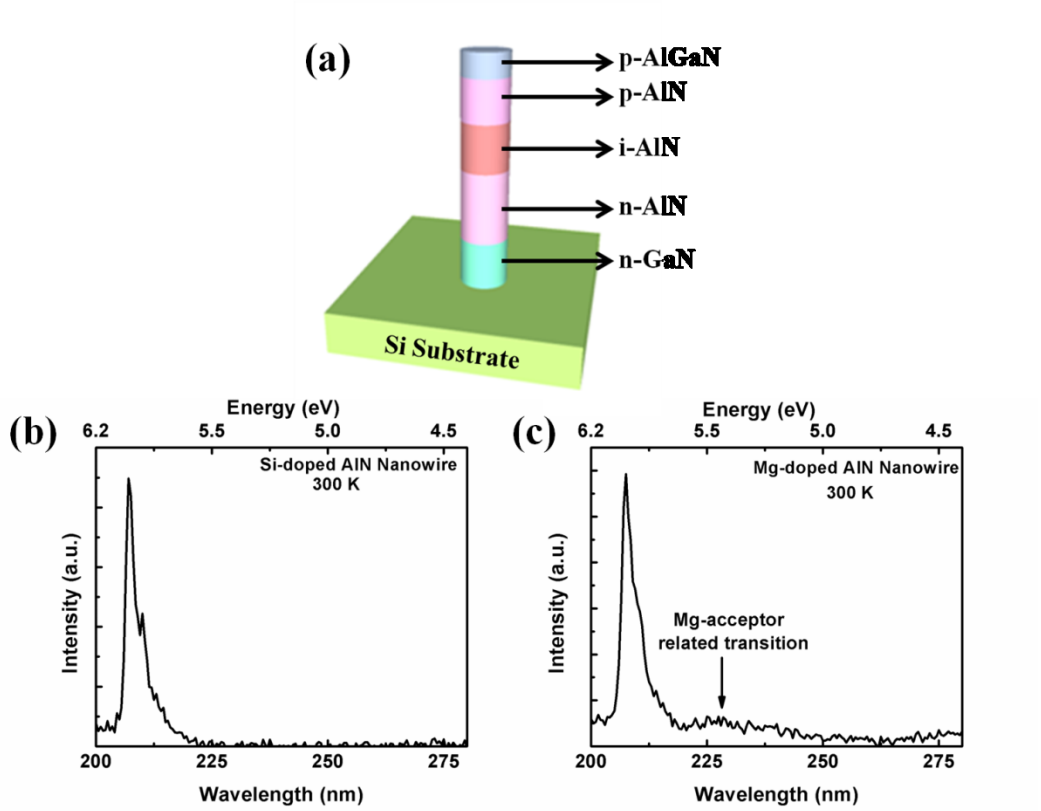

Figure 5.11 (a) Schematic diagram of the AlN *p-i-n* LED on GaN template on Si substrate. The room temperature PL spectra of AlN nanowires: (b) Si-doped, and (c) Mg-doped.

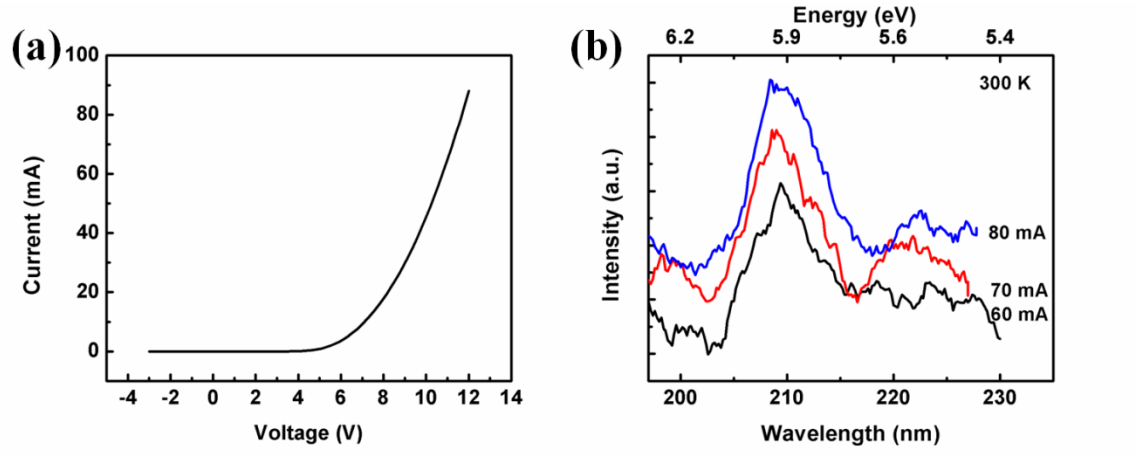

Figure 5.12 (a) The I-V characteristics of the AlN *p-i-n* LED. (b) The current dependent EL spectra of the AlN *p-i-n* LED.

corresponding *n*- and *p*-doped AlN are presented in Fig. 5.11(b), and 5.11(c), respectively.

The devices are fabricated following the procedure as described in Section 2.2.2. The I-V characteristic is presented in Fig. 5.12(a). The turn on voltage is ~6 V, which is close to the band gap energy of AlN. The operating voltage at 20 mA injection current is ~8 V. The first demonstration of AlN planar LED emitted at 210 nm presented a turn-on voltage of ~20 V with an operating voltage of 45 V at 20 mA [232]. The high turn-on voltage and high resistance are mainly originated from the poor material quality and inefficient impurity doping. However, our nanowire LEDs exhibit a significantly enhanced material quality and controllable impurity doping. This is further evidenced from the room temperature current dependent EL spectra presented in Fig. 5.12(b). A clear band edge emission at ~210 nm is observed in Fig. 5.12(b).

5.4 Conclusion

The enhanced performance characteristics of nanowire UV LEDs have been demonstrated in this chapter. We present emissions at 340 nm, 290 nm, and at 210 nm. The LEDs emitting at 340 nm and 290 nm present enhanced performance with IQEs as high as 59% and 41%, respectively. However, most important achievement described in this chapter is the realization of AlN *p*-*i*-*n* LED emitting at ~210 nm. There has been no report on the demonstration of UV nanowire LEDs emitting at 210 nm till today. Not only that, the *p*-*i*-*n* LEDs also exhibit good electrical characteristic. A clear band-edge emission is observed at ~210 nm and the I-V curve shows low turn-on voltage (~6 V). This enhanced performance can be attributed to the unique properties of nanowires, such as, effective stress relaxation, and enhanced impurity doping. The successful demonstration of this LED will lead the way to realize tunable deep UV LED with enhanced optical and electrical performance.

Chapter 6. Conclusions and Future Works

6.1 Conclusions

In this thesis, we have discussed the properties of the III-nitride LEDs in a broad spectrum, covering emission in both UV and white spectral range. We have intensely investigated the optical and electrical properties of InGaN/GaN white LEDs and AlGaN UV LEDs. We have demonstrated the highest CRI value (97.7) achieved from a nanowire white LED. We have also presented the first demonstration of the emission from an AlN LED using nanostructures. The major findings of this thesis are summarized below.

The III-nitride nanowire structures can outperform their planar counterpart in many respects. One of the fundamental problems of III-nitride devices is the lack of lattice matched substrate. This results in poor material quality for planar structures. However, by means of strain relaxation through lateral surfaces, nanowires can accommodate the strain in an effective way, resulting in significantly enhanced crystal quality. By using nanowire structures, we have presented the strain-free formation of AlN nanowires, which is very challenging due to the large lattice mismatch between AlN and the available substrates. Furthermore, polarization and therefore, the problems associated with polarization, such as, QCSE, is less prominent in nanowire structures. However, one big demerit of nanowire structures is the presence of surface states. The high density of surface states can affect the device performance significantly. The injection efficiency, and therefore, the QE of the device can be significantly reduced due to the presence of the surface states. By using APSYS simulation tool, we have shown that the injection efficiency can be as low as 6% for $In_{0.25}Ga_{0.75}N$/GaN nanowire structures having 100 nm diameter, whereas planar structures enjoy ~100% injection efficiency. The injection efficiency can be increased if the surface recombination velocity is reduced, which can be done by employing surface passivation techniques. Inspired from this result, we have designed an in-situ surface passivation scheme wherein AlGaN layer is grown laterally surrounding the InGaN/GaN nanowires. This results in significantly improved performance. An output power of 1.5 mW has been achieved for a current density of 70 $A \cdot cm^{-2}$ from the

core-shell LED structure, which is two orders of magnitude larger than its non-core-shell counterpart.

We have also analyzed the functional properties, such as, CCT and CRI of InGaN/(Al)GaN white LEDs. Both CCT and CRI are important quality metric for white LEDs. CCT and CRI depend on the SPD of the light source and we have shown that it is easy to tune the SPD of InGaN/GaN nanowire LEDs by changing the growth conditions. We have presented that the InGaN/GaN white LEDs can achieve CRIs as high as 95.6 in the cool white region and 97.7 in the warm white region.

To realize the deep UV emission, it is of prime interest to study the optical properties of AlN nanowires. As mentioned previously, due to having larger band gap of AlN and different growth kinetics of Al than Ga adatom, it is more challenging to grow AlN of good quality. Exploiting the advantages of nanowire structure, we have presented the enhanced optical properties of the strain-free non-doped AlN nanowires. The AlN nanowires present stronger emission and narrower FWHM compared to previously reported high quality AlN epilayers. In addition, enhanced impurity doping and conductivity can be achieved from nanowire structures due to the reduced formation energy of substitutional dopants at the near surface region of nanowires. Impurity doping, especially, efficient Mg-doping is very difficult for AlN epilayers. In this work, we have presented controllable Mg-doping in AlN nanowires. By changing the growth conditions, such as, Al flux and Mg flux, we have shown that it is possible to achieve AlN nanowires with different Mg-doping. The signature of the different doping levels can be confirmed by observing the Mg-related transition in the PL spectra of these nanowires. The PL spectra do not exhibit any defect peak at 3.9 and 4.7 eV, further confirming the superior quality of the AlN nanowires.

We have also presented the UV emission at 340 nm (UV LED1), 290 nm (UV LED2), and most importantly, at 210 nm (UV LED3). UV LED1 and UV LED2 both exhibit enhanced optical and electrical properties. The presence of core-shell structure has been observed for both UV LED1 and UV LED2. This prohibits surface recombination, which can enhance the QE of the devices. The IQEs of UV LED1 and UV LED2 are 59%, and 41%, respectively. The improved electrical property of the LEDs can be reflected by their

small series resistances and small leakage current. The calculated series resistances of LED1 and LED2 are ~50 Ω and ~70 Ω for device sizes 0.3 × 0.3 mm^2, respectively.

We have presented the deep UV emission at 210 nm, which is the first demonstration of electroluminescence emission in such a short wavelength range using nanowire structure. The growth of strain and defect-free AlN has enabled the successful realization of AlN *p-i-n* LED, emitting at 210 nm. The UV LED3 presents good I-V characteristics with low turn-on voltage (6 V) and low operating voltage (8 V at 20 mA). The operating voltage at 20 mA of a *c*-plane planar *p-i-n* AlN and an *a*-plane AlN *p-n* LED emitting at 210 nm and 214 nm are 45 V and 13 V, respectively [232, 260]. Such enhanced I-V performance of the AlN *p-i-n* nanowire LED can be attributed to the improved crystal quality and enhanced surface doping in AlN nanowires. Strong EL emission is observed at room temperature and current dependent EL demonstrates increasing power with increasing injection current. This successful realization opens up the possibility to achieve tunable deep UV emitters and deep UV nanowire lasers.

6.2 Future Works

6.2.1 High Efficiency Deep UV LED

To date, the power and EQE achieved from the UV LEDs are very low. The main reasons of the low power and EQE are discussed in Chapter 1, which include the presence of polarization, poor crystal quality, and inefficient impurity doping. Novel design techniques, such as, polarization doping and superlattice structures should be considered to alleviate the extent of such problems [131, 132, 261-264]. In polarization doping, abrupt barriers are avoided by means of graded barrier. In one hand, it reduces the strain effect, and on the other hand, it can induce hole incorporation in the structure. This results in improved Mg-doping efficiency which is considered as the bottleneck for planar UV devices. Superlattice structure also enhances hole incorporation. In superlattice structure, two different band gap materials are grown on top of each other in a periodic manner and the carrier transport is enhanced by means of tunneling. However, the polarity of the III-nitride material should be carefully considered while designing the structure.

Another significant problem that hinders the efficiency of LEDs is the light extraction efficiency. As discussed in Chapter 1, light extraction efficiency is low for planar structure. For deep UV LEDs, it imposes additional challenge due to the unique valence band structure of AlN. As the Al composition increases, the emitted light tends to switch from TE to TM polarization [142]. The crossover point between TE and TM polarization depends on the strain and QW thickness and can be varied from Al mole fraction of ~0.25 to ~0.83 [265-269]. To enhance the light extraction efficiency in the deep UV range, we need to efficiently collect the TM polarized light. One approach is to design the structure to enhance TM polarized light extraction. For instance, designing the top *p*-GaN layer as microdomes [270] or use of Al metal for surface plasmon coupling [271] enhances TM polarized light extraction. Nanowire structure can also be beneficial in this context. It has been reported that the TM mode light extraction efficiency can be enhanced in nanowire structures [272]. This enhancement largely depends on the length and diameter of the nanowires. The optimization of these parameters along with introducing novel design to enhance light extraction efficiency is part of our future works.

6.2.2 Deep UV Nanowire Laser Diodes

There is a growing demand for AlGaN based deep UV LDs. However, due to the limitations of this material system, the AlGaN MQW LDs cannot result in enhanced performance. The shortest reported wavelength for electrically injected AlGaN MQW LD is 336 nm whereas optically injected laser can reach as low as 230 nm [273]. However, such LDs present extremely high threshold current density and low output power. In this context, nanowire AlGaN LD can result in enhanced performance. The enhanced optical and electrical properties of reported AlN nanowires are a great motivation for the success of this work. Furthermore, recently, electrically injected UV laser at 320 nm wavelength range has been demonstrated by our group [274]. Such laser also presents an extremely low threshold current density of ~10 $A \cdot cm^{-2}$.

Our proposed design of AlGaN based nanowire edge emitting LD is presented in Fig. 6.1. In this structure, the Si and Mg-doped AlN form the cladding layers. The waveguide

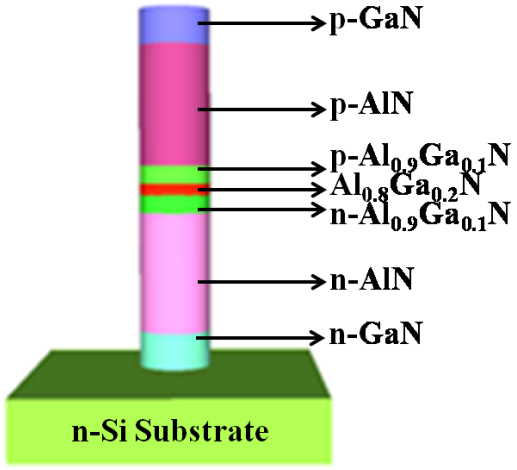

Figure 6.1 Schematic illustration of $Al_xGa_{1-x}N$ based deep UV laser on Si substrate.

consists of $Al_{0.8}Ga_{0.2}N$ active region, which is sandwiched between Si- and Mg-doped $Al_{0.9}Ga_{0.1}N$ layers. To provide optical feedback, distributed Bragg reflectors consisting of multiple SiO_x/air stacks will be fabricated on both ends of the high density AlGaN nanowire heterostructure array. The optical loss of this laser structure includes the loss through the substrate, top metal contact layer, mirror loss and loss due to photon absorption in the active region. The optical loss through substrate and top metal contact can be largely eliminated by careful optimization; the mirror loss can be carefully controlled by using multiple SiO_x/air distributed Bragg reflectors. A defect-free AlGaN nanowire heterostructure can be achieved by optimizing the growth parameters which will minimize the photon absorption loss in the device active region. The laser performance including the threshold current density, QE, output power, wall plug efficiency will be thoroughly studied and correlated with the design parameters in order to ensure maximum achievable performance.

6.2.3 Utilizing the Benefits of N-polar III-Nitride Materials

The polarization of III-nitride materials depends largely on the polarity (metal versus N) of the material. The spontaneous and piezoelectric polarizations are in the opposite direction for metal- and N-polar devices. It has been presented that N-polarity is beneficial compared to Ga-polarity for InGaN/GaN LEDs [275, 276]. Stable N-polar InN

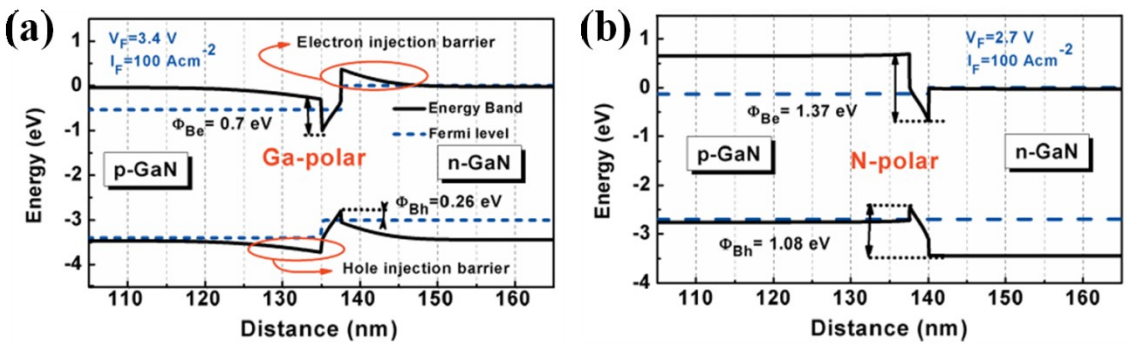

Figure 6.2**.** Simulated energy band diagram of a single QW InGaN/GaN LED device, (a) Ga-polar, and (b) N-polar [276].

can be grown by PAMBE at higher temperature [277, 278]. It asserts that higher In composition can be achieved in N-polar InGaN/GaN LEDs. Furthermore, the bias induced electric field and internal polarization fields are in the opposite (same) direction for N (Ga)-polar devices. This results in reduced QCSE and enhanced device performance for N-polar conventional *p*-top devices. The energy band diagram for Ga-polar and N-polar devices are presented in Fig. 6.2 [276]. It is apparent from the figure that the carrier injection is enhanced in N-polar devices due to the lower potential barrier experienced by the injecting carriers from the *n*- and *p*-side. Furthermore, the electron overflow can be effectively suppressed, even without the AlGaN EBL, due to the presence of the barriers caused by the polarization charges.

The polarity also plays a significant role in the device performance of UV LEDs. Since AlGaN has a higher band gap than GaN, polarization field is more enhanced in this case which affects the device performance significantly [279-281]. However, there is no report of systematic study concerning the role of N-polarity in AlGaN based UV LEDs. We aim to investigate the advantages/disadvantages of N-polarity in the case of UV LEDs and accordingly design the structure to have high performance deep UV LEDs.

List of Publications

Refereed and Archival Journal Articles

1. **A. T. Connie**, S. Zhao, S. M. Sadaf, I. Shih, Z. Mi, X. Z. Du, J. Y. Lin, and H. X. Jiang, "On the Magnesium Doping into Aluminum Nitride Nanowires," Appl. Phys. Lett. (submitted).

2. S. Zhao, **A. T. Connie**, M. H. T. Dastjerdi, X. H. Kong, Q. Wang, M. Djavid, S. Sadaf, X. D. Liu, I. Shih, H. Guo, and Z. Mi, "Aluminum Nitride Nanowire Light Emitting Diodes: Breaking the Fundamental Bottleneck of Deep Ultraviolet Light Sources," Sci. Rep., vol. 5, pp. 8332 (2015).

3. R. Wang, H. P. T. Nguyen, **A. T. Connie**, J. Lee, I. Shih, and Z. Mi, "Color-tunable, Phosphor-free InGaN Nanowire Light-Emitting Diode Arrays Monolithically Integrated on Silicon," Opt. Exp., vol. 22, no. S7, pp. A1768-A1775 (2014).

4. S. Zhang, **A. T. Connie**, D. A. Laleyan, H. P. T. Nguyen, Q. Wang, J. Song, I. Shih, and Z. Mi, "On the Carrier Injection Efficiency and Thermal Property of InGaN/GaN Axial Nanowire Light Emitting Diodes," IEEE J. Quan. Elec., vol. 50, no. 6, pp. 483-490 (2014).

5. Q. Wang, S. Zhao, **A. T. Connie**, I. Shih, Z. Mi, T. Gonzalez, M. P. Andrews, X. Z. Du, J. Y. Lin, and H. X. Jiang, "Optical Properties of Strain-free AlN Nanowires Grown by Molecular Beam Epitaxy on Si Substrates," Appl. Phys. Lett., 104, 223107 (2014).

6. **A. T. Connie**, H. P. T. Nguyen, S. M. Sadaf, I. Shih, and Z. Mi, "Engineering the Color Rendering Index of Phosphor-free InGaN/(Al)GaN Nanowire White Light Emitting Diodes Grown by Molecular Beam Epitaxy", J. Vac. Sci. Technol. B, 32, 02C113 (2013).

7. H. P. T. Nguyen, S. Zhang, **A. T. Connie**, Md. Kibria, Q. Wang, I. Shih, and Z. Mi, "Breaking the Carrier Injection Bottleneck of Phosphor-free Nanowire White Light Emitting Diodes", Nano Lett., vol. 13, no. 11, pp. 5437-5442 (2013).

8. Q. Wang, **A. T. Connie**, H. P. T. Nguyen, M. G. Kibria, S. Zhao, S. Sadaf, and Z. Mi, "High Efficiency, Spectrally Pure 340 nm Ultraviolet Emission from $Al_xGa_{1-x}N$

Nanowire Based Light Emitting Diodes", Nanotechnology, vol. 24, no. 34, 345201 (2013).

Conference/Meeting Presentations

1. S. Zhao, **A. T. Connie**, Q. Wang, M. H. T. Dasterjdi, and Z. Mi, "Molecular Beam Epitaxial Growth and Characterization of Superior Quality AlN Nanowires on Si," 18th International Conference on Molecular Beam Epitaxy, Flagstaff, Arizona, USA, Sept. 7-12, 2014.
2. H. P. T. Nguyen, R. Wang, **A. T. Connie**, I. Shih, and Z. Mi, "Color Tunable Phosphor-free InGaN/GaN/AlGaN Core-shell Nanowire White Light-Emitting Diodes on Silicon," 2014 IEEE Summer Topical Meeting on Nanowire Materials and Integrated Photonics, Montreal, QC, Canada, July 14 -16, 2014.
3. S. Zhang, **A. T. Connie**, H. P. T. Nguyen, Q. Wang, I. Shih, and Z. Mi, "Impact of Surface Recombination on the Performance of Phosphor-free InGaN/GaN Nanowire White Light Emitting Diodes," Conference on Lasers and Electro-Optics, San Jose, CA, USA, June 8-13, 2014.
4. **A. T. Connie**, H. P. T. Nguyen, B. H. Le, I. Shih, and Z. Mi, "Investigating the Surface State Effect on Nanowire Solar Cells," Next Generation Solar 2014 – Photovoltaics Canada – Fifth National Scientific Conference, Montreal, QC, Canada, May 14-16, 2014.
5. Z. Mi, H. P. T. Nguyen, **A. T. Connie**, M. G. Kibria, Q. Wang, and I. Shih, "Phosphor-free InGaN/GaN/AlGaN Core-shell Dot-in-a-wire White Light Emitting Diodes," Proc. SPIE, vol. 9003, 900306, 2014.
6. **A. T. Connie**, H. P. T. Nguyen, S. M. Sadaf, I. Shih, and Z. Mi, "Engineering the Color Rendering Index of Phosphor-Free InGaN/(Al)GaN Nanowire White Light Emitting Diodes Grown by Molecular Beam Epitaxy," 30th North American Molecular Beam Epitaxy Conference, Banff, AB, Canada, Oct. 5-11, 2013 (Outstanding Student Paper Award).
7. H. P. T. Nguyen, M. G. Kibria, **A. T. Connie**, Q. Wang, I. Shih, and Z. Mi, "High-Power Phosphor-free InGaN/GaN/AlGaN Dot-in-a-wire Core-shell White Light Emitting

Diodes," 30th North American Molecular Beam Epitaxy Conference, Banff, AB, Canada, Oct. 5-11, 2013.

8. **A. T. Connie**, H. P. T. Nguyen, I. Shih and Z. Mi, "Molecular Beam Epitaxial Growth of InGaN/GaN Nanowire Solar Cells," Next Generation Solar 2013 – Photovoltaics Canada – Fourth National Scientific Conference, Hamilton, ON, Canada, May 8-10, 2013.

Bibliography

[1] M. V. Schilfgaarde, A. Sher, and A.-B. Chen, "Theory of A1N, GaN, InN and their alloys," *J. Crys. Grow.,* vol. 178, pp. 8-31, 1997.

[2] S. Strite and H. Morkoc, "GaN, AIN, and InN: A review," *J. Vac. Sci. Technol. B,* vol. 10, no. 4, pp. 1237-1266, 1992.

[3] M. Farahmand, C. Garetto, E. Bellotti, K. F. Brennan, M. Goano, E. Ghillino, G. Ghione, J. D. Albrecht, P. P. Ruden, "Monte Carlo simulation of electron transport in the III-nitride wurtzite phase materials system: binaries and ternaries," *IEEE Transac. Elec. Dev.,* vol. 48, no. 3, pp. 535-542, 2001.

[4] I. Vurgaftman, J. R. Meyer, and L. R. Ram-Mohan, "Band parameters for III–V compound semiconductors and their alloys," *J. Appl. Phys.,* vol. 89, pp. 5815-5875, 2001.

[5] J. Wu, "When group-III nitrides go infrared: New properties and perspectives," *J. Appl. Phys.,* vol. 106, pp. 011101, 2009.

[6] Z. Yarar, "Transport and mobility properties of wurtzite InN and GaN," P*hys. Stat. Sol. (b),* vol. 244, pp. 3711-3718, 2007.

[7] M. H. Crawford, "LEDs for solid-state lighting: performance challenges and recent advances," *IEEE J. Sel. Topics Quan. Elec.,* vol. 15, pp. 1028-1040, 2009.

[8] M. R. Krames, O. B. Shchekin, R. Mueller-Mach, G. O. Mueller, L. Zhou, G. Harbers, and M. G. Craford, "Status and fFuture of high-power light-emitting diodes for solid-state lighting," *J. Display Technol.,* vol. 3, no. 2, p. 160-175, 2007.

[9] P. T. Barletta, E. Acar Berkman, B. F. Moody, N. A. El-Masry, A. M. Emara, M. J. Reed*, et al.*, "Development of green, yellow, and amber light emitting diodes using InGaN multiple quantum well structures," *Appl. Phys. Lett.,* vol. 90, pp. 151109, 2007.

[10] Y. L. Chang, J. L. Wang, F. Li, and Z. Mi, "High efficiency green, yellow, and amber emission from InGaN/GaN dot-in-a-wire heterostructures on Si(111)," *Appl. Phys. Lett.,* vol. 96, pp. 013106, 2010.

[11] B. Damilano, N. Grandjean, J. Massies, L. Siozade, and J. Leymarie, "InGaN/GaN quantum wells grown by molecular-beam epitaxy emitting from blue to red at 300 K," *Appl. Phys. Lett.,* vol. 77, pp. 1268-1270, 2000.

[12] W. Guo, M. Zhang, A. Banerjee, and P. Bhattacharya, "Catalyst-free InGaN/GaN nanowire light emitting diodes grown on (001) silicon by molecular beam epitaxy," *Nano Lett.,* vol. 10, pp. 3355-3359, 2010.

[13] M. A. Khan, M. Shatalov, H. P. Maruska, H. M. Wang, and E. Kuokstis, "III–Nitride UV Devices," *Jpn. J. Appl. Phys.,* vol. 44, pp. 7191-7206, 2005.

[14] M. Kneissl, T. Kolbe, C. Chua, V. Kueller, N. Lobo, J. Stellmach, A. Knauer, H. Rodriguez, S. Einfeldt, Z. Yang, N. M. Johnson, and M. Weyers, "Advances in group III-nitride-based deep UV light-emitting diode technology," *Semicond. Sci. Technol.,* vol. 26, pp. 014036, 2011.

[15] E. Mu˜noz, E. Monroy, J. L. Pau, F. Calle, F. Omn`es, and P Gibart, "III nitrides and UV detection," *J. Phys: Condens. Mater.,* vol. 13, pp. 7115-7137, 2001.

[16] M. Razeghi and A. Rogalski, "Semiconductor ultraviolet detectors," *J. Appl. Phys.,* vol. 79, no. 10, pp. 7433-7473, 1996.

[17] F. Binet, J. Y. Duboz, E. Rosencher, F. Scholz, and V. Härle, "Mechanisms of recombination in GaN photodetectors," *Appl. Phys. Lett.,* vol. 69, no. 9, p. 1202-1204, 1996.

[18] L. W. Ji, Y. K. Su, S. J. Chang, S. H. Liu, C. K. Wang, S. T. Tsai*, et al.*, "InGaN quantum dot photodetectors," *Solid-State Electron.,* vol. 47, pp. 1753-1756, 2003.

[19] E. Miyazaki, S. Itami, and T. Araki, "Using a light-emitting diode as a high-speed, wavelength selective photodetector," *Rev. Sci. Instrum.,* vol. 69, no. 11, pp. 3751-3754, 1998.

[20] A. Osinsky, S. Gangopadhyay, R. Gaska, B. Williams, M. A. Khan, D. Kuksenkov*, et al.*, "Low noise p-π-n GaN ultraviolet photodetectors," *App. Phys. Lett.,* vol. 71, no. 16, pp. 2334-2336, 1997.

[21] G. E. Weng, A. K. Ling, X. Q. Lv, J. Y. Zhang, and B. P. Zhang, "III-Nitride-based quantum dots and their optoelectronic applications," *Nano-Micro Lett.,* vol. 3, no. 3, pp. 200-207, 2011.

[22] Y. Dong, B. Tian, T. J. Kempa, and C. M. Lieber, "Coaxial Group III-Nitride Nanowire Photovoltaics," *Nano Lett.,* vol. 9, no. 5, pp. 2183-2187, 2009.

[23] O. Jani, I. Ferguson, C. Honsberg, and S. Kurtz, "Design and characterization of GaN/InGaN solar cells," *Appl. Phys. Lett.,* vol. 91, pp. 132117, 2007.

[24] C. J. Neufeld, N. G. Toledo, S. C. Cruz, M. Iza, S. P. DenBaars, and U. K. Mishra, "High quantum efficiency InGaN/GaN solar cells with 2.95 eV band gap," *Appl. Phys. Lett.,* vol. 93, pp. 143502, 2008.

[25] Y. B. Tang, Z. H. Chen, H. S. Song, C. S. Lee, H. T. Cong, H. M. Cheng*, et al.*, "Vertically aligned p-type single-crystalline GaN nanorod arrays on n-type Si for heterojunction photovoltaic cells," *Nano Lett.,* vol. 8, no. 12, pp. 4191-4195, 2008.

[26] X. Zhang, X. Wang, H. Xiao, C. Yang, J. Ran, C. Wang*, et al.*, "Simulation of $In_{0.65}Ga_{0.35}$ N single-junction solar cell," *J. Phys. D: Appl. Phys.,* vol. 40, pp. 7335-7338, 2007.

[27] S. Nakamura, M. Senoh, S.-i. Nagahama, N. Iwasa, T. Yamada, T. Matsushita*, et al.*, "InGaN/GaN/AlGaN-based laser diodes with modulation-doped strained-layer superlattices grown on an epitaxially laterally overgrown GaN substrate," *Appl. Phys. Lett.,* vol. 72, pp. 211-213, 1998.

[28] S. Nakamura, M. Senoh, S.-i. Nagahama, N. Iwasa, T. Yamada, T. Matsushita*, et al.*, "Room-temperature continuous-wave operation of InGaN multi-quantum-well structure laser diodes with a lifetime of 27 hours," *Appl. Phys. Lett.,* vol. 70, pp. 1417-1419, 1997.

[29] Y. Narukawa, Y. Kawakami, M. Funato, S. Fujita, S. Fujita, and S. Nakamura, "Role of self-formed InGaN quantum dots for exciton localization in the purple laser diode emitting at 420 nm," *Appl. Phys. Lett.,* vol. 70, pp. 981-983, 1997.

[30] D. Queren, A. Avramescu, G. Brüderl, A. Breidenassel, M. Schillgalies, S. Lutgen*, et al.*, "500 nm electrically driven InGaN based laser diodes," *Appl. Phys. Lett.,* vol. 94, pp. 081119, 2009.

[31] A. C. T. Palacios, S. Heikman, S. Keller, S. P. DenBaars, and U. K. Mishra, "AlGaN/GaN high electron mobility transistors with InGaN back-barriers," *IEEE Elec. Dev. Lett.,* vol. 27, no. 1, pp. 13-15, 2006.

[32] M. A. Khan, A. Bhattarai, J. N. Kuznia, and D. T. Olson, "High electron mobility transistor based on a GaN-$Al_xGa_{1-x}N$ heterojunction," *Appl. Phys. Lett.,* vol. 63, pp. 1214-1215, 1993.

[33] M. A. Khan, J. N. Kuznia, D. T. Olson, W. J. Schaff, J. W. Burm, and M. S. Shur, "Microwave performance of a 0.25 μm gate AlGaN/GaN heterostructure field effect transistor," *Appl. Phys. Lett.,* vol. 65, pp. 1121-1123, 1994.

[34] P. D. Ye, B. Yang, K. K. Ng, J. Bude, G. D. Wilk, S. Halder*, et al.*, "GaN metal-oxide-semiconductor high-electron-mobility-transistor with atomic layer deposited Al_2O_3 as gate dielectric," *Appl. Phys. Lett.,* vol. 86, pp. 063501, 2005.

[35] Y. Zhang and J. Singh, "Charge control and mobility studies for an AlGaN/GaN high electron mobility transistor," *J. Appl. Phys.,* vol. 85, pp. 587-594, 1999.

[36] S. J. Chang, T. K. Ko, Y. K. Su, Y. Z. Chiou, C. S. Chang, S. C. Shei, J. K. Sheu, W. C. Lai, Y. C. Lin, W. S. Chen, and C. F. Shen, "GaN-Based p-i-n sensors With ITO contacts," *IEEE Sensors. J.,* vol. 6, no. 2, pp. 406-411, 2006.

[37] J. L. Pau, J. Anduaga, C. Rivera, Á. Navarro, I. Álava, M. Redondo, and E. Muñoz, "Optical sensors based on III-nitride photodetectors for flame sensing and combustion monitoring," *Appl. Opt.,* vol. 45, no. 28, pp. 7498-7503, 2006.

[38] D. Chandrasekhar, D. J. Smith, S. Strite, M. E. Lin, and H. Morkoc, "Characterization of Group III-nitride semiconductors by high-resolution electron microscopy " *J. Crys. Grow.,* vol. 152, p. 8, 1995.

[39] M. F. T. Lei, R. J. Molnar, T. D. Moustakas, R. J. Graham, and J. Scanlon "Epitaxial growth of zinc blende and wurtzitic allied nitride thin films on (001) silicon " *Appl. phys. Lett.,* vol. 59, pp. 135-142, 1991.

[40] V. Lebedev, V. Cimalla, U. Kaiser, C. Foerster, J. Pezoldt, J. Biskupek*, et al.*, "Effect of nanoscale surface morphology on the phase stability of 3C-AlN films on Si(111)," *J. Appl. Phys.,* vol. 97, pp. 114306,, 2005.

[41] J. G. Lozano, F. M. Morales, R. García, D. González, V. Lebedev, C. Y. Wang*, et al.*, "Cubic InN growth on sapphire (0001) using cubic indium oxide as buffer layer," *Appl. Phys. Lett.,* vol. 90, pp. 091901, 2007.

[42] T. Schupp, G. Rossbach, P. Schley, R. Goldhahn, M. Röppischer, N. Esser*, et al.*, "MBE growth of cubic AlN on 3C-SiC substrate," *Phys. Stat. Solidi (a),* vol. 207, pp. 1365-1368, 2010.

[43] J. Ibáñez, R. Oliva, F. J. Manjón, A. Segura, T. Yamaguchi, Y. Nanishi*, et al.*, "High-pressure lattice dynamics in wurtzite and rocksalt indium nitride investigated by means of Raman spectroscopy," *Phys. Rev. B,* vol. 88, pp. 115202, 2013.

[44] H. Xia, Q. Xia, and A. Ruoff, "High-pressure structure of gallium nitride: Wurtzite-to-rocksalt phase transition," *Phys. Rev. B,* vol. 47, pp. 12925-12928, 1993.

[45] R. Collazo, S. Mita, A. Aleksov, R. Schlesser, and Z. Sitar, "Growth of Ga- and N- polar gallium nitride layers by metalorganic vapor phase epitaxy on sapphire wafers," *J. Crys. Grow.,* vol. 287, no. 2, pp. 586-590, 2006.

[46] S. Keller, H. Li, M. Laurent, Y. Hu, N. Pfaff, J. Lu, *et al.*, "Recent progress in metal-organic chemical vapor deposition of $\left(000\bar{1} \right)$ N-polar group-III nitrides," *Semicond. Sci. Technol.,* vol. 29, pp. 113001, 2014.
[47] *www.wikipedia.com*.
[48] M. S. Dresselhaus, Y. M. Lin, O. Rabin, M.R. Black, and G. Dresselhaus. "Nanowires," 2003 (http://mgm.mit.edu/group/x986.pdf).
[49] T. Egawa and B. A. B. A. Shuhaimi, "High performance InGaN LEDs on Si (1 1 1) substrates grown by MOCVD," *J. Phys. D: Appl. Phys.,* vol. 43, pp. 354008 2010.
[50] C. D. Lee, V. Ramachandran, A. Sagar, R. M. Feenstra, D. W. Greve, W. L. Sarney, L. Salamanca-Riba, D. C. Look, S. Bai, W. J. Choyke, and R. P. Devaty, "Properties of GaN epitaxial layers grown on 6HSiC(0001) by plasma-assisted molecular beam epitaxy," *J. Elec. Mater.,* vol. 30, no. 3, pp. 162-169, 2001.
[51] M. Haeberlen, D. Zhu, C. McAleese, M. J. Kappers, and C. J. Humphreys, "Dislocation reduction in MOVPE grown GaN layers on (111) Si using SiN_x and AlGaN layers," *J. Phys.: Conf. Ser.,* vol. 209, pp. 012017, 2010.
[52] H.-Y. Shin, S. K. Kwon, Y. I. Chang, M. J. Cho, and K. H. Park, "Reducing dislocation density in GaN films using a cone-shaped patterned sapphire substrate," *J. Crys. Grow.,* vol. 311, pp. 4167-4170, 2009.
[53] F. Glas, "Critical dimensions for the plastic relaxation of strained axial heterostructures in free-standing nanowires," *Phys. Rev. B,* vol. 74, pp. 121302*,* 2006.
[54] D. Eaglesham and M. Cerullo, "Dislocation-free Stranski-Krastanow growth of Ge on Si(100)," *Phys. Rev. Lett.,* vol. 64, no. 16, pp. 1943-1946, 1990.
[55] D. W. Palmer, "Properties of III-nitride semiconductors," http://www.semiconductors.co.uk.
[56] S. Strite and H. Morkoc, "GaN, AIN, and InN: A review " *J. Vac. Sci. Technol. B,* vol. 10, no. 4, pp. 1237-1266, 1992.
[57] D. Zhu, D. J. Wallis, and C. J. Humphreys, "Prospects of III-nitride optoelectronics grown on Si," *Rep. Prog. Phys.,* vol. 76, no. 10, pp. 106501, 2013.
[58] M. Boroditsky, T. F. Krauss, R. Coccioli, R. Vrijen, R. Bhat, and E. Yablonovitch, "Light extraction from optically pumped light-emitting diode by thin-slab photonic crystals," *Appl. Phys. Lett.,* vol. 75, no. 8, pp. 1036-1038, 1999.
[59] E. E. Loebner, "The future of electroluminescent solids in display application," *Proc. of IEEE,* vol. 61, no. 7, pp. 837-861, 1973.
[60] W. N. Carr and G. E. Pittman, " One-Watt GaAs *p-n* junction infrared source," *Appl. Phys. Lett.,* vol. 3, no. 10, pp. 173-175, 1963.
[61] A. R. Franklin and R. Newman, "Shaped electroluminescent GaAs diodes," *Appl. Phys.,* vol. 35, no. 4, pp. 1153-1155,, 1964.
[62] J. J. Wierer, A. David, and M. M. Megens, "III-nitride photonic-crystal light-emitting diodes with high extraction efficiency," *Nature Photon.,* vol. 3, pp. 163-169, 2009.
[63] D. Ko, J. Yoon, and J. Seo, "Patterned substrates enhance LED light extraction," *LEDs Magazine*, 2014.

[64] H. Benisty, H. De Neve, and C. Weisbuch, "Impact of planar microcavity effects on light extraction—Part I: basic concepts and analytical trends," *IEEE J. Quan. Elec.,* vol. 34, pp. 1612-1631, 1998.
[65] H. Benisty, H. De Neve, and C. Weisbuch, "Impact of planar microcavity effects on light extraction—Part I: basic concepts and analytical trends," *IEEE J. Quan. Elec.,* vol. 34, pp. 1632-1643, 1998.
[66] E. F. Schubert, N. E. J. Hunt, M. Micovic, R. J. Malik, D. L. Sivco, A. Y. Cho, *et al.*, "Highly efficient light-emitting diodes with microcavities," *Science,* vol. 265, no. 5174, pp. 943-945, 1994.
[67] S. Fan, P. R. Villeneuve, and J. D. Joannopoulos, "High extraction efficiency of spontaneous emission from slabs of photonic crystals," *Phys. Rev. Lett.,* vol. 78, no. 17, pp. 3294-3297, 1997.
[68] E. Yablonovitch, "Inhibited spontaneous emission in solid state physics and electronics," *Phys. Rev. Lett.,* vol. 58, no. 20, pp. 2059-2062, 1987.
[69] M. Fujita, S. Takahashi, Y. Tanaka, T. Asano, and S. Noda, "Simultaneous inhibition and redistribution of spontaneous light emission in photonic crystals," *Science,* vol. 308, pp. pp. 1296-1298, 2005.
[70] A-L. Henneghien, G. Tourbot, B. Daudin, O. Lartigue, Y. D´esi`eres, and J-M. G´erard, "Optical anisotropy and light extraction efficiency of MBE grown GaN nanowires epilayers," *Opt. Exp.,* vol. 19, no. 2, pp. 527-539, 2011.
[71] A-L. Henneghien, B. Gayral, Y. Désières, and J-M. Gérard, "Simulation of waveguiding and emitting properties of semiconductor nanowires with hexagonal or circular sections " *J. Opt. Soc. Am. B,* vol. 26, no. 2, pp. 2396-2403, 2009.
[72] M. H. Mustary and V. V. Lysak,, "Fabrication of nanorod light emitting diode by Ni nano-clusters and enhanced light extraction efficiency," *IOSR-JEEE,* vol. 9, no. 4, pp. 18-22, 2014.
[73] J. Wenjing, X. Chen, S. Guangdi, F. Rong, and G. Wei, "Improved light extraction in AlGaInP-based LEDs using a self-assembly metal nanomask," *J. Semicond.,* vol. 31, no. 6, pp. 064008, 2010.
[74] M. L. Kuo, Y. S. Kim, M. L. Hsieh, and S. Y. Lin, "Efficient and directed Nano-LED emission by a complete elimination of transverse-electric guided modes," *Nano Lett.,* vol. 11, no. 2, pp. 476-481, 2011.
[75] A. Armstrong, Q. Li, Y. Lin, A. A. Talin, and G. T. Wang, "GaN nanowire surface state observed using deep level optical spectroscopy," *Appl Phys. Lett.,* vol. 96, pp. 163106, 2010.
[76] M. Bertelli, P. Löptien, M. Wenderoth, A. Rizzi, R. Ulbrich, M. Righi*, et al.*, "Atomic and electronic structure of the nonpolar GaN(11¯00) surface," *Phys. Rev. B,* vol. 80, pp. 115324, 2009.
[77] C. G. Van de Walle and D. Segev, "Microscopic origins of surface states on nitride surfaces," *J. Appl. Phys.,* vol. 101, no. 8, pp. 081704, 2007.
[78] C-H. Chang, L-Y. Chen, L.-Y. C. C-H. Chang, L-C. Huang, Y-T. Wang, T-C. Lu, and J. J. Huang, "Effects of strains and defects on the internal quantum efficiency of InGaN/GaN nanorod light emitting diodes," *IEEE J. Quan. Elec.,* vol. 48, no. 4, pp. 551-556, 2012.

[79] H. P. Nguyen, M. Djavid, K. Cui, and Z. Mi, "Temperature-dependent nonradiative recombination processes in GaN-based nanowire white-light-emitting diodes on silicon," *Nanotechnology,* vol. 23, no. 19, pp. 194012, 2012.
[80] M. G. Kibria, S. Zhao, F. A. Chowdhury, Q. Wang, H. P. Nguyen, M. L. Trudeau*, et al.*, "Tuning the surface Fermi level on p-type gallium nitride nanowires for efficient overall water splitting," *Nat Commun,* vol. 5, pp. 3825, 2014.
[81] Q. Wang, X. Liu, M. G. Kibria, S. Zhao, H. P. Nguyen, K. H. Li*, et al.*, "p-Type dopant incorporation and surface charge properties of catalyst-free GaN nanowires revealed by micro-Raman scattering and X-ray photoelectron spectroscopy," *Nanoscale,* vol. 6, pp. 9970-9976, 2014.
[82] B. S. Simpkins, M. A. Mastro, C. R. Eddy, and P. E. Pehrsson, "Surface depletion effects in semiconducting nanowires," *J. Appl. Phys.,* vol. 103, pp. 104313, 2008.
[83] R. Calarco, M. Marso, T. Richter, A. I. Aykanat, R. Meijers, A. V. D. Hart, T. Stoica, and H. Luth, "Size-dependent Photoconductivity in MBE-Grown GaN-Nanowires," *Nano Lett.,* vol. 5, no. 5, pp. 981-984, 2005.
[84] N. A. Sanford, P. T. Blanchard, K. A. Bertness, L. Mansfield, J. B. Schlager, A. W. Sanders*, et al.*, "Steady-state and transient photoconductivity in c-axis GaN nanowires grown by nitrogen-plasma-assisted molecular beam epitaxy," *J. Appl. Phys.,* vol. 107, pp. 034318, 2010.
[85] V. Schmidt, S. Senz, and U. Gösele, "Influence of the Si/SiO2 interface on the charge carrier density of Si nanowires," *Appl. Phys. A,* vol. 86, pp. 187-191, 2006.
[86] E. F. Schubert and J. K. Kim, "Solid-state light sources getting smart," *Science,* vol. 308, pp. 1274-1278, 2005.
[87] Q. Dai, Q. Shan, J. Wang, S. Chhajed, J. Cho, E. F. Schubert*, et al.*, "Carrier recombination mechanisms and efficiency droop in GaInN/GaN light-emitting diodes," *Appl. Phys. Lett.,* vol. 97, pp. 133507, 2010.
[88] H.-Y. Ryu, H.-S. Kim, and J.-I. Shim, "Rate equation analysis of efficiency droop in InGaN light-emitting diodes," *Appl. Phys. Lett.,* vol. 95, pp. 081114, 2009.
[89] S. Chichibu, T. Azuhata, T. Sota, and S. Nakamura, "Luminescences from localized states in InGaN epilayers," *Appl. Phys. Lett.,* vol. 70, pp. 2822-2824, 1997.
[90] Y.-L. Lai, C.-P. Liu, Y.-H. Lin, T.-H. Hsueh, R.-M. Lin, D.-Y. Lyu*, et al.*, "Origins of efficient green light emission in phase-separated InGaN quantum wells," *Nanotechnology,* vol. 17, pp. 3734-3739, 2006.
[91] B. Monemar and B. E. Sernelius, "Defect related issues in the "current roll-off" in InGaN based light emitting diodes," *Appl. Phys. Lett.,* vol. 91, pp. 181103, 2007.
[92] X. Ni, Q. Fan, R. Shimada, U. m. Özgür, and H. Morkoç, "Reduction of efficiency droop in InGaN light emitting diodes by coupled quantum wells," *Appl. Phys. Lett.,* vol. 93, pp. 171113, 2008.
[93] S.-H. Y. M-C. Tsai, Y-C. Lu, and Y-K. Kuo, "Numerical Study of Blue InGaN Light-Emitting Diodes With Varied Barrier Thicknesses," *IEEE Photon. Technon. Lett.,* vol. 23, pp. 76-78, 2011.
[94] E. Kioupakis, P. Rinke, K. T. Delaney, and C. G. Van de Walle, "Indirect Auger recombination as a cause of efficiency droop in nitride light-emitting diodes," *Appl. Phys. Lett.,* vol. 98, pp. 161107, 2011.

[95] E. Kioupakis, P. Rinke, A. Schleife, F. Bechstedt, and C. G. Van de Walle, "Free-carrier absorption in nitrides from first principles," *Phys. Rev. B,* vol. 81, pp. 241201, 2010.
[96] A. Laubsch, M. Sabathil, J. Baur, M. Peter, and B. Hahn, "High-Power and High-Efficiency InGaN-Based Light Emitters," *IEEE Transac. Elec. Dev.,* vol. 57, pp. 79-87, 2010.
[97] M. Meneghini, N. Trivellin, G. Meneghesso, E. Zanoni, U. Zehnder, and B. Hahn, "A combined electro-optical method for the determination of the recombination parameters in InGaN-based light-emitting diodes," *J. Appl. Phys.,* vol. 106, pp. 114508, 2009.
[98] M. Zhang, P. Bhattacharya, J. Singh, and J. Hinckley, "Direct measurement of auger recombination in In[sub 0.1]Ga[sub 0.9]N/GaN quantum wells and its impact on the efficiency of $In_{0.1}Ga_{0.9}N$/GaN multiple quantum well light emitting diodes," *Appl. Phys. Lett.,* vol. 95, pp. 201108, 2009.
[99] J. Piprek and S. Li, "Electron leakage effects on GaN-based light-emitting diodes," *Opt. Quan. Elec.,* vol. 42, pp. 89-95, 2011.
[100] A. Kikuchi, M. Kawai, M. Tada, and K. Kishino, "InGaN/GaN multiple quantum disk nanocolumn light-emitting diodes grown on (111) Si substrate," *Jpn. J. Appl. Phys.,* vol. 43, pp. L1524, 2004.
[101] A. Kikuchi, M. Tada, K. Miwa, and K. Kishino, "Growth and characterization of InGaN/GaN nanocolumn LED," *Proc. SPIE 6129,* 2006.
[102] A. L. Bavencove, G. Tourbot, E. Pougeoise, J. Garcia, P. Gilet, F. Levy*, et al.*, "GaN-based nanowires: From nanometric-scale characterization to light emitting diodes," P*hys. Stat. Solidi (a),* vol. 207, pp. 1425-1427, 2010.
[103] W. Guo, M. Zhang, P. Bhattacharya, and J. Heo, "Auger recombination in III-nitride nanowires and its effect on nanowire light-emitting diode characteristics," *Nano Lett.,* vol. 11, pp. 1434-1438, 2011.
[104] S. D. Hersee, M. Fairchild, A. K. Rishinaramangalam, M. S. Ferdous, L. Zhang, P. M. Varangis*, et al.*, "GaN nanowire light emitting diodes based on templated and scalable nanowire growth process," *Electron. Lett.,* vol. 45, no. 1, pp. 75, 2009.
[105] H-M. Kim, Y-H. Choo, H. Lee, S. I. Kim, S. R. Ryu, D. Y. Kim, T. W. Kang, and K. S. Chung, "High-brightness light emitting diodes using dislocation-free Indium Gallium Nitride/Gallium Nitride multiquantum-well nanorod arrays," *Nano Lett.,* vol. 4, no. 6, pp. 1059-1062, 2004.
[106] G. Kunert, W. Freund, T. Aschenbrenner, C. Kruse, S. Figge, M. Schowalter*, et al.*, "Light-emitting diode based on mask- and catalyst-free grown N-polar GaN nanorods," *Nanotechnology,* vol. 22, pp. 265202, 2011.
[107] H.-W. Lin, Y.-J. Lu, H.-Y. Chen, H.-M. Lee, and S. Gwo, "InGaN/GaN nanorod array white light-emitting diode," *Appl. Phys. Lett.,* vol. 97, pp. 073101, 2010.
[108] M. Zhang, W. Guo, A. Banerjee, and Pallab Bhattacharya, "InGaN/GaN nanowire green light emitting diodes on (001) Si substrates," Dev. Res. Conf., pp. 229-230, 2010.
[109] H. P. T. Nguyen, K. Cui, S. Zhang, M. Djavid, A. Korinek, G. A. Botton*, et al.*, "Controlling electron overflow in phosphor-free InGaN/GaN nanowire white light-emitting diodes," *Nano Lett.,* vol. 12, pp. 1317-1323, 2012.

[110] H. P. T. Nguyen, S. Zhang, K. Cui, X. Han, S. Fathololoumi, M. Couillard*, et al.*, "p-Type modulation doped InGaN/GaN dot-in-a-wire white-light-emitting diodes monolithically grown on Si(111)," *Nano Lett.,* vol. 11, pp. 1919-1924, 2011.
[111] R. Halliday, "Key Benefits of Next-Gen UV LED Technology," http://www.lumex.com/en/tech-notes/article/key_benefits_of_next-gen_uv-led_tech/.
[112] "Next Generation UV LED Technology Benefits Industrial Curing, Coating," P. E. Editors, http://www.digikey.ca/en/articles/techzone/2012/aug/next-generation-uv-led-technology-benefits-industrial-curing-coating, 2012.
[113] "The UV LED market is booming," http://electroiq.com/blog/2013/03/the-uv-led-market-is-booming/, 2014.
[114] S. Kamiyama, M. Iwaya, N. Hayashi, T. Takeuchi, H. Amano, I. Akasaki, S. Watanabe, Y. Kaneko, N. Yamada, "Low-temperature-deposited AlGaN interlayer for improvement of AlGaN/GaN heterostructure," *J. Crys. Grow.,* vol. 223, pp. 83-91, 2001.
[115] J. Han, K. E. Waldrip, S. R. Lee, J. J. Figiel, S. J. Hearne, G. A. Petersen*, et al.*, "Control and elimination of cracking of AlGaN using low-temperature AlGaN interlayers," *Appl. Phys. Lett.,* vol. 78, pp. 67, 2001.
[116] K. Hiramatsu, "Epitaxial lateral overgrowth techniques used in group III nitride epitaxy," *J. Phys: Condens. Matter.,* vol. 13, pp. 15, 2001.
[117] Z. R. Zytkiewicz, "Laterally overgrown structures as substrates for lattice mismatched epitaxy," *Thin Solid Films,* vol. 412, pp. 12, 2002.
[118] O.-H. Nam, M. D. Bremser, T. S. Zheleva, and R. F. Davis, "Lateral epitaxy of low defect density GaN layers via organometallic vapor phase epitaxy," *Appl. Phys. Lett.,* vol. 71, pp. 2638-2640, 1997.
[119] M. A. Khan, J. N. Kuznia, D. T. Olson, T. George, and W. T. Pike, "GaN/AlN digital alloy short-period superlattices by switched atomic layer metalorganic chemical vapor deposition," *Appl. Phys. Lett.,* vol. 63, pp. 3470-3472, 1993.
[120] M. A. Khan, J. N. Kuznia, R. A. Skogman, D. T. Olson, M. Mac Millan, and W. J. Choyke, "Low pressure metalorganic chemical vapor deposition of AIN over sapphire substrates," *Appl. Phys. Lett.,* vol. 61, pp. 2539, 1992.
[121] M. A. Khan, R. A. Skogman, J. M. Van Hove, D. T. Olson, and J. N. Kuznia, "Atomic layer epitaxy of GaN over sapphire using switched metalorganic chemical vapor deposition," *Appl. Phys. Lett.,* vol. 60, no. 11, pp. 1366-1368, 1992.
[122] V. Kueller, A. Knauer, C. Reich, A. Mogilatenko, M. Weyers, J. Stellmach, T. Wernicke, M. Kneissl, Z. Yang, C. L. Chua, and N. M. Johnson, "Modulated epitaxial lateral overgrowth of AlN for efficient UV LEDs," *IEEE Photon. Technon. Lett.,* vol. 24, no. 18, pp. 1603-1605, 2012.
[123] R. Gaska, C. Chen, J. Yang, E. Kuokstis, A. Khan, G. Tamulaitis*, et al.*, "Deep-ultraviolet emission of AlGaN/AlN quantum wells on bulk AlN," *Appl. Phys. Lett.,* vol. 81, no. 24, pp. 4658-4660, 2002.
[124] J. C. Rojo, L. J. Schowalter,, R. Gaska, M. Shur, M.A. Khan, J. Yang, D. D. Koleske, "Growth and characterization of epitaxial layers on aluminum nitride substrates prepared frombulk, single crystals," *J. Crys. Grow.,* vol. 240, pp. 508-512, 2002.

[125] T. Nishida, T. Makimoto, H. Saito, and T. Ban, "AlGaN-based ultraviolet light-emitting diodes grown on bulk AlN substrates," *Appl. Phys. Lett.,* vol. 84, no. 6, pp. 1002-1003, 2004.
[126] Z. Ren, Q. Sun, S. Y. Kwon, J. Han, K. Davitt, Y. K. Song*, et al.*, "Heteroepitaxy of AlGaN on bulk AlN substrates for deep ultraviolet light emitting diodes," *Appl. Phys. Lett.,* vol. 91, pp. 051116, 2007.
[127] E. Silveira, J. A. Freitas, M. Kneissl, D. W. Treat, N. M. Johnson, G. A. Slack*, et al.*, "Near-bandedge cathodoluminescence of an AlN homoepitaxial film," *Appl. Phys. Lett.,* vol. 84, no. 18, pp. 3501-3503, 2004.
[128] T. Kinoshita, T. Obata, T. Nagashima, H. Yanagi, B. Moody, S. Mita, S-I Inoue, Y. Kumagai, A. Koukitu, and Z. Sitar, "Performance and reliability of deep-ultraviolet light-emitting diodes fabricated on AlN substrates prepared by hydride vapor phase epitaxy," *Appl. Phys. Exp.,* vol. 6, pp. 092103, 2013.
[129] T. Kinoshita, K. Hironaka, T. Obata, T. Nagashima, R. Dalmau, R. Schlesser, B. Moody, J. Xie, S-I. Inoue, Y. Kumagai, A. Koukitu, Z. Sitar, "Deep-ultraviolet light-emitting diodes fabricated on AlN substrates prepared by hydride vapor phase epitaxy," *Appl. Phys. Exp.,* vol. 5, pp. 122101, 2012.
[130] M. L. Nakarmi, N. Nepal, J. Y. Lin, and H. X. Jiang, "Photoluminescence studies of impurity transitions in Mg-doped AlGaN alloys," *Appl. Phys. Lett.,* vol. 94, pp. 091903, 2009.
[131] J. Simon, V. Protasenko, C. Lian, H. Xing, and D. Jena, "Polarization-induced hole doping in wide-band-gap uniaxial semiconductor heterostructures," *Science,* vol. 327, pp. 60-64, 2010.
[132] L. Zhang, K. Ding, N. X. Liu, T. B. Wei, X. L. Ji, P. Ma*, et al.*, "Theoretical study of polarization-doped GaN-based light-emitting diodes," *Appl. Phys. Lett.,* vol. 98, pp. 101110, 2011.
[133] S. Krishnamoorthy, F. Akyol, P. S. Park, and S. Rajan, "Low resistance GaN/InGaN/GaN tunnel junctions," *Appl. Phys. Lett.,* vol. 102, pp. 113503, 2013.
[134] S. Krishnamoorthy, D. N. Nath, F. Akyol, P. S. Park, M. Esposto, and S. Rajan, "Polarization-engineered GaN/InGaN/GaN tunnel diodes," *Appl. Phys. Lett.,* vol. 97, pp. 203502, 2010.
[135] M. L. Nakarmi, K. H. Kim, J. Li, J. Y. Lin, and H. X. Jiang, "Enhanced p-type conduction in GaN and AlGaN by Mg-δ-doping," *Appl. Phys. Lett.,* vol. 82, no. 18, pp. 3041-3043, 2003.
[136] J. Li, K. B. Nam, M. L. Nakarmi, J. Y. Lin, H. X. Jiang, P. Carrier*, et al.*, "Band structure and fundamental optical transitions in wurtzite AlN," *Appl. Phys. Lett.,* vol. 83, no. 25, pp. 5163-5165, 2003.
[137] K. B. Nam, J. Li, M. L. Nakarmi, J. Y. Lin, and H. X. Jiang, "Unique optical properties of AlGaN alloys and related ultraviolet emitters," *Appl. Phys. Lett.,* vol. 84, no. 25, pp. 5264-5266, 2004.
[138] R. Banal, M. Funato, and Y. Kawakami, "Optical anisotropy in [0001]-oriented $Al_xGa_{1-x}N$/AlN quantum wells ($x > 0.69$)," *Phys. Rev. B,* vol. 79, pp. 121308, 2009.
[139] H. Kawanishi, M. Senuma, and T. Nukui, "Anisotropic polarization characteristics of lasing and spontaneous surface and edge emissions from deep-

ultraviolet (λ≈240 nm) AlGaN multiple-quantum-well lasers," *Appl. Phys. Lett.,* vol. 89, pp. 041126, 2006.

[140] H. Kawanishi, M. Senuma, M. Yamamoto, E. Niikura, and T. Nukui, "Extremely weak surface emission from (0001) c-plane AlGaN multiple quantum well structure in deep-ultraviolet spectral region," *Appl. Phys. Lett.,* vol. 89, pp. 081121, 2006.

[141] T. Kolbe, A. Knauer, C. Chua, Z. Yang, S. Einfeldt, P. Vogt*, et al.*, "Optical polarization characteristics of ultraviolet (In)(Al)GaN multiple quantum well light emitting diodes," *Appl. Phys. Lett.,* vol. 97, pp. 171105, 2010.

[142] J. E. Northrup, C. L. Chua, Z. Yang, T. Wunderer, M. Kneissl, N. M. Johnson*, et al.*, "Effect of strain and barrier composition on the polarization of light emission from AlGaN/AlN quantum wells," *Appl. Phys. Lett.,* vol. 100, pp. 021101, 2012.

[143] V. Adivarahan, W. H. Sun, A. Chitnis, M. Shatalov, S. Wu, H. P. Maruska*, et al.*, "250 nm AlGaN light-emitting diodes," *Appl. Phys. Lett.,* vol. 85, no. 12, pp. 2175-2177, 2004.

[144] K. X. Chen, Q. Dai, W. Lee, J. K. Kim, E. F. Schubert, W. Liu*, et al.*, "Parasitic sub-band-gap emission originating from compensating native defects in Si doped AlGaN," *Appl. Phys. Lett.,* vol. 91, pp. 121110, 2007.

[145] K. X. Chen, Y. A. Xi, F. W. Mont, J. K. Kim, E. F. Schubert, W. Liu*, et al.*, "Recombination dynamics in ultraviolet light-emitting diodes with Si-doped $Al_xGa_{1-x}N/Al_yGa_{1-y}N$ multiple quantum well active regions," *J. Appl. Phys.,* vol. 101, pp. 113102, 2007.

[146] K. B. Nam, M. L. Nakarmi, J. Li, J. Y. Lin, and H. X. Jiang, "Mg acceptor level in AlN probed by deep ultraviolet photoluminescence," *Appl. Phys. Lett.,* vol. 83, no. 5, pp. 878-880, 2003.

[147] M. L. Nakarmi, N. Nepal, C. Ugolini, T. M. Altahtamouni, J. Y. Lin, and H. X. Jiang, "Correlation between optical and electrical properties of Mg-doped AlN epilayers," *Appl. Phys. Lett.,* vol. 89, pp. 152120, 2006.

[148] A. Pierret, C. Bougerol, B. Gayral, M. Kociak, and B. Daudin, "Probing alloy composition gradient and nanometer-scale carrier localization in single AlGaN nanowires by nanocathodoluminescence," *Nanotechnology,* vol. 24, pp. 305703, 2013.

[149] A. Pierret, C. Bougerol, M. d. Hertog, B. Gayral, M. Kociak, H. Renevier*, et al.*, "Structural and optical properties of AlxGa1-xN nanowires," *Phys. Stat. Solidi - Rapid Res. Lett.,* vol. 7, pp. 868-873, 2013.

[150] A. Pierret, C. Bougerol, S. Murcia-Mascaros, A. Cros, H. Renevier, B. Gayral*, et al.*, "Growth, structural and optical properties of AlGaN nanowires in the whole composition range," *Nanotechnology,* vol. 24, pp. 115704, 2013.

[151] J. Zhang, X. S. Peng, X. F. Wang, Y. W. Wang, and L. D. Zhang "Micro-Raman Investigation of GaN Nanowires Prepared by Direct Reaction Ga with NH_3," *Chem. Phys. Lett.,* vol. 345, no. 5-6, pp. 372-376, 2001.

[152] Q. Li, K. R. Westlake, M. H. Crawford, S. R. Lee, D. D. Koleske, J. J. Figiel, K. C. Cross, S. Fathololoumi, Z. Mi, and G. T. Wang, "Optical performance of top-down fabricated InGaN/GaN nanorod light emitting diode arrays," *Opt. Exp.,* vol. 19, no. 25, pp. 25528-25534, 2011.

[153] M. Kuball, F. H. Morrissey, M. Benyoucef, I. Harrison, D. Korakakis, and C. T. Foxon, "Nano-fabrication of GaN pillars using focused ion meam etching," *Phys. Stat. Solidi A,* vol. 176, no. 1, pp. 355-358, 1999.

[154] S.-Y. Park, S. J. Di Giacomo, R. Anisha, P. R. Berger, P. E. Thompson, and I. Adesida, "Fabrication of nanowires with high aspect ratios utilized by dry etching with SF_6:C_4F_8 and self-limiting thermal oxidation on Si substrate," *J. Vac. Sci. Technol. B: Microelectron. Nanometer Struc.,* vol. 28, pp. 763, 2010.

[155] R. S. Wagner and W. C. Ellis, "Vapor-liquid-solid mechanism of single crystal growth," *Appl. Phys. Lett.,* vol. 4, pp. 89, 1964.

[156] H. Sekiguchi, K. Kishino, and A. Kikuchi, "Ti-mask selective-area growth of GaN by RF-plasma-assisted molecular-beam epitaxy for fabricating regularly arranged InGaN/GaN nanocolumns," *Appl. Phys. Exp.,* vol. 1, pp. 124002, 2008.

[157] K. Kishino, H. Sekiguchi, and A. Kikuchi, "Improved Ti-mask selective-area growth (SAG) by rf-plasma-assisted molecular beam epitaxy demonstrating extremely uniform GaN nanocolumn arrays," *J. Crys. Grow.,* vol. 311, pp. 2063-2068, 2009.

[158] T. Schumann, T. Gotschke, F. Limbach, T. Stoica, and R. Calarco, "Selective-area catalyst-free MBE growth of GaN nanowires using a patterned oxide layer," *Nanotechnology,* vol. 22, pp. 095603, 2011.

[159] J. Ristić, E. Calleja, S. Fernández-Garrido, L. Cerutti, A. Trampert, U. Jahn*, et al.*, "On the mechanisms of spontaneous growth of III-nitride nanocolumns by plasma-assisted molecular beam epitaxy," *J. Crys. Grow.,* vol. 310, pp. 4035-4045, 2008.

[160] A. P. Vajpeyi, A. O. Ajagunna, G. Tsiakatouras, A. Adikimenakis, E. Iliopoulos, K. Tsagaraki*, et al.*, "Spontaneous growth of III-nitride nanowires on Si by molecular beam epitaxy," *Microelectron. Eng.,* vol. 86, pp. 812-815, 2009.

[161] T. Stoica, R. Meijers, R. Calarco, T. Richter, and H. Lüth, "MBE growth optimization of InN nanowires," *J. Crys. Grow.,* vol. 290, pp. 241-247, 2006.

[162] K. A. Bertness, A. Roshko, N. A. Sanford, J. M. Barker, and A. V. Davydov, "Spontaneously grown GaN and AlGaN nanowires," *J. Crys. Grow.,* vol. 287, pp. 522-527, 2006.

[163] K. Vampola, "Improvement of III-N visible and ultraviolet light-emitting diode performance, including extraction efficiency, electrical efficiency, thermal management and efficiency maintenance at high current densities " Ph. D, Materials Engineering, University of California (Santa Barbara), 2009.

[164] I. Pelant and J. Valenta, "Luminescence Spectroscopy of Semiconductors," Oxford University Press, 2012.

[165] L. Zhang, K. Cheng, S. Degroote, M. Leys, M. Germain, and G. Borghs, "Strain effects in GaN epilayers grown on different substrates by metal organic vapor phase epitaxy," *J. Appl. Phys.,* vol. 108, pp. 073522, 2010.

[166] C. Netzel, V. Hoffmann, T. Wernicke, A. Knauer, M. Weyers, M. Kneissl*, et al.*, "Temperature and excitation power dependent photoluminescence intensity of GaInN quantum wells with varying charge carrier wave function overlap," *J. Appl. Phys.,* vol. 107, pp. 033510,, 2010.

[167] S. Watanabe, N. Yamada, M. Nagashima, Y. Ueki, C. Sasaki, Y. Yamada*, et al.*, "Internal quantum efficiency of highly-efficient $In_xGa_{1-x}N$-based near-ultraviolet light-emitting diodes," *Appl. Phys. Lett.,* vol. 83, pp. 4906, 2003.
[168] Y-J. Lee, C-H., Chiu, C. C. Ke, P. C. Lin, T-C. Lu, H-C. Kuo, and S-C. Wang, "Study of the excitation power dependent internal quantum efficiency in InGaN/GaN LEDs grown on patterned sapphire substrate," *IEEE J. Sel. Topics Quan. Elec.,* vol. 15, no. 4, pp. 1137 - 1143, 2009.
[169] W. Davis, "Color Rendering of Light Sources," *Article Library,* 2011.
[170] F. Qian, Y. Li, S. Gradec˘ak, D. Wang, C. J. Barrelet, and C. M. Lieber, "Gallium Nitride-based nanowire radial heterostructures for nanophotonics," *Nano Lett.,* vol. 4, no. 10, pp. 1975–1979, 2004.
[171] M.-H. Kim, M. F. Schubert, Q. Dai, J. K. Kim, E. F. Schubert, J. Piprek*, et al.*, "Origin of efficiency droop in GaN-based light-emitting diodes," *Appl. Phys. Lett.,* vol. 91, pp. 183507, 2007.
[172] T. Kuykendall, P. Ulrich, S. Aloni, and P. Yang, "Complete composition tunability of InGaN nanowires using a combinatorial approach," *Nat. Mater.,* vol. 6, pp. 951-956, 2007.
[173] H. Masui, J. Sonoda, N. Pfaff, I. Koslow, S. Nakamura, and S. P. DenBaars, "Quantum-confined Stark effect on photoluminescence and electroluminescence characteristics of InGaN-based light-emitting diodes," *J. Phys. D: Appl. Phys.,* vol. 41, pp. 165105, 2008.
[174] A. Kikuchi, M. Kawai, M. Tada, and K. Kishino, "InGaN/GaN multiple quantum disk nanocolumn light-emitting diodes grown on (111) Si substrate," *Jpn. J. Appl. Phys.,* vol. 43, pp. L1524-L1526, 2004.
[175] K. G. Eyink, A. Kikuchi, M. Tada, K. Miwa, K. Kishino, and D. L. Huffaker, "Growth and characterization of InGaN/GaN nanocolumn LED," vol. 6129, pp. 612905-612905-8, 2006.
[176] I. V. Rozhansky and D. A. Zakheim, "Analysis of the causes of the decrease in the electroluminescence efficiency of AlGaInN light-emitting-diode heterostructures at high pumping density," *Semicond.,* vol. 40, pp. 839-845, 2006.
[177] J. Xie, X. Ni, Q. Fan, R. Shimada, U. m. Özgür, and H. Morkoç, "On the efficiency droop in InGaN multiple quantum well blue light emitting diodes and its reduction with p-doped quantum well barriers," *Appl. Phys. Lett.,* vol. 93, pp. 121107, 2008.
[178] A. Waag, X. Wang, S. Fündling, J. Ledig, M. Erenburg, R. Neumann*, et al.*, "The nanorod approach: GaN NanoLEDs for solid state lighting," P*hys. Stat. Solidi (c),* vol. 8, pp. 2296-2301, 2011.
[179] A. L. Bavencove, G. Tourbot, J. Garcia, Y. Desieres, P. Gilet, F. Levy*, et al.*, "Submicrometre resolved optical characterization of green nanowire-based light emitting diodes," *Nanotechnology,* vol. 22, pp. 345705, 2011.
[180] M. Boroditsky, I. Gontijo, M. Jackson, R. Vrijen, and E. Yablonovitch, "Surface recombination measurements on III–V candidate materials for nanostructure light-emitting diodes," *J. Appl. Phys.,* vol. 87, no. 7, pp. 3497-3504, 2000.
[181] Y.-J. Lin, W.-X. Lin, C.-T. Lee, and F.-T. Chien, "Changes in optical and electrical properties and surface recombination velocity of n-type GaN due to $(NH_4)_2S_x$ treatment," *Solid State Commun.,* vol. 137, pp. 257-259, 2006.

[182] A. A. Setlur, E. V. Radkov, C. S. Henderson, J.-H. Her, A. M. Srivastava, N. Karkada*, et al.*, "Energy-efficient, high-color-rendering LED lamps using Oxyfluoride and Fluoride phosphors," *Chem. Mater.,* vol. 22, pp. 4076-4082, 2010.

[183] H-S. Chen, C-K. Hsu, and Hsin-Yen Hong, "InGaN–CdSe–ZnSe quantum dots white LEDs," *IEEE Photon. Technol. Lett.,* vol. 18, no. 1, pp. 193-195, 2006.

[184] S. Nizamoglu, G. Zengin, and H. V. Demir, "Color-converting combinations of nanocrystal emitters for warm-white light generation with high color rendering index," *Appl. Phys. Lett.,* vol. 92, pp. 031102, 2008.

[185] K. Becker, J. M. Lupton, J. Muller, A. L. Rogach, D. V. Talapin, H. Weller*, et al.*, "Electrical control of Forster energy transfer," *Nat. Mater.,* vol. 5, pp. 777-781, 2006.

[186] H-M. Kim, Y-H. Cho, Hosang Lee, Suk Il Kim, Sung Ryong Ryu, Deuk Young Kim, Tae Won Kang, and Kwan Soo Chung, "High-brightness light emitting diodes using dislocation-free indium gallium nitride/gallium nitride multiquantum-well nanorod arrays," *Nano Lett.,* vol. 4, no. 6, pp. 1059–1062, 2004.

[187] C.-H. Lee, J. Yoo, Y. J. Hong, J. Cho, Y.-J. Kim, S.-R. Jeon*, et al.*, " GaN/$In_{1-x}Ga_xN$/GaN/ZnO nanoarchitecture light emitting diode microarrays," *Appl. Phys. Lett.,* vol. 94, pp. 213101, 2009.

[188] S. Xu, C. Xu, Y. Liu, Y. Hu, R. Yang, Q. Yang*, et al.*, "Ordered nanowire array blue/near-UV light emitting diodes," *Adv. Mater.,* vol. 22, pp. 4749-4753, 2010.

[189] L-Y. Chen, Y-Y. Huan, C-H. Chang, Y-H. Sun, Y-W. Cheng, M-Y. Ke, C-P. Chen, and J. Huang, "High performance InGaN/GaN nanorod light emitting diode arrays fabricated by nanosphere lithography and chemical mechanical polishing processes," *Opt. Exp.,* vol. 18, no. 8, pp. 7664-7669, 2010.

[190] H. P. T. Nguyen, K. Cui, S. Zhang, S. Fathololoumi, and Z. Mi, "Full-color InGaN/GaN dot-in-a-wire light emitting diodes on silicon," *Nanotechnology,* vol. 22, pp. 445202, 2011.

[191] H. P. T. Nguyen, S. Zhang, A. T. Connie, M. G. Kibria, Q. Wang, I. Shih*, et al.*, "Breaking the carrier injection bottleneck of phosphor-free nanowire white light-emitting diodes," *Nano Lett.,* vol. 13, pp. 5437-5442, 2013.

[192] Y. H. Ra, R. Navamathavan, H. I. Yoo, and C. R. Lee, "Single nanowire light-emitting diodes using uniaxial and coaxial InGaN/GaN multiple quantum wells synthesized by metalorganic chemical vapor deposition," *Nano Lett.,* vol. 14, pp. 1537-1545, 2014.

[193] F. Qian, S. Gradečak, Y. Li, C-Y. Wen, and C. M. Lieber, "Core/multishell nanowire heterostructures as multicolor, high-efficiency light-emitting diodes," *Nano Lett.,* vol. 5, no. 11, pp. 2287-2291, 2011.

[194] L. J. Lauhon, M. S. Gudiksen, D. Wang, and C. M. Lieber, "Epitaxial core–shell and core–multishell nanowire heterostructures," *Nature,* vol. 420, pp. 57-61, 2001.

[195] F. Qian, Y. Li, S. Gradec˘ak, D. Wang, C. J. Barrelet, and C. M. Lieber, "Gallium Nitride-based nanowire radial heterostructures for nanophotonics," *Nano Lett.,* vol. 4, no. 10, pp. 1975–1979, 2004.

[196] R. Koester, J. S. Hwang, D. Salomon, X. Chen, C. Bougerol, J. P. Barnes*, et al.*, "M-plane core-shell InGaN/GaN multiple-quantum-wells on GaN wires for electroluminescent devices," *Nano Lett.,* vol. 11, pp. 4839-45, 2011.
[197] H. Sekiguchi, K. Kishino, and A. Kikuchi, "Emission color control from blue to red with nanocolumn diameter of InGaN/GaN nanocolumn arrays grown on same substrate," *Appl. Phys. Lett.,* vol. 96, pp. 231104, 2010.
[198] . B. Schlager, K. A. Bertness, Paul T. Blanchard, Lawrence H. Robins, Alexana Roshko, and Norman A. Sanford, N. A., "Steady-state and time-resolved photoluminescence from relaxed and strained GaN nanowires grown by catalyst-free molecular-beam epitaxy," *J. Appl. Phys.,* vol. 103, pp. 124309, 2008.
[199] R. Aleksiejnas, M. Sūdžius, T. Malinauskas, J. Vaitkus, K. Jarašinas, and S. Sakai, "Determination of free carrier bipolar diffusion coefficient and surface recombination velocity of undoped GaN epilayers," *Appl. Phys. Lett.,* vol. 83, no. 6, pp. 1157-1159, 2003.
[200] www.corsslight.com, "Crosslight," ed, 2013.
[201] S. Zhang, A. T. Connie, D. A. Laleyan, H. P. T. Nguyen, Q. Wang, J. Song, I. Shih, and Z. Mi, "On the carrier injection efficiency and thermal property of InGaN/GaN axial nanowire light emitting diodes," *IEEE J. Quan. Elec.,* vol. 50, no. 6, pp. 483-490, 2014.
[202] S. Zhao, M. G. Kibria, Q. Wang, H. P. Nguyen, and Z. Mi, "Growth of large-scale vertically aligned GaN nanowires and their heterostructures with high uniformity on SiO(x) by catalyst-free molecular beam epitaxy," *Nanoscale,* vol. 5, pp. 5283-7, 2013.
[203] M. L. Nakarmi, B. Cai, J. Y. Lin, and H. X. Jiang, "Three-step growth method for high quality AlN epilayers," P*hys. Stat. Solidi (a),* vol. 209, pp. 126-129, 2012.
[204] H. W. Kim, M. A. Kebede, and H. S. Kim, "Temperature-controlled growth and photoluminescence of AlN nanowires," *Appl. Surf. Sci.,* vol. 255, pp. 7221-7225, 2009.
[205] C. Xu, L. Xue, C. Yin, and G. Wang, "Formation and photoluminescence properties of AlN nanowires," P*hys. Stat. Solidi (a),* vol. 198, pp. 329-335, 2003.
[206] G. R. Yazdi, P. O. Persson, D. Gogova, R. Fornari, L. Hultman, M. Syvajarvi*, et al.*, "Aligned AlN nanowires by self-organized vapor-solid growth," *Nanotechnology,* vol. 20, pp. 495304, 2009.
[207] J. Li, K. B. Nam, M. L. Nakarmi, J. Y. Lin, and H. X. Jiang, "Band-edge photoluminescence of AlN epilayers," *Appl. Phys. Lett.,* vol. 81, pp. 3365, 2002.
[208] A. Sedhain, J. Li, J. Y. Lin, and H. X. Jiang, "Probing exciton-phonon interaction in AlN epilayers by photoluminescence," *Appl. Phys. Lett.,* vol. 95, pp. 061106, 2009.
[209] B. N. Pantha, N. Nepal, T. M. Al Tahtamouni, M. L. Nakarmi, J. Li, J. Y. Lin, and H. X. Jiang, "Correlation between biaxial stress and free exciton transition in AlN epilayers," *Appl. Phys. Lett.,* vol. 91, pp. 121117, 2007.
[210] X. B. Zhang, T. Taliercio, S Kolliakos and P Lefebvre, "Influence of electron–phonon interaction on the optical properties of III nitride semiconductors," *J. Phys.: Conden. Matter,* vol. 13, pp. 7053 2001.
[211] Z. Li, "Interface-optical-phonon modes in quasi-one-dimensional wurtzite rectangular quantum wires," *Commun. Theor. Phys.,* vol. 46, pp. 1109, 2006.

[212] S. Dhara, P. Sahoo, A. K. Tyagi, and B. Raj, "Surface optical mode in semiconductor nanowires," in *Nanowires - Implementations and Applications* D. A. Hashim, Ed., (http://www.intechopen.com/books/nanowires-implementations-and-applications/surface-optical-modesin-semiconductor-nanowires).
[213] R. Gupta, Q. Xiong, G. D. Mahan, and P. C. Eklund, "Surface optical phonons in gallium phosphide nanowires," *Nano Lett.,* vol. 3, no. 12, pp. 1745–1750, 2003.
[214] R. Mata, A. Cros, K. Hestroffer, and B. Daudin, "Surface optical phonon modes in GaN nanowire arrays: Dependence on nanowire density and diameter," *Phys. Rev. B,* vol. 85, pp. 035322, 2012.
[215] J. Titus, H. P. T. Nguyen, Z. Mi, and A. G. U. Perera, "Optical phonon modes in InGaN/GaN dot-in-a-wire heterostructures grown by molecular beam epitaxy," *Appl. Phys. Lett.,* vol. 102, pp. 121901, 2013.
[216] L. Zhang, J.-j. Shi, and T. Tansley, "Polar vibration spectra of interface optical phonons and electron-interface optical phonon interactions in a wurtzite GaN-AlN nanowire," *Phys. Rev. B,* vol. 71, pp. 245324, 2005.
[217] Q. Wang, S. Zhao, A. T. Connie, I. Shih, Z. Mi, T. Gonzalez*, et al.*, "Optical properties of strain-free AlN nanowires grown by molecular beam epitaxy on Si substrates," *Appl. Phys. Lett.,* vol. 104, pp. 223107, 2014.
[218] T. Kinoshita, T. Obata, H. Yanagi, and S.-i. Inoue, "High p-type conduction in high-Al content Mg-doped AlGaN," *Appl. Phys. Lett.,* vol. 102, pp. 012105, 2013.
[219] P. Kozodoy, H. Xing, S. P. DenBaars, U. K. Mishra, A. Saxler, R. Perrin*, et al.*, "Heavy doping effects in Mg-doped GaN," *J. Appl. Phys.,* vol. 87, pp. 1832, 2000.
[220] K. B. Nam, M. L. Nakarmi, J. Y. Lin, and H. X. Jiang, "Deep impurity transitions involving cation vacancies and complexes in AlGaN alloys," *Appl. Phys. Lett.,* vol. 86, pp. 222108, 2005.
[221] N. Nepal, K. B. Nam, M. L. Nakarmi, J. Y. Lin, H. X. Jiang, J. M. Zavada*, et al.*, "Optical properties of the nitrogen vacancy in AlN epilayers," *Appl. Phys. Lett.,* vol. 84, pp. 1090, 2004.
[222] S. Zhao, A. T. Connie, M. H. Dastjerdi, X. H. Kong, Q. Wang, M. Djavid*, et al.*, "Aluminum nitride nanowire light emitting diodes: Breaking the fundamental bottleneck of deep ultraviolet light sources," *Sci Rep,* vol. 5, pp. 8332, 2015.
[223] S. Zhao, B. H. Le, D. P. Liu, X. D. Liu, M. G. Kibria, T. Szkopek*, et al.*, "p-Type InN nanowires," *Nano Lett.,* vol. 13, pp. 5509-5513, 2013.
[224] U. Kaufmann, M. Kunzer, M. Maier, H. Obloh, A. Ramakrishnan, B. Santic*, et al.*, "Nature of the 2.8 eV photoluminescence band in Mg doped GaN," *Appl. Phys. Lett.,* vol. 72, pp. 1326, 1998.
[225] S. Zhao, X. Liu, and Z. Mi, "Photoluminescence properties of Mg-doped InN nanowires," *Appl. Phys. Lett.,* vol. 103, pp. 203113, 2013.
[226] T. Nagai, T. J. Inagaki, and Y. Kanemitsu, "Band-gap renormalization in highly excited GaN," *Appl. Phys. Lett.,* vol. 84, pp. 1284, 2004.
[227] A. B. Slimane, A. Najar, R. Elafandy, D. P. San-Román-Alerigi, D. Anjum, T. K. Ng, and B. S. Ooi, "On the phenomenon of large photoluminescence red shift in GaN nanoparticles," *Nanoscale Res. Lett.,* vol. 8, pp. 342, 2013.
[228] I. Aleksandrov and K. Zhuravlev, "Photoluminescence of GaN/AlN quantum dots at high excitation powers," P*hys. Stat. Solidi (c),* vol. 7, pp. 2230-2232, 2010.

[229] Y. P. Varshni, "Temperature dependence of the energy gap in semiconductors," *Physica,* ol. 34, pp. 149-154, 1967.
[230] T. Hanada, "Basic properties of ZnO, GaN, and related materials," *Adv. Mater. Res.,* vol. 12, pp. 1-19, 2009.
[231] K. Kumakura, T. Makimoto, and N. Kobayashi, "Mg-acceptor activation mechanism and transport characteristics in p-type InGaN grown by metalorganic vapor phase epitaxy," *J. Appl. Phys.,* vol. 93, pp. 3370, 2003.
[232] Y. Taniyasu, M. Kasu, and T. Makimoto, "An aluminium nitride light-emitting diode with a wavelength of 210 nanometres," *Nature,* vol. 441, pp. 325-328, 2006.
[233] K. Davitt, Y-K. Song, W. R. Patterson III, A. V. Nurmikko, M. Gherasimova, J. Han, Y-L. Pan, and R. K. Chang, "290 and 340 nm UV LED arrays for fluorescence detection from single airborne particles," *Opt. Exp.,* vol. 13, no. 23, pp. 9548-9555, 2005.
[234] H. Peng, E. Makarona, Y. He, Y. K. Song, A. V. Nurmikko, J. Su*, et al.*, "Ultraviolet light-emitting diodes operating in the 340 nm wavelength range and application to time-resolved fluorescence spectroscopy," *Appl. Phys. Lett.,* vol. 85, pp. 1436, 2004.
[235] H. Xu, J. Zhang, K. M. Davitt, Y. K. Song, and A. V. Nurmikko, "Application of blue–green and ultraviolet micro-LEDs to biological imaging and detection," *J. Phys. D: Appl. Phys.,* vol. 41, pp. 094013, 2008.
[236] S. M. Rothman, G. Perry, X-F. Yang, K. Hyrc, and B. F. Schmidt, "Optical Suppression of Seizure-Like Activity with an LED," *Epilepsy Res.,* vol. 74, no. 2-3, pp. 201-209, 2007.
[237] M. Morrell, "Brain stimulation for epilepsy: can scheduled or responsive neurostimulation stop seizures?," *Curr. Opin. Neurol.,* vol. 19, pp. 5, 2006.
[238] J. Zhang, S. Wu, S. Rai, V. Mandavilli, V. Adivarahan, A. Chitnis*, et al.*, "AlGaN multiple-quantum-well-based, deep ultraviolet light-emitting diodes with significantly reduced long-wave emission," *Appl. Phys. Lett.,* vol. 83, pp. 3456, 2003.
[239] L. Zhou, J. E. Epler, M. R. Krames, W. Goetz, M. Gherasimova, Z. Ren*, et al.*, "Vertical injection thin-film AlGaN/AlGaN multiple-quantum-well deep ultraviolet light-emitting diodes," *Appl. Phys. Lett.,* vol. 89, pp. 241113, 2006.
[240] S. Zhao, S. Fathololoumi, K. H. Bevan, D. P. Liu, M. G. Kibria, Q. Li*, et al.*, "Tuning the surface charge properties of epitaxial InN nanowires," *Nano Lett.,* vol. 12, pp. 2877-2882, 2012.
[241] Y. Q. Bie, Z. M. Liao, P. W. Wang, Y. B. Zhou, X. B. Han, Y. Ye*, et al.*, "Single ZnO nanowire/p-type GaN heterojunctions for photovoltaic devices and UV light-emitting diodes," *Adv. Mater.,* vol. 22, pp. 4284-4287, 2010.
[242] M. T. Chen, M. P. Lu, Y. J. Wu, J. Song, C. Y. Lee, M. Y. Lu*, et al.*, "Near UV LEDs made with in situ doped p-n homojunction ZnO nanowire arrays," *Nano Lett.,* vol. 10, pp. 4387-93, 2010.
[243] S. K. Jha, C. Luan, C. H. To, O. Kutsay, J. Kováč, J. A. Zapien*, et al.*, "ZnO-nanorod-array/p-GaN high-performance ultra-violet light emitting devices prepared by simple solution synthesis," *Appl. Phys. Lett.,* vol. 101, pp. 211116, 2012.

[244] O. Lupan, T. Pauporte, and B. Viana, "Low-voltage UV-electroluminescence from ZnO-nanowire Array/p-GaN light-emitting diodes," *Adv. Mater.,* vol. 22, pp. 3298-302, 2010.
[245] X.-M. Zhang, M.-Y. Lu, Y. Zhang, L.-J. Chen, and Z. L. Wang, "Fabrication of a High-Brightness Blue-Light-Emitting Diode Using a ZnO-Nanowire Array Grown on p-GaN Thin Film," *Adv. Mater.,* vol. 21, pp. 2767-2770, 2009.
[246] K. H. Kim, J. Li, S. X. Jin, J. Y. Lin, and H. X. Jiang, "III-nitride ultraviolet light-emitting diodes with delta doping," *Appl. Phys. Lett.,* vol. 83, pp. 566, 2003.
[247] T. N. Oder, K. H. Kim, J. Y. Lin, and H. X. Jiang, "III-nitride blue and ultraviolet photonic crystal light emitting diodes," *Appl. Phys. Lett,* vol. 84, pp. 466, 2004.
[248] G. A. Smith, "341 nm emission from hydride vapor-phase epitaxy ultraviolet light-emitting diodes," *J. Appl. Phys.,* vol. 95, pp. 8247, 2004.
[249] T. Wang, K. B. Lee, J. Bai, P. J. Parbrook, R. J. Airey, Q. Wang*, et al.*, "Greatly improved performance of 340 nm light emitting diodes using a very thin GaN interlayer on a high temperature AlN buffer layer," *Appl. Phys. Lett,* vol. 89, pp. 081126, 2006.
[250] T. Wang, K. B. Lee, J. Bai, P. J. Parbrook, F. Ranalli, Q. Wang*, et al.*, "The 310–340 nm ultraviolet light emitting diodes grown using a thin GaN interlayer on a high temperature AlN buffer," *J. Phys. D: Appl. Phys.,* vol. 41, pp. 094003, 2008.
[251] A. Chitnis, J. Sun, V. Mandavilli, R. Pachipulusu, S. Wu, M. Gaevski*, et al.*, "Self-heating effects at high pump currents in deep ultraviolet light-emitting diodes at 324 nm," *Appl. Phys. Lett,* vol. 81, pp. 3491, 2002.
[252] M. L. Reed, M. Wraback, A. Lunev, Y. Bilenko, X. Hu, A. Sattu*, et al.*, "Device self-heating effects in deep UV LEDs studied by systematic variation in pulsed current injection," *Phys. Stat.Ssolidi (c),* vol. 5, pp. 2053-2055, 2008.
[253] E. F. Schubert, L.W. Tu, G. J. Zydzik, R. F. Kopf, A. Benvenuti, and M. R. Pinto, "Elimination of heterojunction band discontinuities by modulation doping," *Appl. Phys. Lett.,* vol. 60, pp. 466, 1992.
[254] S. R. Jeon, Z. Ren, G. Cui, J. Su, M. Gherasimova, J. Han*, et al.*, "Investigation of Mg doping in high-Al content p-type $Al_xGa_{1-x}N$ ($0.3<x<0.5$)," *Appl. Phys. Lett.,* vol. 86, pp. 082107, 2005.
[255] R. J. Airey, K. B. Lee, P. J. Parbrook, J. Bai, F. Ranalli, T. Wang*, et al.*, "Temperature dependent behaviour of 340 nm light emitting diodes incorporating a gallium nitride interlayer," *J. Phys. D: Appl. Phys.,* vol. 41, pp. 094004, 2008.
[256] H. Jimi, T. Inada, and K. Fujiwara, "Temperature-dependent electroluminescence intensity in green and blue (In,Ga)N multiple-quantum-well diodes," P*hys. Stat.Ssolidi – Rapid Res. Lett.,* vol. 2, pp. 50-52, 2008.
[257] H. Jimi, T. Inada, M. Horiguchi, A. Satake, and K. Fujiwara, "Comparative study of temperature-dependent electroluminescence efficiency in blue and green (In,Ga)N multiple-quantum-well diodes," P*hys. stat. Solidi (c),* vol. 5, pp. 2105-2107, 2008.
[258] C. G. Moe, G. A. Garrett, P. Rotella, H. Shen, M. Wraback, M. Shatalov*, et al.*, "Impact of temperature-dependent hole injection on low-temperature electroluminescence collapse in ultraviolet light-emitting diodes," *Appl. Phys. Lett.,* vol. 101, pp. 253512, 2012.

[259] J. C. Zhang, Y. Sakai, and T. Egawa, "Low-temperature electroluminescence quenching of AlGaN deep ultraviolet light-emitting diodes," *Appl. Phys. Lett.,* vol. 96, pp. 013503, 2010.
[260] Y. Taniyasu and M. Kasu, "Surface 210 nm light emission from an AlN p–n junction light-emitting diode enhanced by A-plane growth orientation," *Appl. Phys. Lett.,* vol. 96, pp. 221110, 2010.
[261] A. Kinoshita, H. Hirayama, M. Ainoya, Y. Aoyagi, and A. Hirata, "Room-temperature operation at 333 nm of $Al_{0.03}Ga_{0.97}N/Al_{0.25}Ga_{0.75}N$ quantum-well light-emitting diodes with Mg-doped superlattice layers," *Appl. Phys. Lett.,* vol. 77, pp. 175, 2000.
[262] P. Kozodoy, Y. P. Smorchkova, M. Hansen, H. Xing, S. P. DenBaars, U. K. Mishra*, et al.*, "Polarization-enhanced Mg doping of AlGaN/GaN superlattices," *Appl. Phys. Lett.,* vol. 75, pp. 2444, 1999.
[263] E. L. Waldron, J. W. Graff, and E. F. Schubert, "Improved mobilities and resistivities in modulation-doped p-type AlGaN/GaN superlattices," *Appl. Phys. Lett.,* vol. 79, pp. 2737, 2001.
[264] A. Yasan, R. McClintock, S. R. Darvish, Z. Lin, K. Mi, P. Kung*, et al.*, "Characteristics of high-quality p-type $Al_xGa_{1-x}N$/GaN superlattices," *Appl. Phys. Lett.,* vol. 80, pp. 2108, 2002.
[265] E. F. Pecora, W. Zhang, A. Y. Nikiforov, J. Yin, R. Paiella, L. D. Negro, and T. D. Moustakas, "Sub-250nm light emission and optical gain in AlGaN materials," *J. Appl. Phys.,* vol. 113, pp. 013106, 2013.
[266] J. Zhang, H. Zhao, and N. Tansub, "Effect of crystal-field split-off hole and heavy-hole bands crossover on gain characteristics of high Al-content AlGaN quantum well lasers," *Appl. Phys. Lett.,* vol. 97, pp. 111105, 2010.
[267] T. Oto, R. G. Banal, Mitsuru Funato, and Yoichi Kawakami, "Optical gain characteristics in Al-rich AlGaN/AlN quantum wells," *Appl. phys. Lett.,* vol. 104, pp. 181102, 2014.
[268] W. Guo, Z. Bryan, J. Xie, R. Kirste, S. Mita, I. Bryan, L. Hussey, M. Bobea, B. Haidet, M. Gerhold, R. Collazo, and Z. Sitar, "Stimulated emission and optical gain in AlGaN heterostructures grown on bulk AlN substrates," *J. Appl. Phys.,* vol. 115, pp. 103108, 2014.
[269] T. K. Sharma, D. Naveh, and E. Towe, "Strain-driven light polarization switching in deep ultraviolet nitride emitters," *Phys. Rev. B,* vol. 84, pp. 035305, 2011.
[270] P. Zhao, L. Han, M. R. McGoogan, and H. Zhao, "Analysis of TM mode light extraction efficiency enhancement for deep ultraviolet AlGaN quantum wells light-emitting diodes with III-nitride micro-domes " *Opt. Mater. Exp.,* vol. 2, no. 10, pp. 1397-1406, 2002.
[271] N. Gao, K. Huang, J. Li, S. Li, X. Yang, and J. Kang, "Surface-plasmon-enhanced deep-UV light emitting diodes based on AlGaN multi-quantum wells," *Sci Rep,* vol. 2, pp. 816, 2012.
[272] H.-Y. Ryu, "Large enhancement of light extraction efficiency in AlGaN-based nanorod ultraviolet light-emitting diode structures," *Nanoscale Res. Lett.,* vol. 9, pp. 58, 2014.

[273] H. Yoshida, Y. Yamashita, M. Kuwabara, and H. Kan, "Demonstration of an ultraviolet 336 nm AlGaN multiple-quantum-well laser diode," *Appl. Phys. Lett.,* vol. 93, pp. 241106, 2008.
[274] K. H. Li, X. Liu, Q. Wang, S. Zhao, and Z. Mi, "Ultralow threshold, electrically injected AlGaN nanowire ultraviolet lasers on Si at low temperature," *Nature Nano Technol.,* vol. 10, no. 2, pp. 140-144, 2014.
[275] F. Akyol, "N-Polar III- Nitride Optoelectronic Devices," Masters Thesis, Electrical and Computer Science, Ohio State University, 2011.
[276] F. Akyol, D. N. Nath, S. Krishnamoorthy, P. S. Park, and S. Rajan, "Suppression of electron overflow and efficiency droop in N-polar GaN green light emitting diodes," *Appl. phys. Lett.,* vol. 100, pp. 111118, 2012.
[277] H. Naoi, F. Matsuda, T. Araki, A. Suzuki, Y. Nanishi, "The effect of substrate polarity on the growth of InN by RF-MBE," *J. Crys. Grow.,* vol. 269, pp. 155-161, 2004.
[278] K. Xu and A. Yoshikawa, "Effects of film polarities on InN growth by molecular-beam epitaxy," *Appl. phys. Lett.,* vol. 83, no. 2, pp. 251-253, 2003.
[279] E. Sarigiannidou, E. Monroy, N. Gogneau, G. Radtke, P. Bayle-Guillemaud, E. Bellet-Amalric, B. Daudin and J. L. Rouvi`ere, "Comparison of the structural quality in Ga-face and N-face polarity GaN/AlN multiple-quantum-well structures," *Semicond. Sci. Technol.,* vol. 21, pp. 612, 2006.
[280] O. Ambacher, J. Smart, J. R. Shealy, N. G. Weimann, K. Chu, M. Murphy, W. J. Schaff, L. F. Eastman, R. Dimitrov, L. Wittmer, M. Stutzmann, W. Rieger, and J. Hilsenbeck, "Two-dimensional electron gases induced by spontaneous and piezoelectric polarization charges in N- and Ga-face AlGaN/GaN heterostructures, " *J. Appl. Phys.,* vol. 85, pp. 3222-3233, 1999.
[281] R. Dimitrov, M. Murphy, J. Smart, W. Schaff, J. R. Shealy et al., "Two-dimensional electron gases in Ga-face and N-face AlGaN/GaN heterostructures grown by plasma-induced molecular beam epitaxy and metalorganic chemical vapor deposition on sapphire," *J. Appl. Phys.,* vol. 87, no. 7, pp. 3375-3380, 2000.